Design, Fabrication, and Characterization of Monolithically Integrated Acoustic and Photonic Devices on Lithium Niobate Over Insulator (LNOI) Platform

Submitted in partial fulfillment of the requirements for

the degree of

Doctor of Philosophy

in

Electrical and Computer Engineering

Mohamed Mahmoud

B.S., Electronics and Communications Engineering, Ain Shams University

M.S., Electronics and Communications Engineering, Ain Shams University

Carnegie Mellon University

Pittsburgh, PA

February 2018

Acknowledgements

All praise is to God, the Lord of the Worlds, the most gracious and most merciful.

First, I would like to thank my advisor, Professor Gianluca Piazza for his support and guidance both technically and personally. Many times, I was stuck in the fabrication process and Gian was always around to help, give advice and support both technically and emotionally. Gianluca was also supportive and helpful on the personal side. I can not forget how supportive he was when my wife was in the hospital and I sent him an e-mail asking to work remotely and he just said "Stay next to your wife".

I would also like to thank my thesis committee, Professor Tamal Mukherjee, Prof. James Bain and Professor Sheng (Mech-E CMU) for their significant help and feedback.

I would like to express my gratitude to the AOG team including students, postdocs and professors: Ashraf Mahmoud, Lutong Cai and MSI Khan. Ashraf had a major role in the SAW design of the AOG and in programming the ZI-box in the measurement setup. Lutong was almost my second hands in the fabrication and characterization. Such a successful team work resulted in having numerous publications as outcome of this PhD thesis. Furthermore, I have learned a lot from prof.Piazza as a PI for our project in terms of having a multi-disciplinary system vision as well as managing our team making sure everything is in place. I would like also to thank Prof.Bain and Prof.Tamal for their help and guidance in our biweekly meetings.

This work was supported by supported by the DARPA PRIGM-AIMS program under Award No. N66001-16-1-4025. so I would like to express my gratitude to them for funding. Although the AOG is fully funded by Darpa, I would like to thank the National Science Foundation as well since the first two years I was working on a project funded by NSF under award NSF ECCS-1201659 and that's where I gained hands-on experience in the clean room.

I would like to thanks all the PMaNS lab colleagues including the current students/post-docs as well as the alumni. I would like to name one post doc "Abhay Kochar" who has provided very useful advice in terms of the fabrication process. I learned a lot from Abhay since he has a very

wide fabrication experience. Additionally I would like to name one previous student “Sid Ghosh” as he has helped me a lot in the beginning of the PhD and in studying the field of Optomechanics. Sid has also provided me support in getting trained on the clean room tools.

I’m almost speechless about the efforts spent by the CMU NANOFAB staff with all their names mentioned (Matt Moneck, Mark Weiler, Norman Gottron, Mason Risley, Dante Boni and James Rosvanis). Those guys have sleepless nights to makes sure all the tools are up and operational.

I would like to thanks the Egyptian friends who welcomed me in Pittsburgh and helped me and my family commute around the city and enjoy a friendly atmosphere with them being around. Those friends are Mohamed Darwish, Mohamed Abdelmoula, Waleed Ammar, Ahmed Hefny, Ahmed Abdelgawad, Nour Salah, Dr.Ashraf Gamal, Mazen Soliman and their families.

I would like to thank my family members: My wife, Ayat Gadelrab, for her help, support and patience. At some point, I had a belief that the PhD student’s wives are happier for their graduation more than the students themselves. I woulk like to thank my twin kids, Hamza and Ziyad, for their contribution to the thesis by motivating me to work harder. Having twin kids is fun but is a lot of work as well, so I would like to thank their grandmother, Wedad Aly, for coming all the way from Egypt to the US before their delivery to help. Furthermore, her VISA is a visitor’s VISA which does not allow her to stay more than six months. Since she had been around for more than a year, she had to return to Egypt then come back which is not an easy trip.

Abstract

Integration of acoustics and photonics devices on the same chip will enable various applications including: building miniaturized sensors, on-chip filtering and optical signal processing, high speed modulation, as well as non-linear optical devices. As an example of the capabilities enabled by such integration, we target the development of a rotation sensor gyroscope based on the acousto-optic effect. The gyroscope components are integrated on a Lithium Niobate Over Insulator (LNOI) substrate because it is a unique platform that exhibits exceptional acoustic as well as photonic properties. However, acoustics and photonics have never been integrated on such substrate, which required the development of a new fabrication process and the design of novel components.. The main challenges we had to overcome and resulted in innovative demonstrations of fabrication processes and devices are:

- Developing a robust fabrication process for etching lithium Niobate (LN) waveguides and integrating them with acoustic transducers: A robust fabrication process was developed on the LNOI platform, which can integrate patterning sub-micron features together with microscale ones on the same 3'' substrate. Furthermore, the developed fabrication process enabled integrating metallic Al electrodes together with etched LN waveguides, which is required for building various components like electro-optic modulators and acousto-optic modulators.
- Coupling light in and out of chip: Gratings couplers were designed for optimum coupling of the TE polarized light. The optimization was based on FDTD simulation on LUMERICAL. The grating couplers realization enabled estimation of the light coupling loss in and out of the chip. The measured coupling loss was about 9 dB per coupler in the best case which is much more than the estimated from simulation. That difference is attributed to the alignment accuracy of the photonic chip.
- Integrating photonic waveguides/resonators and coupling light between them: LNOI waveguides and photonic resonators were designed and built. The photonic resonators

enabled extraction of the losses of waveguides by monitoring the photonic resonator Quality factor, Q, or Finesse (F). Directional couplers (DCs) are commonly used as coupling elements to photonic resonators. However, etching narrow gaps in LN is a challenge that we avoided by using multi-mode interference (MMI) couplers, where butterfly MMI couplers were designed as coupling element to photonic racetrack (RT) resonators aiming for critical coupling condition. Additionally 3-dB MMI couplers were designed to be used as beam combiners in the Mach-Zehnder interferometer (MZI). The built RT resonators enabled extraction of the propagation losses in the etched LNOI photonic waveguides, which were found to be equal to2.5 dB/cm.

- Building high efficiency electro-optic modulators (EOMs): The EOM is used in the AOG to compensate for temperature variations and other environmental variation affecting the rotation measurement. The EOM realization enabled extraction of the electro-optic (EO) coefficient for the LN thin film, which permits to evaluate the magnitude of the control voltages required to stabilize the system. EOMs of two different types were demonstrated, one is based on a photonic RT while the other is based on an Asymmetric MZI (AMZI). The RT EOM represents the first demonstration for such device with etched waveguides in Y cut LNOI platform. Modulation bandwidth of 4 GHz, wavelength tuning rate of 0.32 pm/V and an ER of more than 10 dB were experimentally measured for the RT EOM. For the AMZI, a half wave voltage length product of 16.8 Vcm was experimentally measured. Although, it is not the best we can get from this LNOI platform because of our wide waveguides, feeding that EO coefficient to the AOG system model ensures that the temperature variation from -54 ^{o}C to 25 ^{o}C can be compensated by applying a maximum voltage of 64.5 V.

- Building efficient acousto-optic modulators (AOMs): The AOM enabled the extraction of the acousto-optic (AO) coefficient, which directly impacts the AOG scale factor (*SF*). Additionally, two different types of AOMs were demonstrated, one is based on an MZI embedded inside a SAW cavity while the other is based on a photonic RT whose coupling condition is under EO control. For the MZI AOM, the SAW resonator enhances the modulation efficiency due to the resonator Q such that the phase shift per

square root of power extracted from the measurements is a factor of 3x higher than what previously reported on a GaAs platform, which makes it, to the author's knowledge, effectively the highest AO modulation ever attained on chip. On the other hand, the EO tuned RT AOM showcases integration of various functionalities on same platform to build efficient AOM that can be operated at the desired wavelength. The EO tuning not only changes the operating optical wavelength but also ensures the critical coupling condition needed for efficient modulation. This design takes advantage of the unique AO and EO properties of LN, hence showcasing important building blocks for RF-photonic applications.

By addressing all the previous challenges through the demonstration of high performance components, we were able to prototype the first acousto-optic gyroscope. That prototype represents the first demonstration of a novel rotation sensing technique, which combines the following advantages: (i) large mass (there is no suspended mass in the sensing mechanism and hence no limits on increasing the mass and no concerns about stiction issues during fabrication), and (ii) high shock resistance (since the sensing mechanism is strain based, the AOG has no moving parts that would not survive high G accelerations).

The AOG *SF* is estimated comparing three photonic phase sensing techniques which are MZI, RT as well as RT coupled to MZI (MZI/RT). The phase sensitivity is estimated in terms of the cavity *F* for each technique. That theoretical analysis is verified by experimental measurement for the *SF* for both the MZI and the RT AOGs. The measured *SF* for the MZI is 48 nv/(^{o}/sec) while it is about 9 nv/(^{o}/sec) for the RT AOG. The *SF* is lower for the RT AOG because the Finesse (*F~6*) of the RT is not as high as expected. Nevertheless, these prototypes represent a proof of concept for our novel method for sensing rotation.

Future work could prove that this AOG concept could be disruptive. Reducing the losses in the LNOI waveguide is a key challenge that can be overcome and has been already demonstrated by other groups showcasing 100x lower propagation loss. The estimated *F* from our model in that case would increase by approximately 50x, hence improving the gyroscope *SF* by the same factor.

Further improvement of 100x is possible by increasing the SAW wavelength and Q. A separate challenge that needs to be addressed is the laser and photodetector integration on chip, which will reduce the coupling loss and the sensitivity to optical alignment.

Table of Contents

List of Figures

1. Introduction

1.1. Motivation

Integration of acoustic and photonic components on the same chip will enable various applications including: building miniaturized sensors [1], on-chip filtering [2] and optical signal processing [3], high speed modulation [4], as well as on chip scanners for holography displays [5] . Among these various application areas, we target harnessing the acousto-optic (AO) effect for building high sensitivity Micro Electro Mechanical Systems (MEMS) inertial sensors. For example, the demonstration of such a novel sensing technique will facilitate the deployment of strain based, large mass gyroscope with high stability and precision.

Micro-gyroscopes based on MEMS technology have been investigated for over 2 decades, and there has been a steady improvement in their performance and in the technology used for their production. Recently, a number of outstanding micro-gyroscopes have demonstrated sufficient performance to potentially replace fiber-optic and ring laser gyroscopes [6]–[8]. The micro-gyroscope has various advantages over optical ones such as the smaller dimensions, the lower power consumption and most importantly the ability to be manufactured with semiconductor-based processes. However, currently available MEMS gyroscopes for inertial grade applications have some drawbacks associated with the need for a large suspended mass, hence high susceptibility to external shocks and vibrations. As opposed to the MEMS gyroscope, the Surface Acoustic Wave (SAW) gyroscope [9]–[12] does not need a suspended vibrating mechanical structure. Therefore, it is more resilient to external shocks and vibrations. The SAW gyroscopes have shown performance that are limited by the small sensitivity of the detection mechanism and the noise associated with the read-out electronics. A novel approach that can combine the cost, size, weight and power advantages of the MEMS and SAW gyroscopes as well as the high scale factor and the better noise performance of the fiber optic and ring laser gyroscope is what we call an acousto-optic gyroscope (AOG). Figure 1.1 depicts the principal of operation of such a novel

approach. We envision building the device in a Lithium Niobate Over Insulator (LNOI) substrate. Vibrating gold (Au) pillars are placed in the center of symmetric SAW resonators in both the drive (X) and the sense directions (Y). With rotation around the Z axis, secondary SAW waves generated by the Coriolis effect propagate in the sense direction such that they can be sensed by the photonic waveguides etched in the Lithium Niobate (LN) thin film through the acousto-optic (or elasto-optic) effect in LN. The photonic detection method shown in the figure is a Mach-Zehnder interferometer (MZI) formed by two symmetric arms coupled to racetracks with high Finesse (F). Grating couplers are used to couple light into the chip from a laser source (eventually to be integrated), and out of the chip to two photodetectors. To implement a differential sensing method, a 3-dB optical coupler is used as a beam combiner at the output of the two MZI arms. To allow for compensation of temperature variations as well as mismatch between the two racetracks, the electro-optic (EO) effect in LN is employed to tune the index of refraction of each waveguide. An electro-optic modulator is formed by integrating metal electrodes along the etched waveguides.

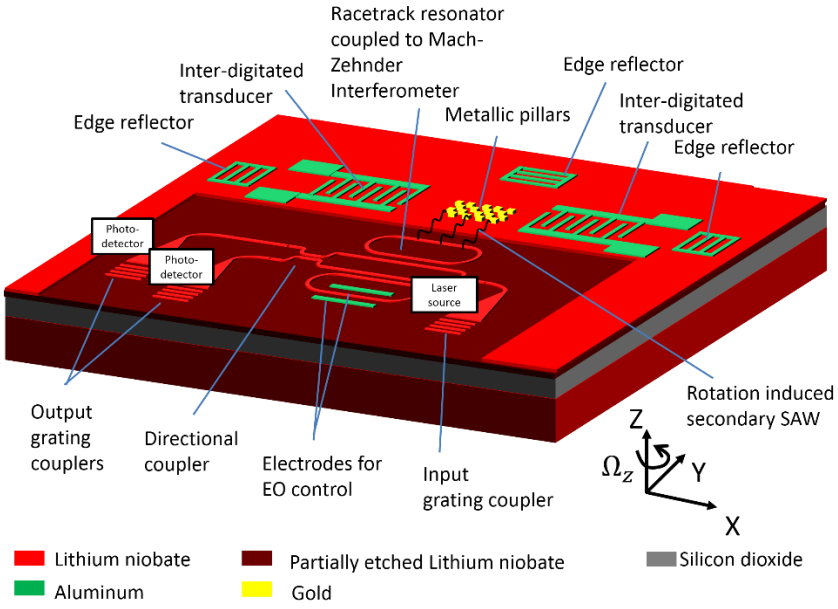

Figure 1.1 Graphic representation of the proposed acousto-optic gyroscope

The LNOI is considered the optimal platform for demonstrating an AOG as it has some of the best acoustic and photonic properties. It has shown to have a high electromechanical coupling coefficient, k_t^2, which allows building SAW resonators of smaller area. Since the SAW reflectors consume most of the area (the sketch in Figure 1.1 is not to scale), a high k_t^2 material is needed,

which reduces the reflectors size. Moreover, the LN has a high acousto-optic (AO) Figure of Merit (FOM), M_2, which provides for a large scale factor, *SF* (the sensitivity), for the gyroscope. Furthermore, LN is the material commonly used for building electro-optic modulators (EOMs) since it has the best electro-optical (EO) properties. However, there are various challenges associated with the fabrication and design of these integrated components. Those challenges are discussed in detail in this thesis and the next section presents a summary for the thesis contribution as well as its organization.

1.2. Thesis Contribution and Organization

The first challenge faced while integrating the various components that form the AOG is the etching of the LN to define the photonic components without impacting the acoustic transducers. This challenge and way to address it are discussed in Chapter 02. Chapter 3 discusses the design of the various photonic components forming the AOG and including: the gratings coupler, the MMI couplers, and the photonic resonators. The resonator Finesse, *F*, is experimentally measured and used to the extract the propagation loss in dB/cm for the LNOI etched waveguide . Additionally, to be able to estimate the needed control voltages for temperature compensation in the AOG, electro-optic modulators (EOMs) were designed, fabricated and characterized. The EOM design and associated experimental results are shown in Chapter 4. The AOG *SF* is a strong function of the AO FOM, M_2, of the material. For that reason, it is important to extract the value of M_2 for the LNOI platform. Thus, AOMs were designed and fabricated as discussed in Chapter 5. In chapter **Error! Reference source not found.**, we discuss how the LN properties and LNOI components impact the sensitivity of the AOG. In the same chapter we compare different phase sensing methods based on the AO effect. We verify these theoretical predictions against the first working prototype of an AOG. Chapter **Error! Reference source not found.** summarizes the work and outline future work required to optimize the proposed AOG.

2. Fabrication Process

Previously reported LN waveguides either relied on Titanium in-diffused waveguides or proton exchanged waveguides, which suffered from low index contrast. [13]–[15]. To attain better optical confinement, various research groups have investigated the use of the high index contrast provided by the Lithium Niobate on Insulator (LNOI) platform [16]–[25]. Various techniques for etching LN including ion milling, ion-beam-enhanced etching, and focused ion beam [21], [22], [26] were explored and yielded functional devices, but are not readily scalable to large substrates and production environments. Other groups avoided all together etching the LN by using LN as an active layer on top of a Si waveguide [27], [28] or used a loaded strip of different material that has an index of refraction similar to LN and placed it above LN to build the core of the waveguide [23]. Defining photonic waveguides by etching LN in an industry compatible process has a major advantage over those approaches where the photonic designer ensures most of the optical power confinement is inside the LN so that one can take advantage of the unique properties. The first section discusses the LUMERICAL model used to estimate the optical power confinement, which justifies the need to etch the LN film. The following section discusses the process flow used to etch LNOI waveguides and integrate them with gratings couplers as well as metallic electrodes needed for building various photonic components as well as the AOG.

2.1. Power Confinement Inside LN

Figure 2.1-a shows a 2D cross-sectional view for the etched LNOI waveguide. LUMERICAL finite difference Eigen mode solver was performed to estimate the optical power distribution inside the waveguide through which the optical power confinement factor is calculated as:

$$\Gamma_{LN} = \frac{\text{Power inside core}}{\text{Total power}} \tag{2.1}$$

Figure 2.1-b plots the estimated optical confinement factor, Γ_{LN}, of the fundamental mode versus the sidewall angle, θ_m for three different values of the waveguide width, d. It clearly shows

that for waveguides narrower than $0.8\,\mu m$, slanted side walls are necessary to improve light confinement. For wider waveguides, the value of Γ_{LN} is almost the same across a wide range of values of angles. The values obtained for Γ_{LN} by other authors [23] who used a loaded strip of different material that has an index of refraction similar to LN and placed it above LN to build the core of the waveguide is about 50%. Thus, this analysis shows that defining LNOI waveguides by etching is of paramount importance for better optical confinement inside the LN material.

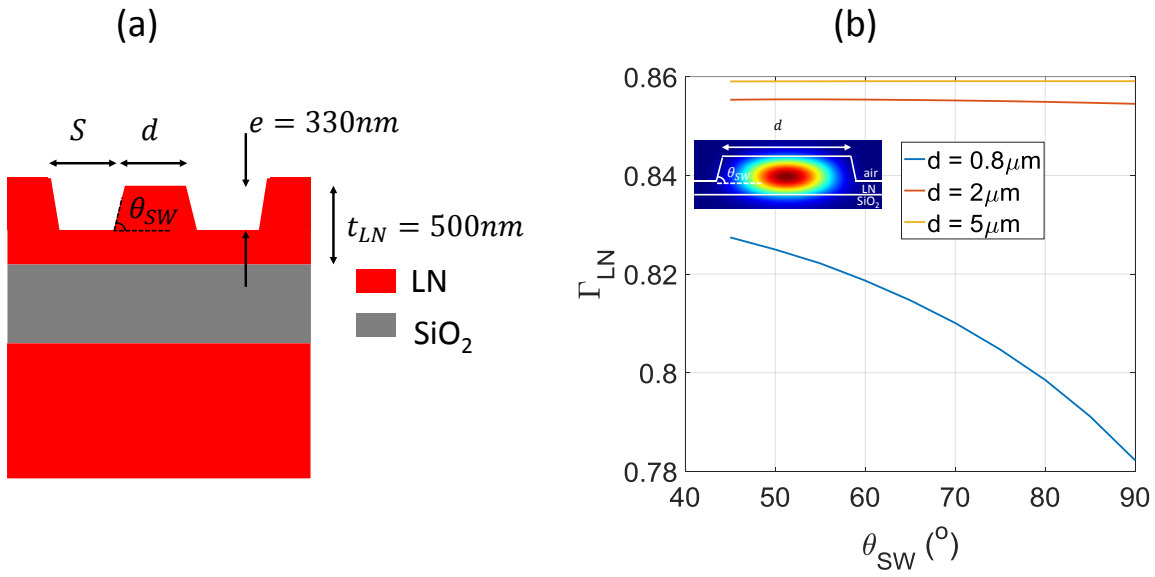

Figure 2.1 (a) Cross sectional view for etched LNOI waveguide. (b) Optical confinement factor of the fundamental mode versus the side-wall angle of the LN etch.

2.2. Process Flow

The fabrication process flow that was used to develop the acousto-optic components in LNOI is depicted in Figure 2.2. The process starts with a Y-cut LNOI 4'' wafer purchased from a third party vendor (NANOLN) [29]. The LN thin film (3'' diameter and 500 nm thickness) was bonded to silicon dioxide (SiO_2, $1\,\mu m$ thick) on an LN substrate using a technique similar to the smart cut technology [30] (Figure 2.2-A). The first step is lift-off of evaporated Al thin film (Figure 2.2-B) which is 100 nm thick and is used to define the electrodes for the SAW and the EOM. After this step, Gold (Au) lift-off is performed (Figure 2.2-C) which is 400 nm thick for patterning the pillars and also for coating the Al pads with Au needed for wire bonding. The next step is deposition of

SiO_2 ($1\mu m$ thick) (Figure 2.2-D) , which is used as a mask layer during the LN etch. Chromium (Cr) (50 nm thick) is then deposited (Figure 2.2-E) and used as a mask for etching SiO_2. This Cr layer is patterned twice. The first pattern is generated with optical lithography to define the waveguides and the racetrack (Figure 2.2-F). The second Cr patterning is performed at the die level using E-beam lithography to define the gratings couplers (Figure 2.2-H). The masks were selected to ensure good selectivity for both etching steps. The choice of a metal as a mask has helped with the E-beam writing step on top of a dielectric stack in terms of reducing the proximity issues and charging effects. The SiO_2 is etched (Figure 2.2-I) in an RIE process using fluorine-based chemistry with Cr mask. The Cr was chosen over other metals like Aluminum (Al) because SiO_2 etch step with Al mask had issues of micromasking causing the gratings etch to stop. Chlorine-based chemistry is used in an ICP process to partially etch the LN (Figure 2.2-J) with the SiO_2 mask where the Cr mask is also removed. The final step is either dry etching in Fluorine or wet etching of SiO_2 (Figure 2.2-K) using Al PAD etch, which is meant to etch the SiO_2 film selectively with respect to the Al pads. The process parameters used for etching the LN are listed in Table 2.1. The selectivity between the LN and SiO_2 was found to be 1:2 and the etch rate is about 60 nm/min. The developed fabrication process enabled integrating metallic Al electrodes together with etched LN waveguides, which is required for building various components like EOMs and AOMs as well as the AOG. The challenge faced with that integration is the removal of the SiO_2 mask as a very last step in the process without attacking the Al electrodes. Various combinations of deposition techniques and wet etchants were tried for that step. Two deposition techniques were tried for the Al which are sputtering and evaporation. The wet etchants tried to etch the SiO_2 selectively with respect to Al include HF50%, BHF, Silox Vapox as well as Al Pad etch. The best results for wet etching was obtained in the combination of the evaporated Al films with Al Pad etch. However, the Al was slightly attacked during that step. Ultimately, dry etching of SiO_2 has proven to be a better approach. the losses in the etched waveguides losses were impacted by that dry etch.

The etch depth for the gratings coupler and the waveguide was chosen to be the same to reduce the fabrication steps. Figure 2.3 shows SEMs for various photonic components fabricated using that process including LNOI waveguides, grating couplers and Y junctions. The tilted views show the sidewall angle which is measured to be 70 degrees for grating coupler and about 75 degrees

for the waveguides. According to previous section, the angled waveguides with 75 degrees provides more confinement than perfectly etched sidewall for narrow waveguide. For wider waveguides, the confinement is the same. For the gratings couplers, no matter what the profile looks like, the wave-vector matching will be achieved as long as the first harmonic associated with the gratings periodicity exists.

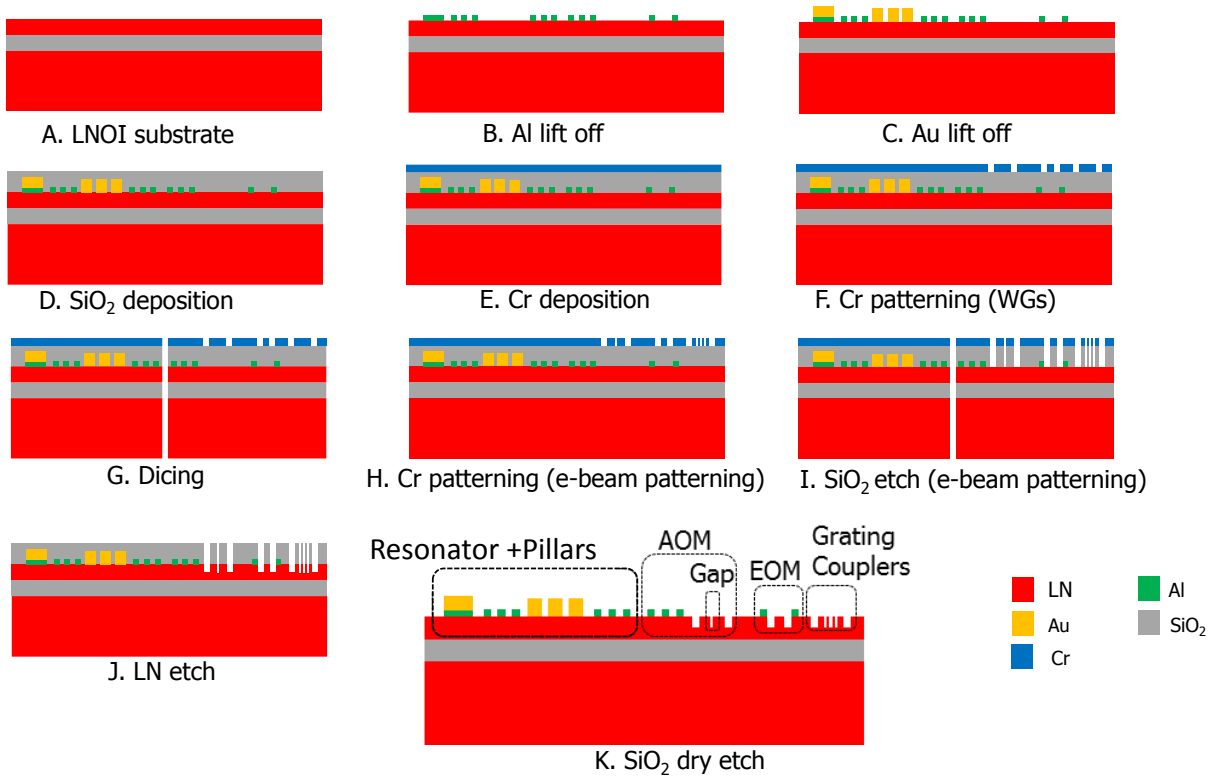

Figure 2.2 Fabrication process flow for the AOG components

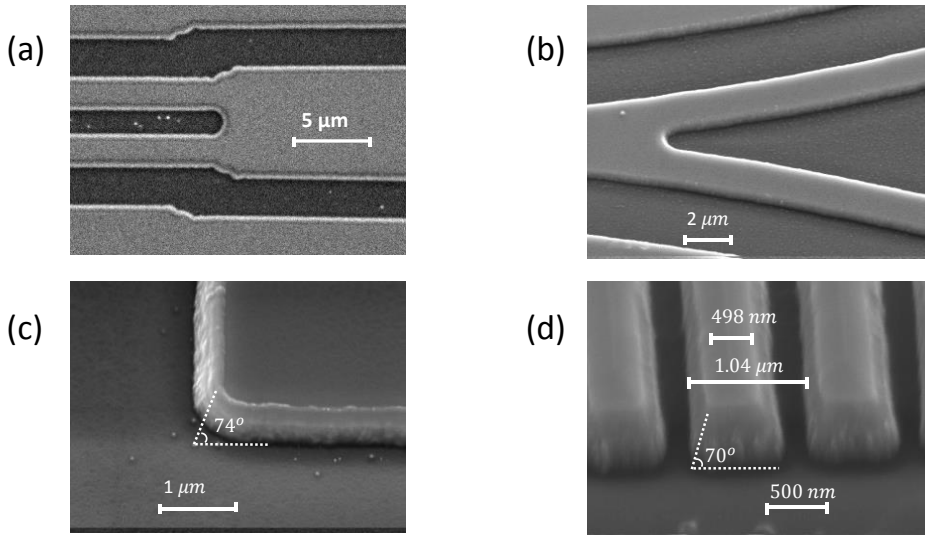

Figure 2.3 Various photonic components etched in LN with the same etch depth. (a) MMI coupler. (b) Y junction. (c) Tilted view for etched waveguies. (d) Tilted side view for the gratings couplers. The side wall angles measured for the waveguide and the grating coupler are 74° and 70° respectively.

Table 2.1 ICP RIE of Lithium niobate recipe

Parameter	**Value**
Cl_2 gas flow	25 SCCM
BCl_3 gas flow	50 SCCM
Ar gas flow	10 SCCM
ICP power	600 W
RF power	250 W

3. Photonic Components

In this chapter, we will study first the LNOI gratings couplers to minimize the insertion loss of the coupled light onto the chip by optimizing the grating design parameters including the pitch, the duty cycle and the etch depth. A finite difference simulation using LUMERICAL is used to study the optical field profile inside the etched LNOI waveguides. As mentioned in the previous chapter, the waveguides and the grating couplers are etched in the same step, thus the analysis of LNOI photonic waveguides will assume the same etch depth and study the size limitation for single mode operation. Finally, this chapter ends with the design of photonic resonators as well as the characterization of the resonator Finesse from which the propagation loss is extracted.

3.1. LNOI Gratings Couplers and Photonic Waveguides

This section begins with introducing the gratings couplers design and the optimization of their dimensions for maximum coupling efficiency. The analysis is then focused on estimating the LNOI waveguide dimensions for single mode operation assuming the same etch depth of the gratings coupler.

i. Gratings Couplers Design

Figure 3.1 shows the proposed geometry for the LNOI grating coupler where buried SiO_2 ($n_3 = 1.44$) is used as a bottom cladding layer. In Figure 3.1, Δ_g is the grating period, δ / Δ_g is the duty cycle, θ_m is the inclination angle of the fiber , e is the etch depth, t_{LN} is the thickness of the LN film and BOX is the thickness of the buried oxide. LUMERICAL [31] finite-difference time-domain (FDTD) was used to calculate the transmission versus the wavelength and further optimize the design for maximum transmission bandwidth product. In the simulation, a $9\mu m$ fiber core of SiO_2 material is coupled to the surface of the top cladding at 8^o incidence angle and centered over the 4^{th} grating tooth from the waveguide. The source injected through the core is a TE polarized

Gaussian beam with $9\mu m$ mode width between $1 / e^2$ points. The grating dimensions were optimized so as to maximize the transmission to the waveguide over a specific bandwidth (equivalently minimize the insertion loss of the coupler), defined as:

$$T_{avg} = \frac{\int_{1.5\mu m}^{1.6\mu m} T(\lambda)\, d\lambda}{\int_{1.5\mu m}^{1.6\mu m} d\lambda} \tag{3.1}$$

Where $T(\lambda)$ is the insertion loss as function of the wavelength. LUMERICAL has a built in optimization algorithm named "particle swarm", which enabled obtaining the optimum design dimensions listed in Table 3.1. The measurement setup for this coupler and the characterization results will be discussed in section iii after the LNOI waveguide analysis is introduced.

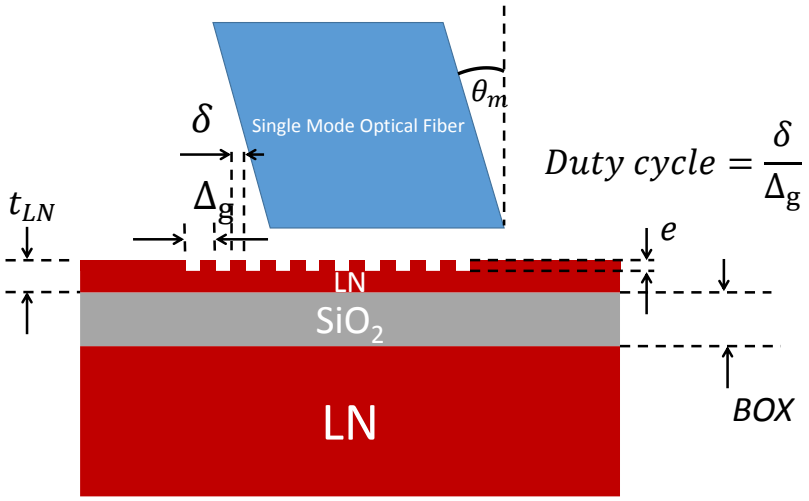

Figure 3.1 Grating Coupler FDTD simulation parameters

Table 3.1 Optimum design dimensions for LNOI grating coupler

Parameter	Value
Δ_g	$1\ \mu m$
δ/Δ_g	0.44
e	$330\ nm$

ii. Photonic Waveguide Analysis

Figure 3.2-a shows a U shaped waveguide that is to be etched in the LNOI platform. Two gratings couplers are separated by the distance $G_s = 250\ \mu m$ which is the separation distance of the readily available V-groove assembly (VGA). The width of the input waveguide was selected to be $W = 17\ \mu m$, which facilitates the alignment to a single mode fiber with a spot size of $9\ \mu m$. Then there is a tapered section, which allows spot size conversion of the guided mode from the input waveguide width of W to the small waveguide width, d. The length of the taper, T, should be sufficient to ensure spot conversion while maintaining losses to a minimum. The waveguide width, d, is expected to be a few microns. The connection between the straight waveguide and the tapered one is through a 90 degree bend with specific radius, R.

Figure 3.2-b shows the cross section view of the straight LNOI waveguide that was simulated using LUMERICAL MODE solver to evaluate the value of the waveguide width, d, required for single mode operation.

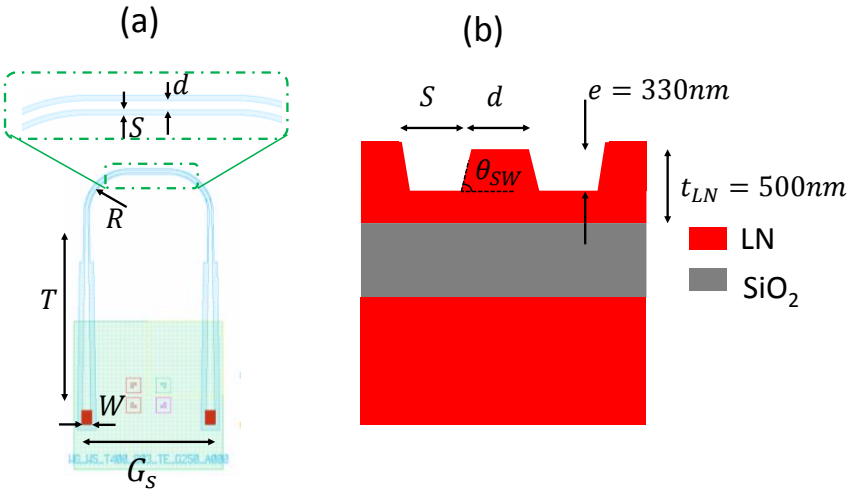

Figure 3.2 (a) U shaped waveguide etched in LN. (b) Cross section view of LNOI waveguide.

A 2D finite difference model was implemented in LUMERICAL to extract the effective index of the guided modes in the LNOI waveguide. The sidewall angle θ_{SW} was set to 75 degrees as that is what was obtained from the fabrication process described in chapter **Error! Reference source not found.**. Figure 3.3 plots the effective index for the first three of the quasi TE modes of the LNOI waveguide. The plot shows that single mode operation exist only for $d < 0.8\ \mu m$. However,

in our fabrication process, the waveguides were defined by a mask aligner, which limited the minimum feature to $2\mu m$. For this reason, all of our fabricated devices have d set to $2\ \mu m$ or larger, hence resulting in multimode waveguides.

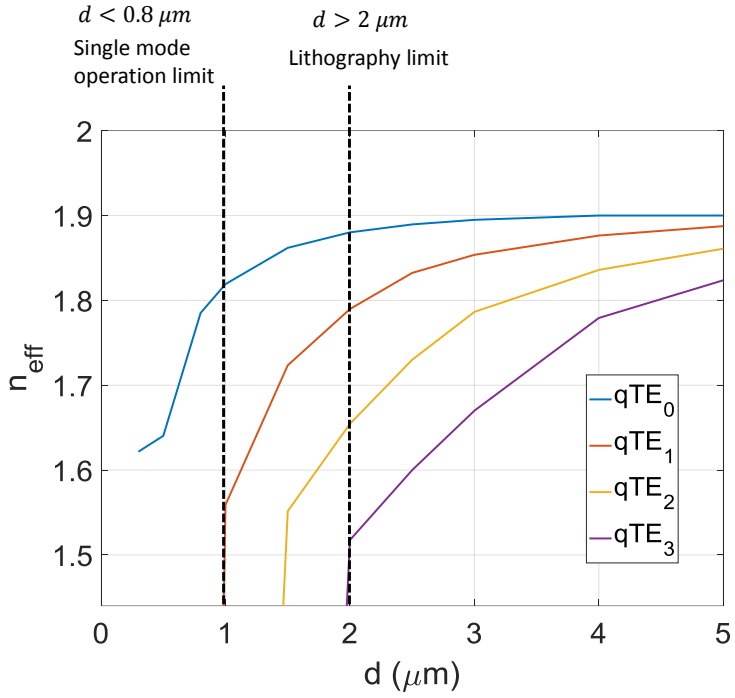

Figure 3.3 Effective index of the guided quasi TE modes versus the waveguide width.

iii. Characterization

The U shaped waveguide with the gratings couplers discussed in the previous sub-sections were fabricated using the process flow introduced in chapter (2 then measured using the setup shown in Figure 3.4. As shown in the figure, the testing of the coupler was carried out on a probe station with a tunable laser source (Santec TSL-510) with a range of 1500-1630 nm and an optical power meter. The Input fiber was fed through polarization paddles to select transverse electric (TE) mode injection to the gratings. After aligning the V-groove to the substrate and positioning the fiber angle about a nominal value of 8 degrees, insertion loss measurements of gratings connected by U-shaped waveguides were made.

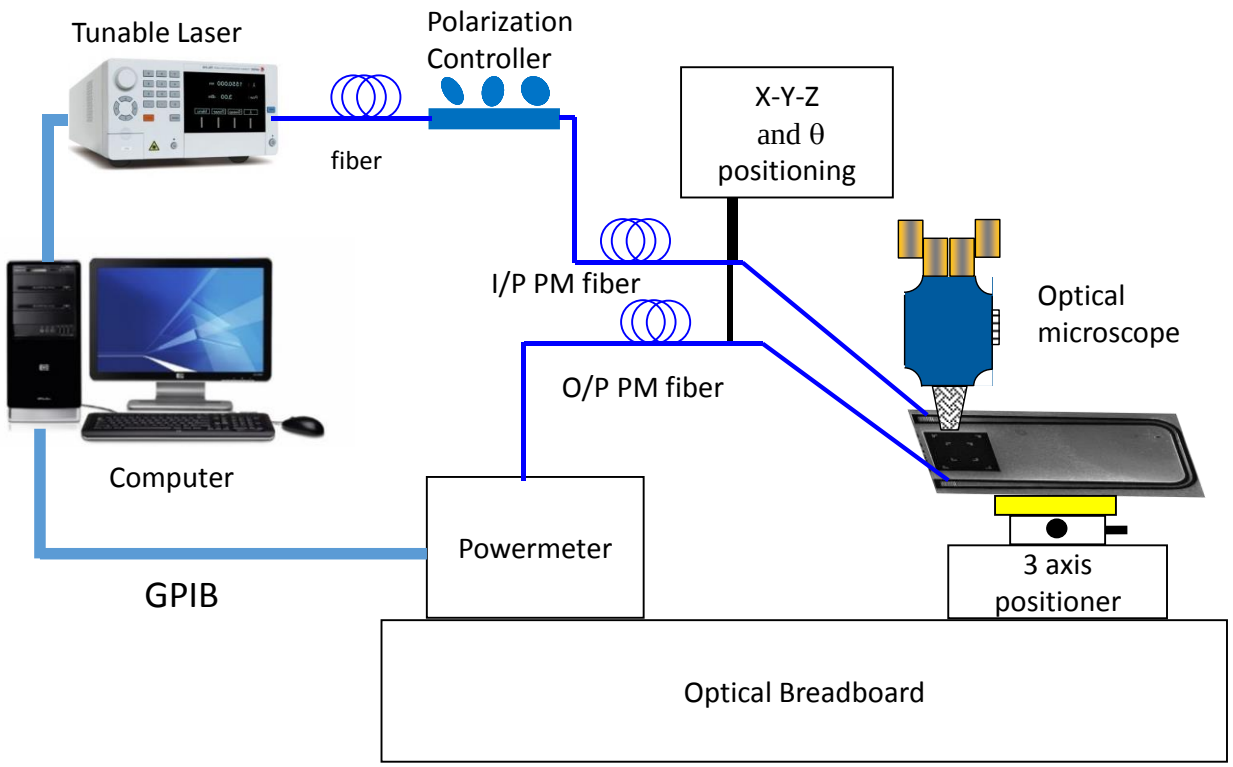

Figure 3.4 Measurement setup for LNOI gratings couplers characterization.

The measured insertion loss per coupler against the wavelength is shown in Figure 3.5. The figure shows the comparison of the FDTD simulated result and the measured response. The simulation yields a peak transmissivity of -4 dB per coupler, while the measured response shows a peak transmissivity of -12 dB. The figure also plots the transmission for the simulated grating coupler considering the actual device dimensions after fabrication as listed in table 1. We believe that the discrepancy between simulation and measurements is to be attributed to the optical setup used in the measurements and the difficulty faced during fiber alignment. Figure 3.5 depicts the aforementioned issue with the setup by showing the effect of a slight misalignment on the measured transmissivity.

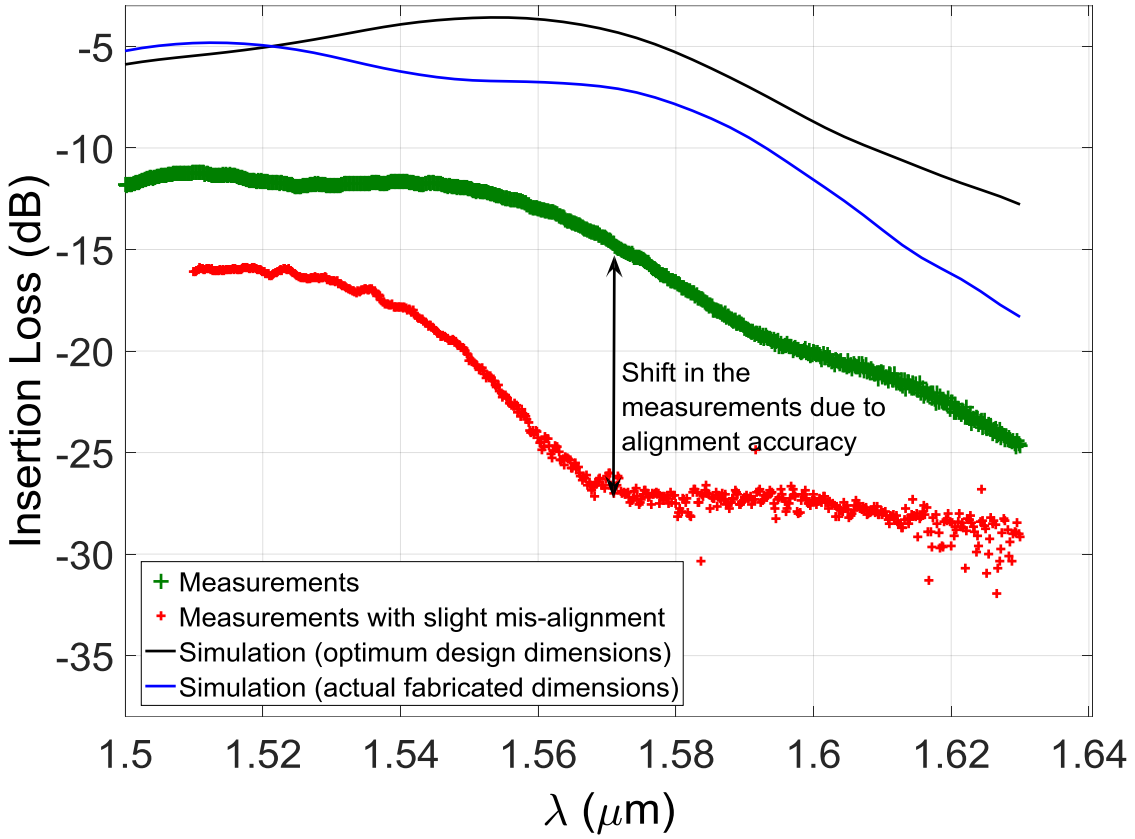

Figure 3.5 FDTD simulated (top, blue and black) and experimentally measured (bottom, red and green) insertion loss for a single grating coupler. The mis-alignment is few microns.

Table 3.2 Comparison between the geometrical parameters for the grating couplers (the optimal design versus actual fabricated values)

Parameter	**Design Value**	**Actual Value**
Δ_g	$1\ \mu m$	$1\ \mu m$
δ/Δ_g	0.44	0.51
e	$330\ nm$	$350\ nm$

3.2. Photonic Resonator

Photonic resonators such as rings, disks or racetracks represent important building blocks not only as phase sensing component in our AOG system, but also in many various applications like optical filters [32], modulators [33], [34], all optical switches [35] and non-linear optical devices [36]. For our particular interest of building the AOG, an important step after building the resonator is the characterization of the Finesse, *F*, of the LNOI resonators and estimating the propagation loss of the etched LNOI waveguides. The next sub-sections begins with introducing the proposed racetrack design followed by the identification of different types of losses inside the racetrack and how to estimate them using LUMERICAL. After which the measurement setup for characterizing the Finesse as well as procedure to extract the propagation loss in dB/cm.

i. Racetrack Resonator Design

Figure 3.6 shows the layout for the proposed photonic racetrack resonator where a 2 x 2 MMI coupler is used to couple light to the racetrack. The geometry of the MMI coupler has a butterfly shape, which is used to target the critical coupling condition needed for maximum extinction ratio. The light is coupled in and out of the chip using grating couplers. Tapered waveguides are used as spot size converters from the wide waveguide at the gratings side to the narrow one that couples to the racetrack resonator. The resonance wavelength is determined by the round trip phase shift inside the racetrack. The grating couplers dimensions are those discussed in section a.i. The separation between the two gratings was set to match the separation in the V-groove fiber array used for measurements, $G_s = 250\,\mu m$. The coupler waveguide width was set to $W = 17\,\mu m$ to facilitate the optical alignment of the single mode fiber ($\sim 9\,\mu m$ core). As discussed in section a.ii, single mode operation for LNOI rib-waveguides is allowed only for width $d \le 0.8\mu m$ at the selected etch depth. Given the constraints on the lithographic equipment used to define the waveguides, their width was set to $d = 2\,\mu m$. The length of the taper was set to $T = 700\,\mu m$ to minimize losses during spot size conversion.

The MMI coupler is used to couple light in and out of the racetrack resonator. It can be modeled as a 2x2 element with two input ports and two output ports such that the output fields, E_3 and E_4 , at ports 3 and 4 are related to the input fields, E_1 and E_2 , at ports 1 and 2 by the equations:

$$E_3 = re^{-j\phi_r}E_1 + te^{-j\phi_t}E_2 \tag{3.2}$$

$$E_4 = te^{-j\phi_t}E_1 + re^{-j\phi_r}E_2 \tag{3.3}$$

Where r and t are the electric field amplitude coupling coefficients for the direct and cross waveguides respectively while ϕ_r and ϕ_t are the associated phase shifts. For a symmetric lossless coupler, the power conservation implies:

$$r^2 + t^2 = 1, \qquad and \qquad \phi_t = \phi_r - \pi/2 \tag{3.4}$$

Accordingly, the losses inside the photonic racetrack can be divided into two parts. The first is coupling loss, r^2, while the second is the intrinsic loss, a^2,so that the transfer function of the racetrack is given by:

$$T = \frac{a^2 + r^2 - 2ar\cos(\phi_l + \phi_r)}{1 + a^2r^2 - 2ar\cos(\phi_l + \phi_r)} \tag{3.5}$$

where $\phi_l = n_{eff}\frac{2\pi}{\lambda}L_T$ is the phase shift due to propagation all the way around the loop except for the MMI coupler such that $L_T = 2l + 2\pi R_r - L_{MMI}$, $n_{eff} = 1.87$ is the effective index of the fundamental mode, $R_r = 100\,\mu m$ is the radius of the curved section, $l = 500\,\mu m$ is the length of the straight section and L_{MMI} is the length of the MMI coupler. The intrinsic loss sources and equations used to model it is discussed in the coming sub-section.

Thus, the critical coupling condition in the racetrack can be expressed as $r^2 = a^2$ and to get an ER larger than 10 dB, a coupling ratio larger than 80% is desired. For that purpose, a butterfly MMI coupler is used since rectangular MMI couplers can be designed only to get discrete and very specific splitting ratios $(r^2/t^2 = 0/100,\ 50/50,\ 72/28,\ 85/15)$ [37]. Eigen Mode Expansion (EME) solver inside LUMERICAL tool was used to design the butterfly coupler. The analysis resulted in an MMI coupler with the dimensions, $W_1 = 10.67\,\mu m$ as inner width, $W_2 = 7.46\,\mu m$ as

outer width and $L_{MMI} = 334.2\,\mu m$ as coupler length for which a coupling coefficient of 83% was achieved.

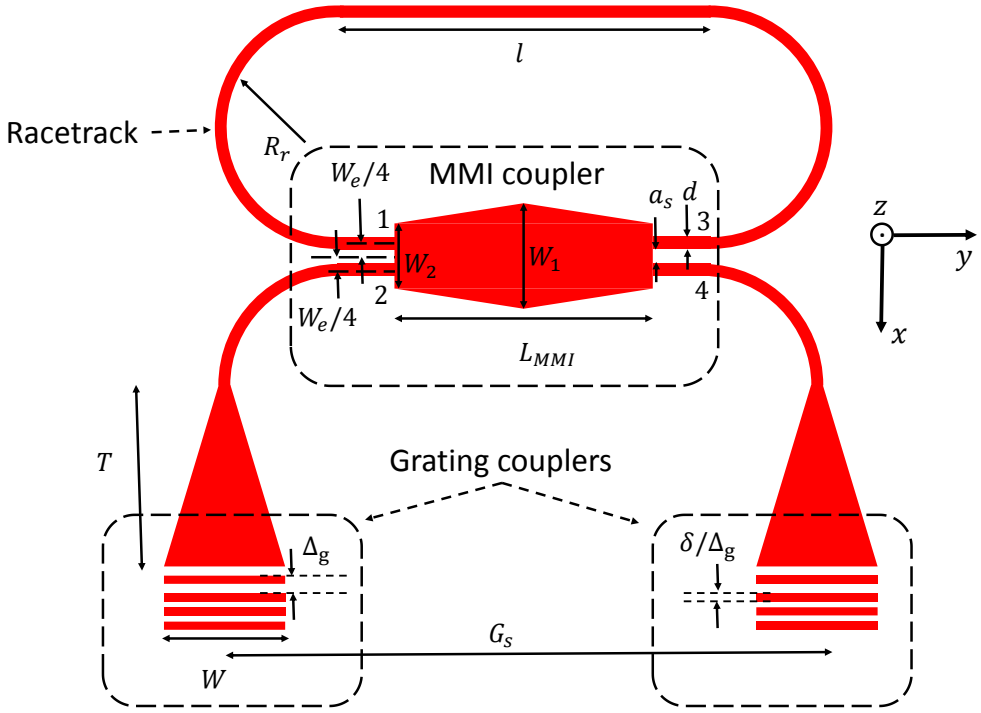

Figure 3.6 Proposed racetrack design. The light is coupled to the racetrack using 2 x 2 butterfly MMI coupler. The gratings are used for in and out of chip couplings.

ii. Intrinsic losses in a photonic racetrack

Intrinsic loss sources can be divided into two parts. The first is the loss in the straight section while the second is the bent waveguides. The losses in a straight photonic waveguide with length l can be modeled as propagation loss, $G_{p_l} = e^{-2\alpha l}$, which includes the materials and scattering losses and α represents the propagation loss coefficient. However, bent waveguides have additional losses identified as the radiation loss, and the mode mismatch loss. The origin of the radiation loss can be explained using ray optics in terms of the change of the angle of incidence, θ_2 (see Figure 3.7), to be smaller than the critical angle for total internal reflection in the bent

section, θ_c. LUMERICAL MODE solver can be used to estimate such losses given the index contrast and the bending radius, R . The mode mismatch loss originates from the fact that the optical field solution is different in the bent section compared to the straight one (see Figure 3.8). The overlap integral between the two fields can be calculated using LUMERICAL to estimate the mode mismatch loss for different radii.

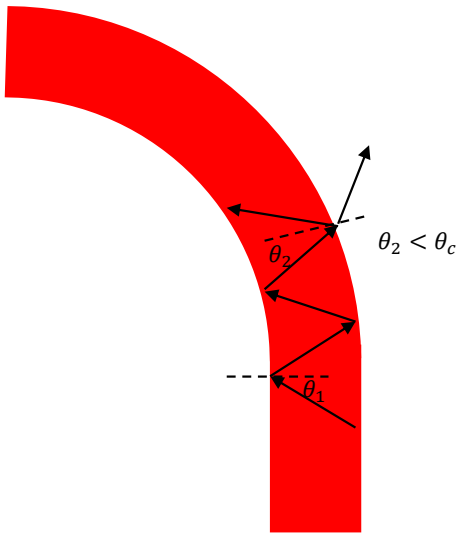

Figure 3.7 Ray picture describing the bending radiation loss

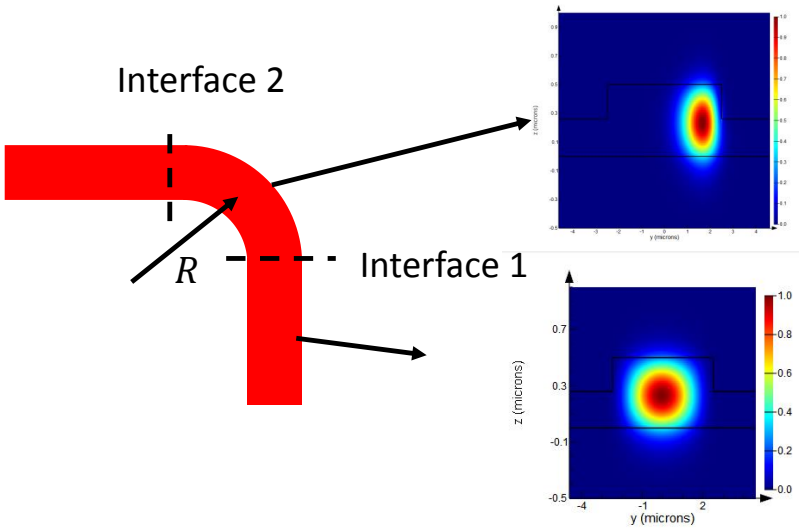

Figure 3.8 Mode mismatch loss for bent waveguide can be evaluated by considering the overlap integral between the optical fields in the bent and the straight sections at the two interfaces.

The modeling of propagation loss is more difficult as it has to include the roughness of the etched waveguide sidewalls as well as possible leakage through the buried oxide. For this reason, our approach is to experimentally measure the losses in the waveguides and extrapolate such propagation losses.

Assuming the MMI coupler has the same losses as the straight waveguide with width, *d*, the intrinsic loss, a^2 , can be expressed mathematically in terms of the bending loss, $G_{B_{180}}$, and the propagation loss for the length l , G_{p_l} , as:

$$10\log\left(a^2\right) = 2G_{\mathbf{B}180} + 2G_{p_l} \tag{3.6}$$

where the subscripts B180 signifies the 180 degree bent waveguide such that the losses inside the bend can be expressed in terms of the radiation loss, $G_{B_{RL}}$, the mode mismatch loss, $G_{B_{MML}}$, and the propagation loss $G_{P_{B180}} = e^{-2\alpha(\pi R)}$ as:

$$G_{B180} = G_{B_{RL}} + G_{B_{MML}} + G_{P_{B180}}$$

Here we have made another assumption that the propagation loss in dB/cm, α, is the same in the straight section and the bent one, which might not be the case given the anisotropicity of the LN crystal and the slightly different etch profile along different crystal directions.

The light coupling loss from fiber to chip, G_T, can be modelled mathematically into the racetrack transfer function by updating equation (3.5):

$$T = G_T \frac{a^2 + r^2 - 2ar\cos(\phi_l + \phi_r)}{1 + a^2 r^2 - 2ar\cos(\phi_l + \phi_r)} \tag{3.7}$$

in which G_T includes also anyloss due to poor alignment between the fiber and the chip. In this way, we can decouple the effect of alignment/coupling losses on the intrinsic propagation losses (a^2)

iii. Measured Finesse and extracted propagation loss

The same measurement setup to characterize the gratings couplers (discussed in sub-section iii) was used to measure the response of the racetrack. The measured transfer function is shown in Figure 3.9. The intrinsic loss, a^2, can be extracted separately by fitting the measured response to equation (3.7). Using LUMERICAL, the bending losses can be estimated and plotted as a function of the propagation loss coefficient (see Figure 3.10). Correspondingly, a value of the propagation loss coefficient $\alpha = 2.45\,dB/cm$ can be extracted.

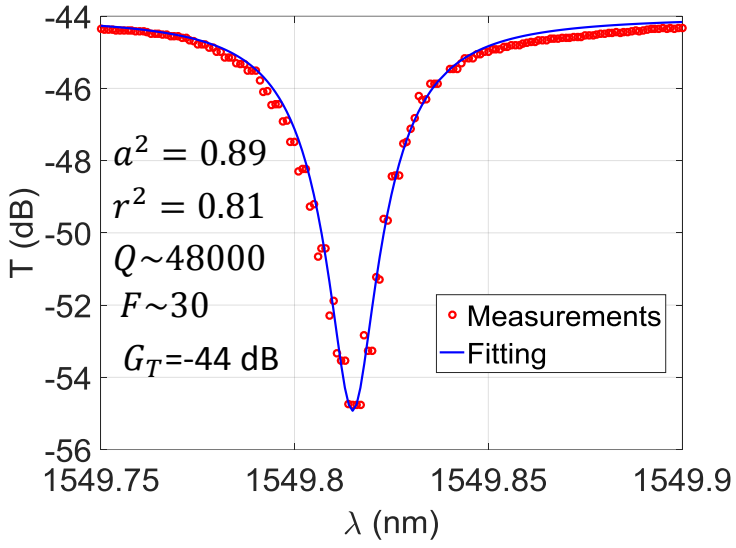

Figure 3.9 Measured transfer function of the photonic resonator

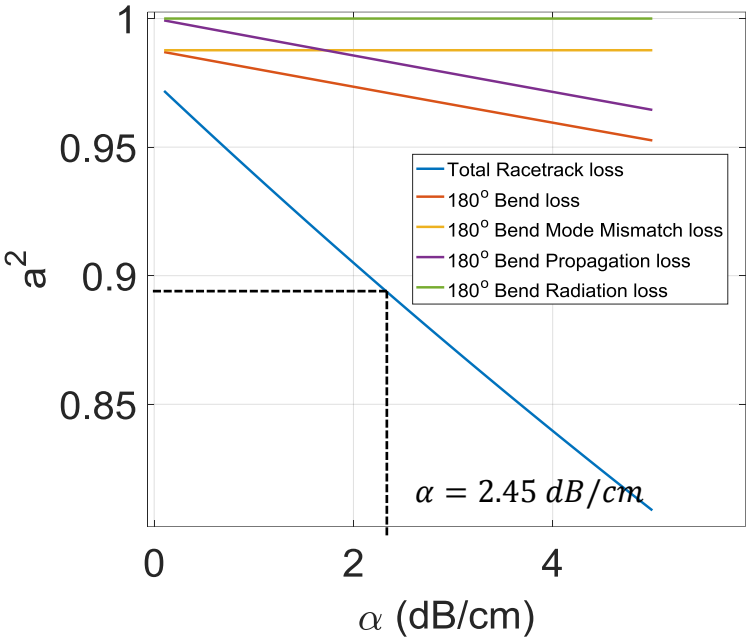

Figure 3.10 Different types of losses inside the resonator versus the propagation loss coefficient.

4. Electro-optic Modulators

Electro-optic modulators (EOMs) represent essential building blocks for various systems and different applications including high speed optical communication, high speed data recording, laser frequency stabilization, pulsed laser generation such as mode locking or Q switching. Our target application is the AOG temperature stabilization. For that purpose, the electro-optic coefficient of the LNOI thin film needs to be extracted from the characterization of EOMs built on that same platform. Two types of EOMs are demonstrated. The first is a racetrack EOM, which is introduced in the first part of this chapter while the second is an Asymmetric Mach-Zehnder interferometer (AMZI) EOM. The AMZI is introduced in the second part of the chapter.

4.1. Racetrack Electro-optic Modulator

Ring or racetrack resonators are important building blocks in integrated optics and very promising in applications including wavelength-division-multiplexing (WDM), cavity quantum electrodynamics (cavity QED), opto-mechanics and high sensitivity sensors[33], [38]–[40]. Electro-optical (EO) tunable racetrack resonators are of particular interest as they can efficiently modulate the photonic signal and work as building blocks of complex and reconfigurable photonic networks [18]. Silicon EOMs have been heavily investigated, but the intrinsic lack of EO property in Silicon limits its performance [41], [42] [43]. On the other hand, the intrinsic strong electro-optic effect of lithium niobate (LN) makes such material an ideal platform for fabricating EO modulators and nonlinear photonic devices [19], [20], [44], [45].

i. Theory of operation and design

The proposed geometry for the racetrack resonator is the same as the one discussed in section 3.2 but with an updated capability, which is the tuning enabled by the electrodes shown in Figure 4.1. The LN racetrack (red in Figure 4.1) and the Aluminum electrodes (green in Figure 4.1) were laid out such that the TE polarized light and the applied electric field are both parallel to the

Z direction of the crystal to make use of the highest E-O coefficient, $r_{33} = 33\,pm/V$. A Gold layer (yellow in Figure 4.1) was also patterned on top of Al to facilitate the probing during device testing.

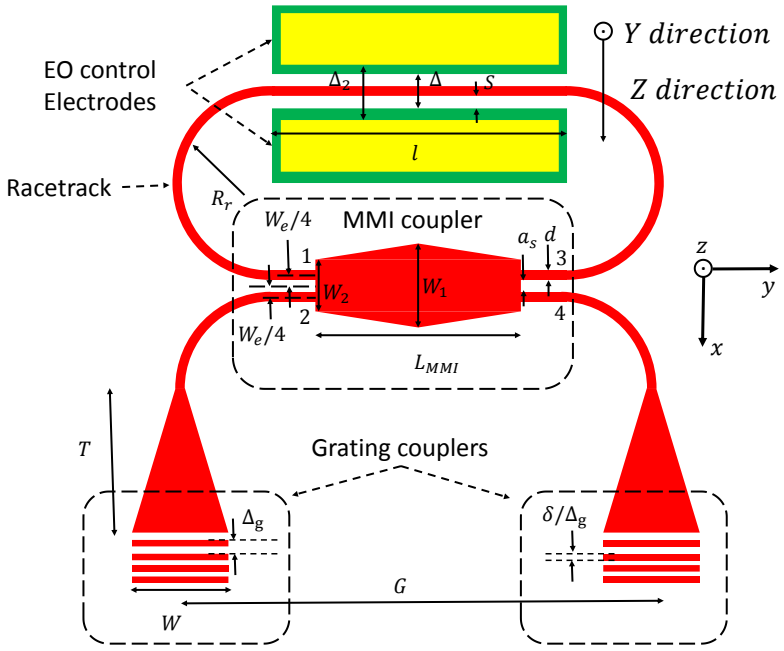

Figure 4.1 Schematic view of the racetrack EOM. Grating couplers are used to couple in and out the light. The Butterfly MMI coupler is used to couple the light inside the racetrack resonator. The resonance condition dictated by the round trip phase shift inside the racetrack is altered by the applied electric field across the electrodes. The higher case symbols X, Y, Z refer to the material axis while the lower case ones x, y, z refer to the simulation axis.

The main parameter that guides the design of the racetrack EOM is the voltage tuning rate, which can be derived to be equal to:

$$TR \approx r_{33} n_{eff}^3 \frac{\lambda_{ro}}{2\Delta} \frac{l}{\left(n_{eff} L_T + n_{MMI} L_{MMI}\right)} \Gamma_{EO} \tag{4.1}$$

Where λ_{ro} is the resonance wavelength at zero voltage , $\Delta = d + 2S$ is the electrode separation, d is the waveguide width, S is the separation from the electrode to the waveguide, $n_{MMI} = 1.907$ is the effective index of the fundamental mode of the MMI waveguide, Γ_{EO} is the overlap between the optical field , $E_{TE}(x,z)$, in the waveguide and the electrical field, $E_{0Z}(x,z)$, between the electrodes and is given by the equation:

$$\Gamma_{EO} = \frac{\Delta}{V} \frac{\int_{-\infty}^{\infty}\int_{-\infty}^{\infty} E_{0Z}(x,z)\,|E_{TE}(x,z)|^2\,dxdz}{\int_{-\infty}^{\infty}\int_{-\infty}^{\infty} |E_{TE}(x,z)|^2\,dxdz} \tag{4.2}$$

For obtaining maximum electric field and hence maximum tuning rate, a minimum separation between the electrodes should be selected. The minimum electrode to waveguide separation, $S_{\min}$, is dictated by the propagation losses introduced by the aluminum near the waveguide. LUMERICAL MODE solver was used to estimate the propagation loss, α_M, in dB/cm for the guided modes of the optical waveguide as a function of the separation distance, S. The subscript M is used to denote that the only losses considered in the model were coming from the Al layer and modeled through an imaginary index of refraction. As shown in Figure 4.2, an $S_{\min}$ of $2.6\,\mu m$ reduces the losses due to the Al layer below 0.1 dB/cm. Note that this value can be reduced to $S_{\min} = 2\,\mu m$ for a SM waveguide. Accordingly, the minimum separation between electrodes is $\Delta_{\min} = 4.8\,\mu m$ for SM waveguide and $\Delta_{\min} = 7.2\,\mu m$ for MM waveguide. However, in our design, Δ was conservatively chosen to be $12\,\mu m$ to ensure no leakage of the optical mode in the aluminum layer.

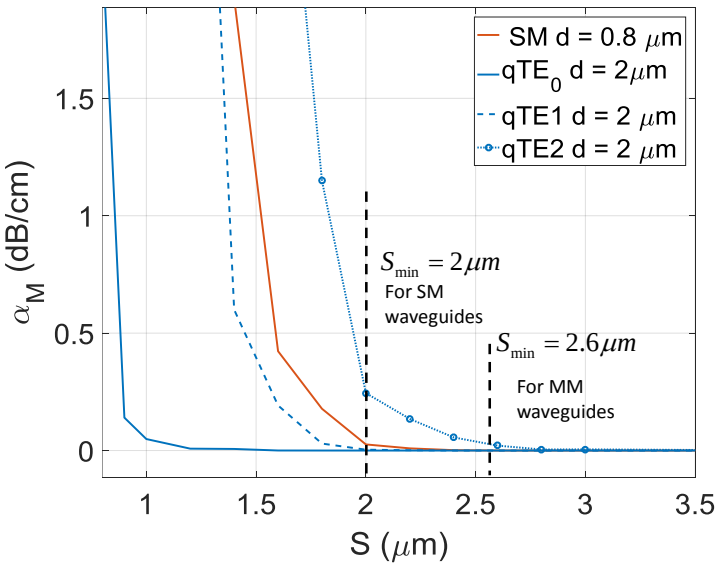

Figure 4.2 Propagation loss of guided modes in dB/cm versus the separation distance between the waveguide and the aluminum metal electrodes.

To evaluate the expected *TR*, the optical and electric field were simulated respectively using LUMERICAL and COMSOL. The overlap between the two fields was evaluated using MATLAB (see Figure 4.3) and the results for Γ_{EO} and TR are summarized in Table 4.1.

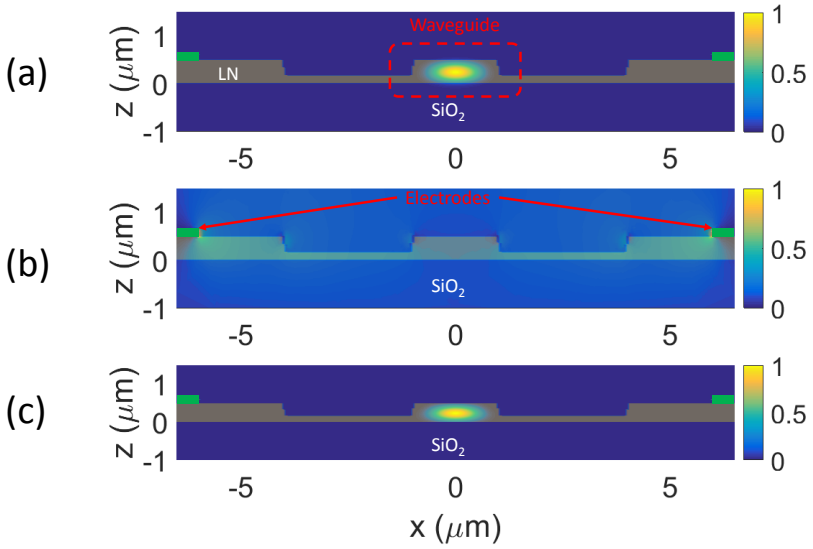

Figure 4.3 a) Normalized optical field inside the waveguide. b) Normalized electric field c) Normalized product of the optical and electrical fields.

Table 4.1 Investigation of the process limitation on the EOM performance for possible improvements

Description	$d\,(\mu m)$	$\Delta(\mu m)$	Γ_{EO}	**TR (pm/V) for current electrode coverage length** $l = 500\mu m$	**TR (pm/V) for same racetrack but with maximum coverage ratio** $l = 960\mu m$
MM (current design)	2	12	0.51	1.1	2
MM – (minimum Δ)	2	7.2	0.5	1.74	3.3
SM	0.8	4.8	0.49	2.2	4.3

The table shows the expected TR for our design and highlights how our proposed fabrication process could ultimately improve the TR if we were to use SM waveguides and minimize the electrode separation. Since the TR increases linearly with the metal coverage ratio, l / L_T, the TR should double when we use the maximum coverage ratio. The overlap factor Γ_{EO} is about 50% in all the cases considered in this study. As shown in Figure 4.3, the LN etch allows confining most

of the optical power in the LN core, which is the EO active material. The overlap factor is still limited by the spatial distribution of the electric field that depends on the ratio between the dielectric constant of LN and air. Using another cladding material like SiO_2 would have helped better confining the electric field in the LN and improve that factor [19].

ii. Characterization

Various values of DC voltages were applied on the EOM electrodes and a TR of 0.38 pm/V was measured (see Figure 4.4). This is approximately 3x lower than the design value (1.1 pm/V). The difference might be related to the fact that Al was slightly attacked during the wet etch step of the SiO_2 as can be clearly seen in the SEM in Figure 4.5. This implies that the electric field was applied across a larger separation, Δ. Assuming that the Al was completely attacked at the edges where there is no Au coverage, the theoretical TR can be re-evaluated as 0.61 pm/V, which is closer to the measured value. We attribute the remaining discrepancy to the material properties of the ion-sliced films.

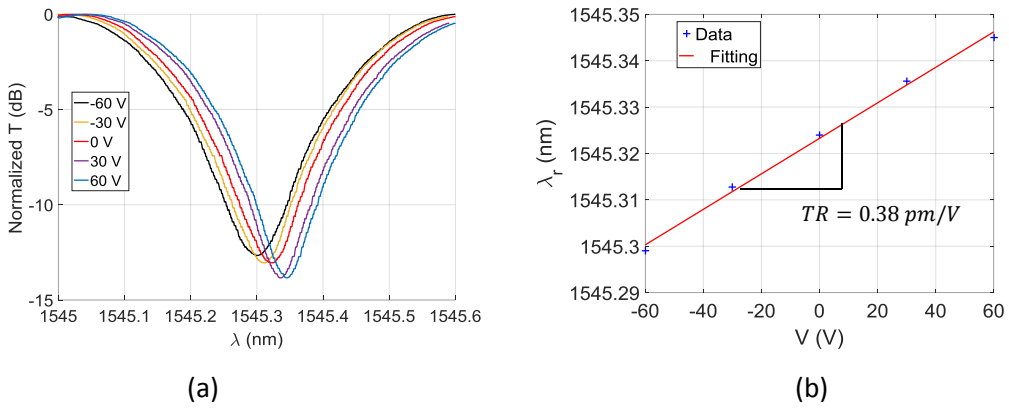

Figure 4.4 Tuning of the resonance condition of the RT EOM by changing the applied DC voltage. a) Measured transfer function for the racetrack at different DC voltages. b) Resonance wavelength for the racetrack as function of the applied voltage. The losses in RT is the one reported in the previous chapter.

High speed modulation was also tested for this device using the setup shown in Figure 4.6. A vector network analyzer (VNA) was used to measure the scattering parameter, $S_{21,}$ of the device. Port 1 of the VNA is used to apply the electrical modulation signal using a GS probe. Port 2 is used to monitor the output of a 1544 New Focus avalanche photodetector (APD) connected to the

output gratings of the racetrack modulator. The measured 3-dB bandwidth is about 4 GHz and is limited mainly by photon lifetime inside the racetrack resonator.

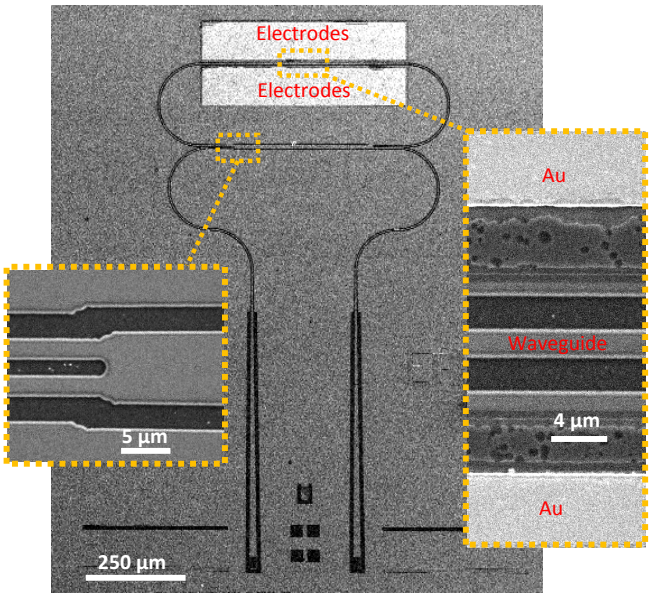

Figure 4.5 SEM for the fabricated RT EOM

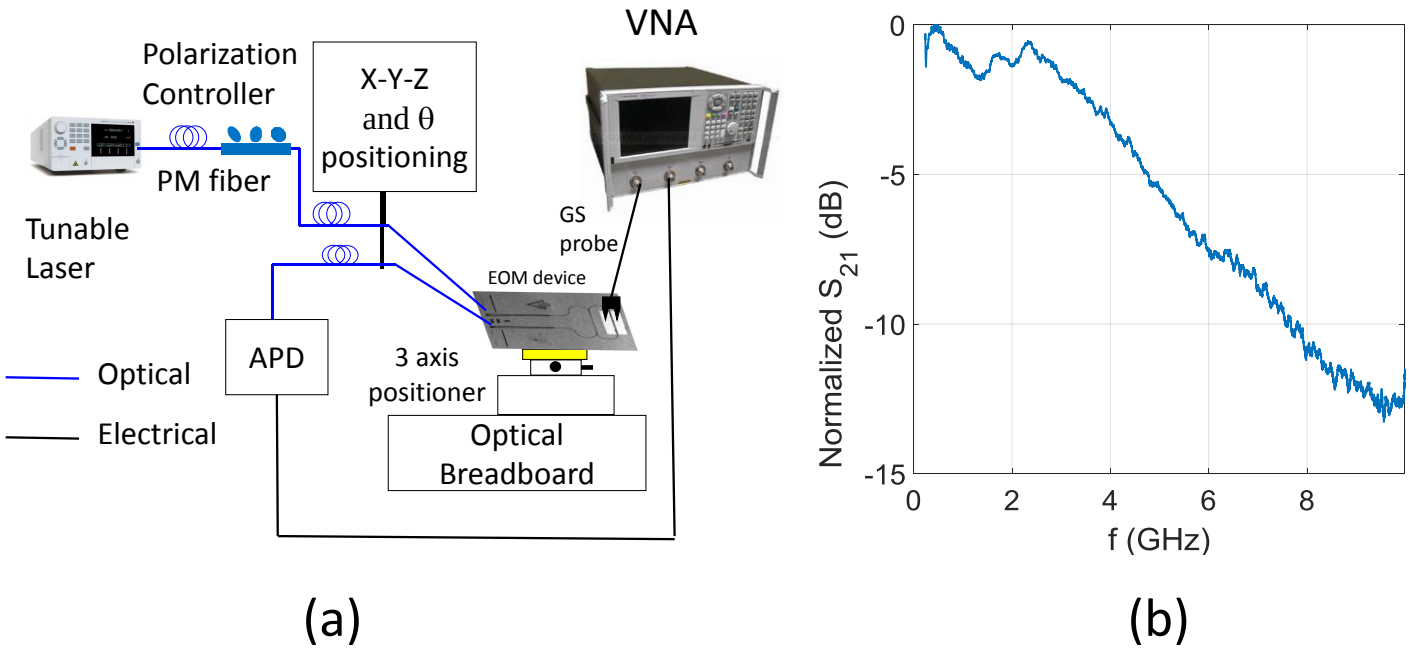

Figure 4.6 (a) Optical setup for high speed modulation. (b) Measured S_{21} for the EOM

4.2. Asymmetric Mach-Zehnder Electro-optic Modulator

In this section, the AMZI is introduced. The purpose of the asymmetry is to get maximum modulation efficiency can be obtained at zero DC bias voltage.

i. Theory and design

Figure 4.7 shows the proposed geometry for the AMZI in which light is coupled in and out using the grating couplers discussed in section 3.a.i. As discussed in the previous section, the electrodes were laid out such that the TE polarized light and the applied electric field are both parallel to the Z direction making use of the highest EO coefficient. Symmetric Y junctions were used as beam splitters and combiners separated by the two arms of the AMZI where each arm has a waveguide with width $d = 2\ \mu m$ (this is a multimode waveguide since the single mode operation requires $d \leq 0.8\ \mu m$ as discussed in section 3.a.ii). To have an unbalanced interferometer, two symmetric S-bends were designed in the lower arm such that the lower arm is longer than the upper one $l_2 = l_1 + \Delta l$. To get maximum slope at zero bias voltage, the S bend shift Δ_B and bending radius R_B were chosen as $\Delta_B = 252.9 \mu m$ and $R_B = 310.3 \mu m$ such that the phase difference at zero bias $\frac{n_{eff} 2\pi}{\lambda} \Delta l = 3\pi/2$ where $n_{eff} = 1.903$ is the effective index that was calculated for the fundamental mode. Thus, the normalized transfer function of the AMZI can be given by the equation $T = (1 - \sin(\beta_{EO} V))/2$ where β_{EO} is the EO modulation factor and V is the applied voltage. Accordingly, the modulation efficiency is given by $\eta_{mod} = \frac{\partial T}{\partial V}\Big|_{max} = -\frac{\beta_{EO}}{2}$ where β_{EO} is given by the equation $\beta_{EO} = \frac{r_{33} n_{eff}^3 \pi l_1}{\lambda \Delta} \Gamma_{EO}$ such that Δ is the electrode separation and Γ_{EO} is the overlap between the optical field, $E_{TE}(x, z)$, in the waveguide and the electrical field, $E_{0z}(x, z)$,between the electrodes and is given by equation (6.20).

An analysis similar to the one in the previous section is repeated for the losses in the waveguide due to the metal refractive index considering the wide waveguide, *d = 5 μm*. The result shown in Figure 4.8 where $S_{min}$of 2.6 μm is allowed the MM wide waveguide which measns $\Delta_{\min} = 11.4\ \mu m$. However, in our design, Δ was conservatively chosen to be $12\ \mu m$ to account for possible mis-alignment between masks.

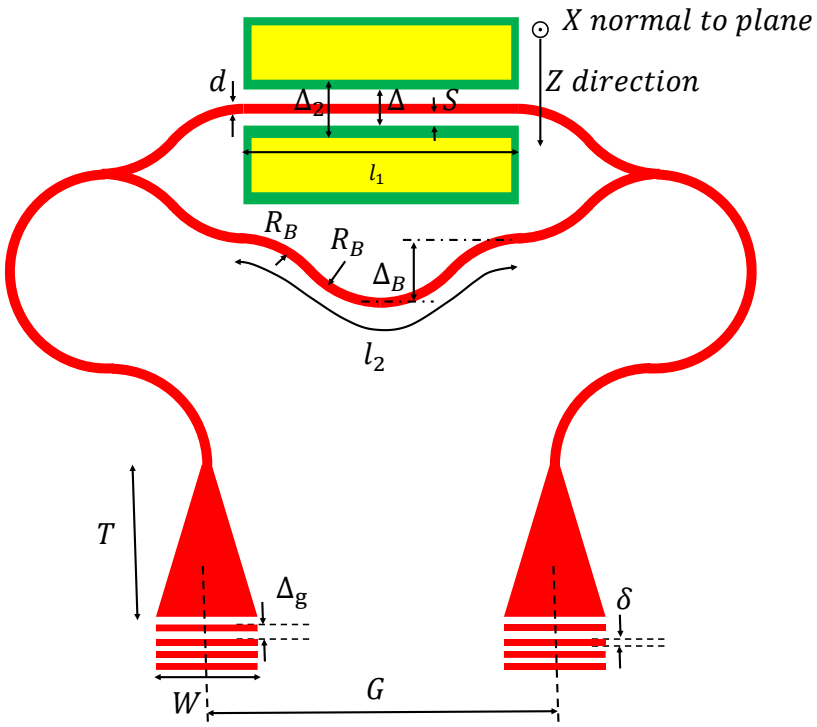

Figure 4.7 Schematic representation of the AMZI

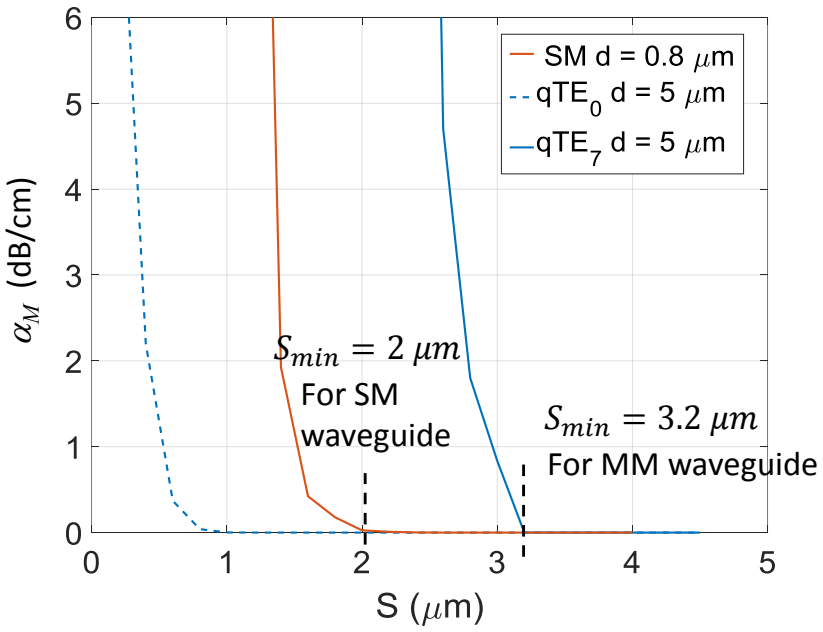

Figure 4.8 Propagation loss due to the imaginary refractive index of the metal as function of the electrode to waveguide separation.

As discussed in the previous section, the EO overlap, Γ_{EO}, can be estimated using COMSOL, LUMERICAL and Matlab in case of the wide waveguide to be equal to 0.47. Accordingly, η_{mod} and the half wave voltage length product $V_\pi l_1 = \frac{\pi}{\beta_{EO}} l_1$ can be estimated to be equal to $\eta_{mod} = 9 \times 10^{-3}\text{V}^{-1}$ and $V_\pi l_1 = \frac{\pi}{\beta_{EO}} l_1 = 17.4\, Vcm$ respectively.

ii. Characterization

The AMZI device was fabricated using the process flow described in chapter 2. Figure 4.9 depicts the SEM for the fabricated AMZI while Figure 4.10 shows the measured transfer function for the AMZI compared with the theoretical expectations. The modulation efficiency extracted from the measurement and the half wave voltage are $\eta_{mod} = 9.4 \times 10^{-3}\text{V}^{-1}$ and $V_\pi l_1 = 16.8 Vcm$, respectively. These results match closely with theoretical expectations except for the slight shift of position of the maximum slope from zero bias, which is attributed to mismatch between the straight and the bent AMZI arm. Although the half wave voltage product is higher than what was reported previously in literature [46] ($V_\pi l_1 = 1.8\, Vcm$) because we are using wide LNOI waveguides, the extracted values from measurement agrees well with the theory and confirms that we can integrate the EOMs in the AOG for the purpose of temperature compensation.

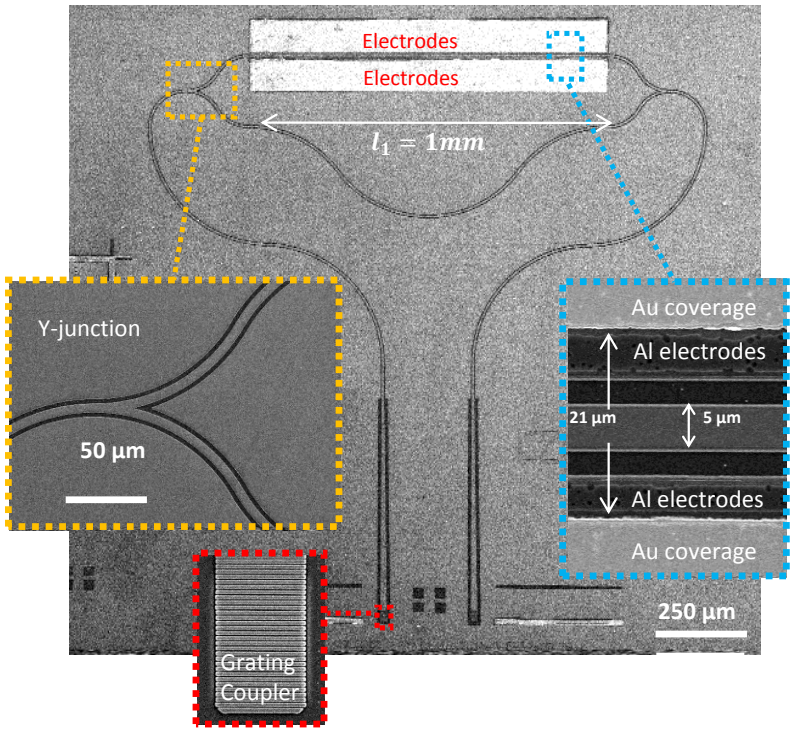

Figure 4.9 SEM for the fabricated AMZI

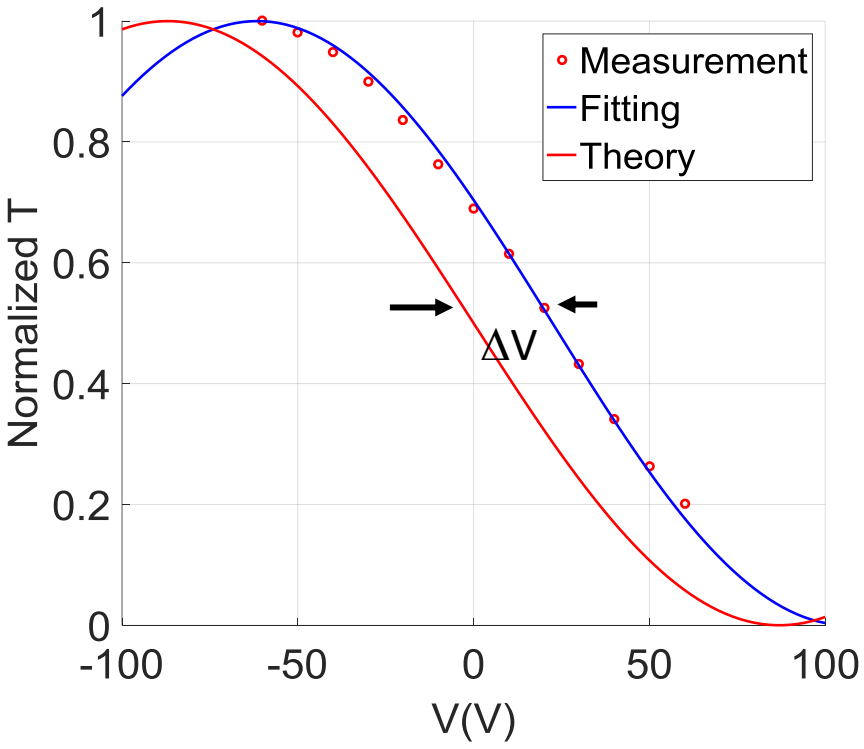

Figure 4.10 Measured response for the fabricated AMZI.

5. Acousto-optic Modulators

Interaction between acoustic and light waves have been widely used to build various devices including modulators [4], [39], [47]–[50], frequency shifters [51], [52], beam deflectors and scanners [53], tunable filters [54], imaging [55], spectral analyzers [56], [57], as well as holographic illumination [58]. In contrast to bulk acoustic waves, Surface Acoustic Waves (SAWs) propagate on the surface of piezoelectric materials in acoustic modes confined within a depth that is equal to a small percentage of the acoustic wavelength [59], [60]. Therefore, SAW can have very high energy confinement and attain large overlap with the optical modes of the planar waveguides to achieve efficient AO modulation in compact devices. Materials with high AO coefficients like Gallium Arsenide (GaAs) or Lithium Niobate (LN) were previously used to build integrated AO modulators (AOM) on various platforms [61]–[63]. For prior LN modulators, the waveguides were defined by Titanium in-diffusion, which limited the optical power confinement in the waveguide due to low the index contrast and hence the AO interactions [63]. For GaAs previously reported AOMs, the AO interaction was limited by the interaction time between the SAW and the optical mode [61], [62]. Although the AO coefficient of GaAs is much higher than that of LN (15x) [64], the electromechanical coupling coefficient, k_t^2 of LN (~5% for bulk LN [65] and ~1.2% for LNOI) is much higher than that of GaAs (~0.07% for bulk GaAs [66]), which improves the overall performance of the modulator. Two different types of LNOI AOMs are demonstrated in this chapter, one is based on a resonant SAW cavity while the other is based on a wideband transducer. Having higher k_t^2 material impacts the design of each one in a separate way. For a resonant SAW cavity, building SAW resonators with high Q and smaller area needs a higher k_t^2 material. For a SAW reflector with N_{ref} fingers, each with reflectivity r, the overall reflection coefficient depends on the product N_{ref} x r [67] and since the LNOI platform provides 17x improvement in the k_t^2 over GaAs/AlGaAs one, the modulator area would scale down by the same amount if it were to be built on that platform.

On the other hand, for the broad band IDT, a higher k_t^2 enables designing transducer with high transduction efficiency between the electrical and mechanical domains with wider bandwidth IDTs. The integration with efficient electro-optic (EO) tuning is an additional advantage for LN since the EO coefficient for LN (30 pm/V [68]) is 30x higher than that of GaAs (1.1 pm/V [69]) as will be discussed in section 5.2.

5.1. SAW Enhanced MZI AOM

In this AOM, we have further enhanced the AO interaction by placing a Mach-Zehnder interferometer (MZI) [25] inside a SAW resonator operating at 116 MHz, hence exploiting the high Q of the SAW cavity. An analytical expression that reflects the enhancement due to SAW resonance is derived in a closed form assuming the waveguides are properly placed inside the SAW cavity at the positions of maximum strain. The experimental results confirm the theoretical model and showcase the AO capabilities of the LNOI platform.

i. Theory and design

Figure 5.1 shows the layout view for the proposed AOM with zoomed-in SEMs of its various components. The figure shows a symmetric SAW cavity with two interdigitated transducers (IDTs) and two reflectors with two photonic waveguides in between that form the MZI arms. Applying electrical signal over the IDT induces an acoustic wave inside the SAW cavity. By properly placing the waveguides inside the cavity at the locations of maximum strain of the generated standing wave, maximum modulation can be harnessed from that modulator. The light is coupled in and out of the MZI using grating couplers. A Y junction is used for splitting the optical input into the two arms of the MZI and a 2x2 multimode interference (MMI) 3-dB coupler is used as a beam combiner. The differential output is detected using a balanced photodetector.

The induced change in the waveguide refractive index tensor, n_K, due to the elasto-optic effect is given by [59]:

$$\Delta n_K = -\frac{1}{2} n_K^3 p_{KL} S_L \quad (K, L = 1, 2...6) \tag{5.1}$$

with p_{KL} and S_L representing the contracted effective elasto-optic coefficient tensor and the strain field tensor, respectively [59]. The repeated index in the subscript implies summation over that index. For materials with high electro-optic, r_{Kj} , and piezoelectric, e_{iL} , coefficients such as LN, the induced electric field due to strain by virtue of the piezoelectric effect will also modulate the refractive index. Thus, the contribution of the indirect electro-optic effect can be lumped into the elasto-optic effect by defining an effective elasto-optic coefficient as [59]:

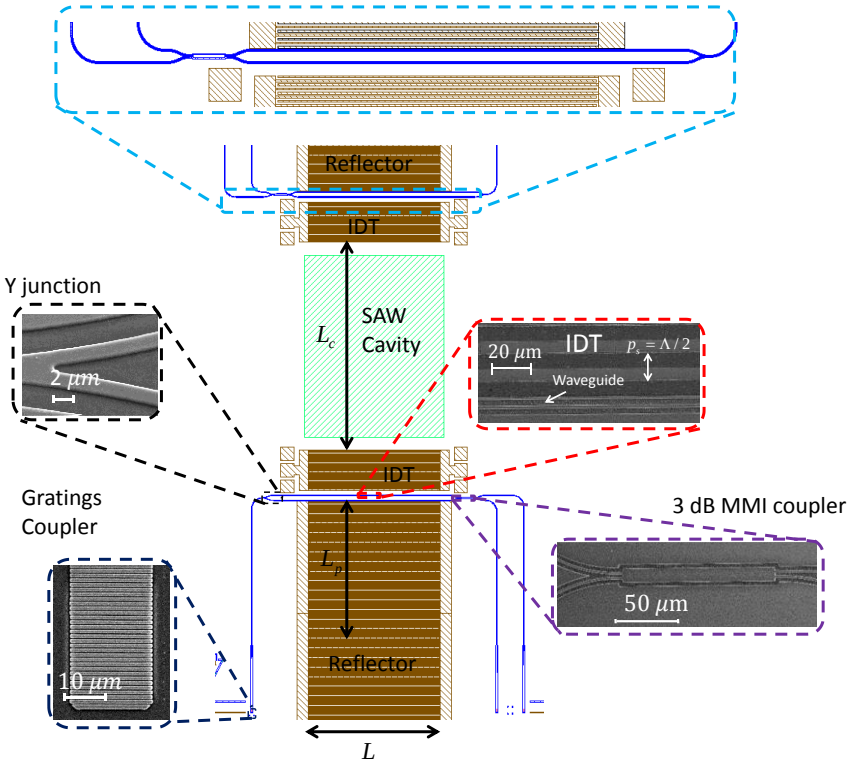

Figure 5.1 Layout view for the proposed AOM. The MZI is placed between the IDT and the SAW reflector.

$$p_{KL}^{eff} = p_{KL} - \frac{\left(r_{Kj} l_j\right)\left(l_i e_{iL}\right)}{\left(l_i \varepsilon_{ij}^S l_j\right)} \tag{5.2}$$

where l_j is the unit vector along the SAW propagation direction and ε_{ij}^S is the permittivity tensor at fixed strain. For a Rayleigh SAW wave, the strain field vector of the surface acoustic wave propagating along the x-axis can be expressed as: $\left(S_1 \quad 0 \quad S_3 \quad 0 \quad S_5\right)$, where S_1 and S_3 are the normal strain fields along the x and z-directions, respectively, and S_5 is the shear strain field. COMSOL Finite Element Method (FEM) was used to estimate the relative amplitudes of those

strain components in the case of Y- cut LNOI wafer as well as the electric potential, ϕ_s . The normalized amplitudes of those strain components are plotted versus the propagation direction, x , in Figure 5.2. over a distance of one period of the standing wave which is one half of acoustic wavelength ($\Lambda/2$). The figure depicts that the longitudinal strain components S_1 and S_3 have the same periodic dependence of the potential ϕ_s whereas the transverse component S_5 has a phase difference of $\pi/2$ which is equivalent to $\Lambda/4$ propagation distance. Thus, placing the MZI arms at the locations of the S_1 and S_3 maxima is a proper design solution. In the following subsections, we will describe: a) the locations of the MZI arms inside the SAW cavity and derivation of the modulation enhancement due to SAW resonance; b) the derivation of the MZI transfer function and the modulation harmonics; c) the SAW resonator design d) the design of the gratings couplers and MMI coupler.

The MZI arms are located between the IDT and the SAW reflector as shown in the cross section view in Figure 5.3. Maximum elasto-optic modulation is attained by placing the MZI arms at the strain maximum position as shown in the same figure. The two strain components, S_1 and S_3 have maxima at the same locations and they both contribute to the modulation. Thus, the spacing between the IDT last finger and the left waveguide is $L_{IDT\_WG} = 3\Lambda/4$. The spacing between the two waveguides, L_{WG_MZI}, is set to $3\Lambda/2$ to enable push-pull operation for the MZI such that when one arm is under compression, the other is under tension. Finally, the spacing between the last finger and the right waveguide is $L_{WG\_ref} = 3\Lambda/8$ which enables maximum strain at the waveguide location.

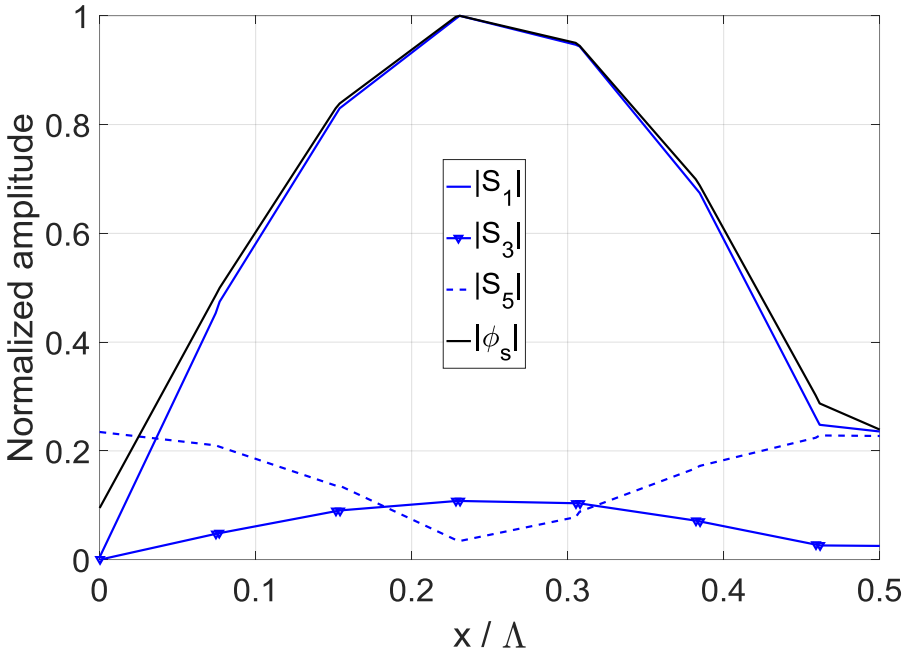

Figure 5.2 Normalized amplitudes of the Rayleigh SAW strain components and the potential versus the propagation distance x. The longitudinal component S_1 has the highest amplitude among the various strain components with standing wave pattern matching that of the potential, φ_s .

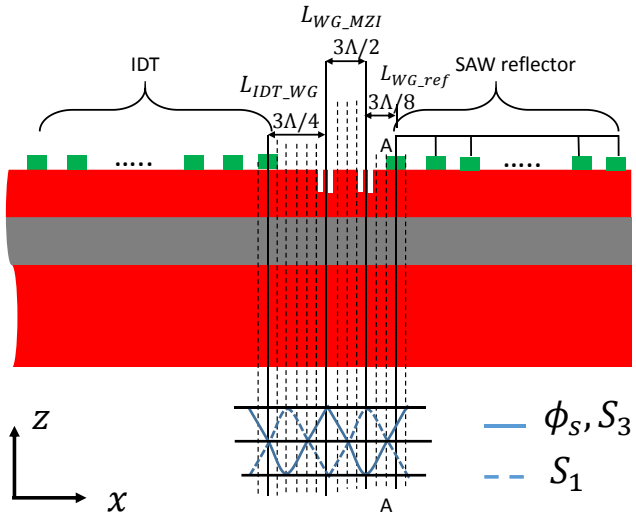

Figure 5.3 Standing wave pattern inside the SAW cavity

By placing the waveguides at these positions and considering the overlap between the optical field distribution, $E_{TE}(x,z)$, inside the waveguide and the dominant strain field distribution,

$S_1(x,z)$, eq. **Error! Reference source not found.** can be modified assuming the perturbed waveguide solution [48], [59], [70] as:

$$\Delta n = \frac{1}{2} n^3 p_{11}^{eff} \frac{\iint S_1(x,z)\left|E_{TE}(x,z)\right|^2 dxdz}{\iint \left|E_{TE}(x,z)\right|^2 dxdz} \tag{5.3}$$

Since we are dealing with SAW standing waves inside the SAW cavity, the strain dependence on the spatial variables x and z can be separated such that it is an exponential decaying function in the z direction, $s(z)$, and a sinusoidal one in the x direction, $\sin Kx$, where $K = 2\pi/\Lambda$ is the SAW wavenumber:

$$S_1(x,z) = |S| s(z) \sin Kx \tag{5.4}$$

Where $|S|$ is the strain amplitude which can be related to the energy density, U , inside the SAW cavity through the elastic modulus tensor, C_{LK} , by the equation $U = \frac{1}{2} S_L C_{LK} S_K$ and by considering only S_1 as the dominant strain component and integrating over the resonator volume, the total energy, E , can be found as:

$$E = \frac{1}{4} C_{11} |S|^2 L_c' LH \tag{5.5}$$

Where $L_c' = L_c + 2L_p$ is the total cavity length including the separation between the IDTs, L_c (see Figure 5.1) and the SAW penetration depth inside the reflector, L_p , L is the aperture length and H is the SAW penetration depth which is given by [59]:

$$H = \int_{-\infty}^{0} \left|s(z)\right|^2 dz \tag{5.6}$$

The energy stored inside the SAW cavity is related to the dissipate power, P and the quality factor, Q by the equation:

$$Q = \frac{\omega_m E}{P} \tag{5.7}$$

Where $\omega_m = 2\pi v_R/\Lambda$ is the radial resonance frequency, v_R is the phase velocity of the Rayleigh SAW wave on the LNOI substrate, which is estimated from COMSOL to be equal to 3420 m/s. The elastic modulus can be approximated as $C_{11} \approx \rho v_R^2$ where ρ is the mass density and by combining equations **Error! Reference source not found.**) and **Error! Reference source not found.**), the strain amplitude inside the cavity can be derived to be equal to:

$$|S| = \sqrt{\frac{2\Lambda Q}{\pi L_c}\frac{P}{LH\rho v_R^3}} \tag{5.8}$$

However, the strain amplitude expected from a transducer without the resonance cavity is given by [71]:

$$|S| = \sqrt{\frac{P}{LH\rho v_R^3}} \tag{5.9}$$

Comparing eqs (5.8) and (6.20), we can see that in the presence of a SAW cavity there is an enhancement in the strain amplitude by a factor proportional to the square root of $\Lambda Q / L_c$. Accordingly, the phase shift in the MZI arms can be calculated considering the amplified strain as:

$$\varphi = 2\left(2\pi / \lambda\right) L\Delta n \tag{5.10}$$

The factor of 2 in eq. (6.20) accounts for the push-pull operation. Thus, the phase shift as a function of the square of the acoustic power, $\varphi = a_p\sqrt{p}$, can be derived by combining equations (5.3) to (6.20) as:

$$a_p = \frac{2\pi}{\lambda}\sqrt{L}\sqrt{M_2}\Gamma_{AO}\sqrt{\frac{2\Lambda Q}{\pi L_c}}\sqrt{\frac{1}{H}} \tag{5.11}$$

Where $M_2 = \left(n^6\left(p^{eff}\right)^2\right) / \left(\rho v_R^3\right)$ is the AO figure of merit (FOM) of LN, Γ_{AO} is the AO overlap and is given by:

$$\Gamma_{AO} = \frac{\iint s(z)\sin Kx\left|E_{TE}\left(x,z\right)\right|^2 dxdz}{\iint\left|E_{TE}\left(x,z\right)\right|^2 dxdz} \tag{5.12}$$

Error! Reference source not found. plots the normalized decaying function $s(z)$ estimated using COMSOL and shows that the SAW strain is confined near the top of the LNOI wafer (within 20% of the acoustic wavelength $\Lambda = 30\mu m$). This 20% is much larger than the LNOI thin film dimensions shown in the inset of **Error! Reference source not found.**. This inset highlights the product of the optical field inside the waveguide and the strain field, hence showcasing that a high AO overlap exists between the SAW and the optical field inside the etched waveguides. The optical field was estimated using LUMERICAL mode solver for a waveguide with dimensions $d = 2\mu m$

as waveguide width and $e = 330nm$ as etch depth. The width of the waveguide is determined by the lithographic resolution of the equipment used in this work, while the etch depth is set equal to the gratings coupler etch depth to simplify the overall AOM fabrication. Using equation **Error! Reference source not found.**, a_p can be estimated to be equal to $a_p = 12\,rad/\sqrt{Watt}$ which is about 3x higher than what's previously reported on AlGaAs platform [62]. Taking into account that the AO FOM of GaAs is about 15x higher than that of LN [64], this enhancement in a_p is mostly attributed to the Q of the SAW cavity.

The normalized differential transfer function of the MZI can be derived in terms of the phase difference, ϕ, as $T_{MZI} = \sin(\phi + \delta_s)$ where δ_s accounts for the slight phase difference due to the mismatch between the two MZI arms. Accordingly the amplitudes of the modulation harmonics, H_i , can be derived to be equal to:

$$H_1 = J_1\left(a_p\sqrt{P}\right)\cos(\delta_s) \tag{5.13}$$

$$H_2 = J_2\left(a_p\sqrt{P}\right)\sin(\delta_s) \tag{5.14}$$

$$H_3 = J_3\left(a_p\sqrt{P}\right)\cos(\delta_s) \tag{5.15}$$

where J_i is the ith order Bessel function for the first kind. Equations (5.1) to (6.20) where implemented using MATLAB and the results are compared with the measurement in the measurement section.

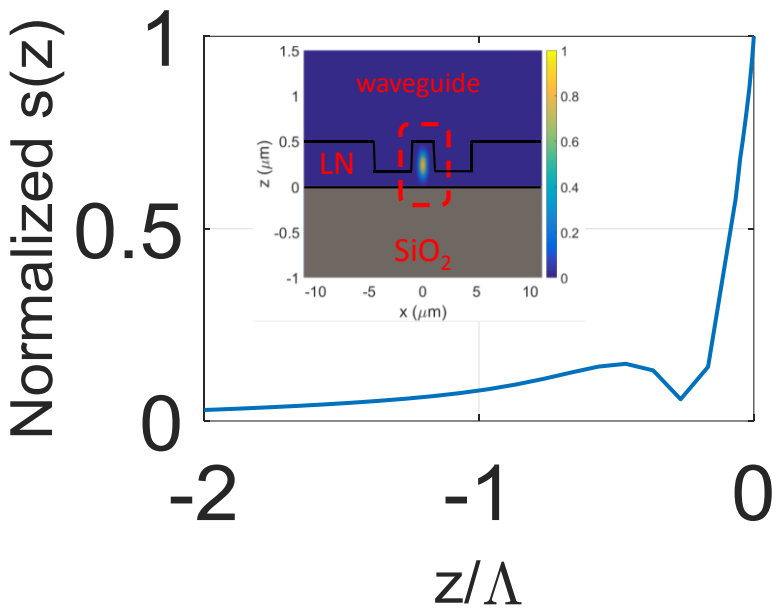

Figure 5.4 Normalized *s(z)* as function of the depth of the LNOI wafer. The inset is the product of the strain field and the optical field.

To properly confine the SAW inside the acoustic cavity and hence maximize Q , SAW reflectors with a high numbers of fingers (700 finger each side) are used. The spacing between IDTs is selected to be $L_c = 40\Lambda$. The number of IDT fingers ($N_{IDT} = 43$) is selected to achieve 50 Ω matching. The metallization ratio of the IDT and SAW reflectors, $\eta = 50\%$, and pitch, $p_s = \Lambda / 2$, are selected to ensure matching the frequencies of both the IDT and the reflector.

The length and width of the MMI coupler are chosen to be $118.1\mu m$ and $11.6\mu m$, respectively to ensure 3-dB splitting around 1550 nm (optical wavelength).

ii. Measurement Results

The frequency response of the SAW resonator is measured using a vector network analyzer (PNA N5230A) and RF probing. The measurement result is shown in Figure 5.5 where resonance can be seen at *f = 115.5 MHz*. The measurement show other spurious modes but since in the AOM measurement we are using Phase Locked Loop (PLL) to lock to the resonance at 115.5 MHz, those mode can be neglected. The extracted Q from the measurement is 2300.

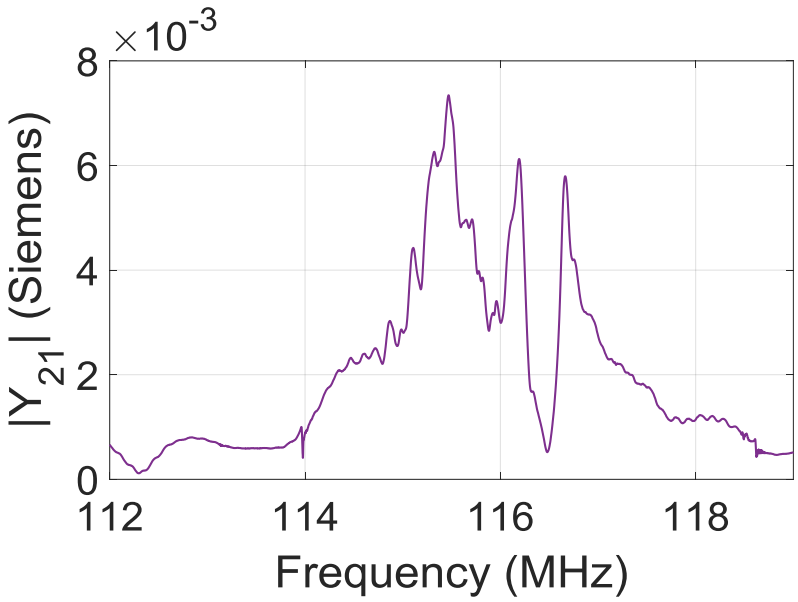

Figure 5.5 Frequency response for the drive and sense cavities showing a mismatch of 40 kHz.

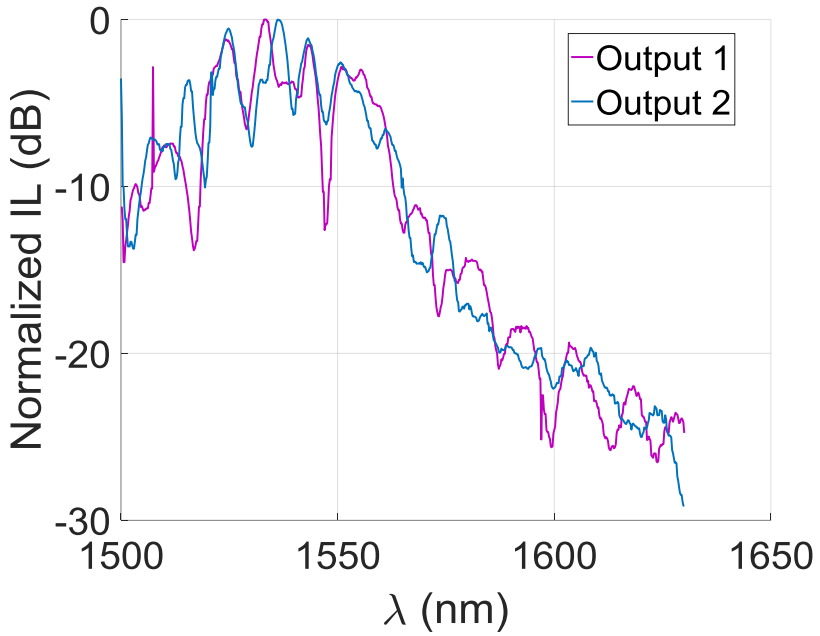

Figure 5.6 Measured insertion loss for the two output ports of the MZI as function of the wavelength.

The AOM measurement setup is shown in Figure 5.7. An Ultra-High Frequency Lock-In (UHFLI) amplifier from Zurich Instruments (ZI-BOX) is used to phase lock the SAW resonator using a built-in PLL. In addition, a built-in PID controller is used to amplitude-control the input signal for the SAW resonator and reject any variations due to vibration or temperature drift. A tunable laser generated carrier is coupled into the optical grating via a vertical groove array (VGA), which also couples out the

which also couples out the modulated AOM signal. The photonic output is fed to the lock-in amplifier, which is used to extract

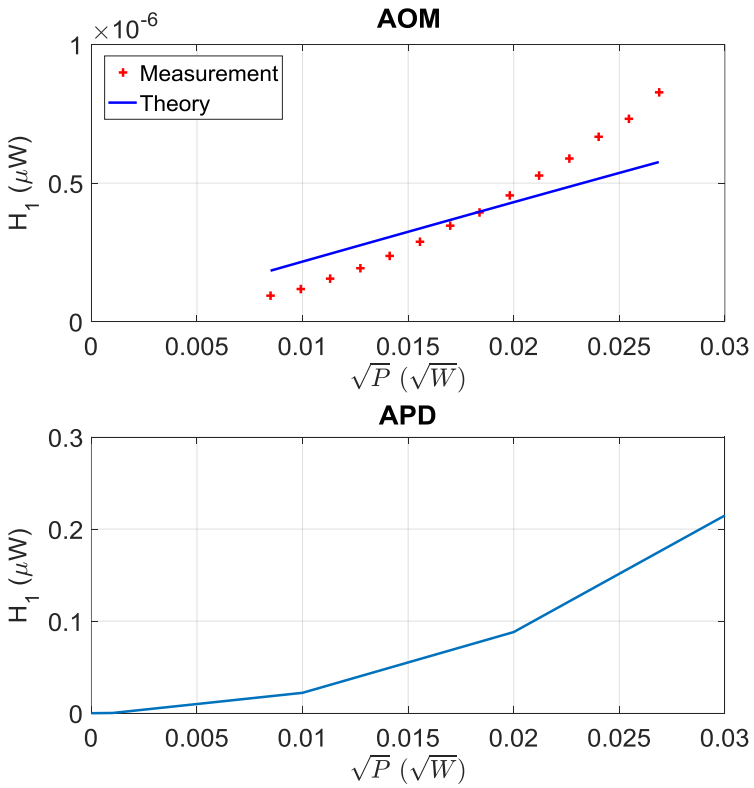

the first modulation harmonic.

Figure 5.8 top portion plots the measured modulation harmonic and compares the results with theoretical expectations. The measured power level for H_1 agrees with the theoretical expectations when we consider the coupling loss and the gain provided by the APD. The slight discrepancy between the theory and the measurements is attributed to the non-linearity in the response of the APD which is plotted in the bottom portion of the figure. Additionally, it is attributed to the fact that the model assumes only one dominant strain component while in reality we have more. That assumption was crucial in order to reach a closed form expression for the modulator. Rigorous modeling by considering the SAW resonator with the total number of reflectors is possible but requires very long simulation time and huge memory requirements. Nonetheless, the results prove that efficient AO modulation enhanced by the SAW cavity resonance as expected from theory.

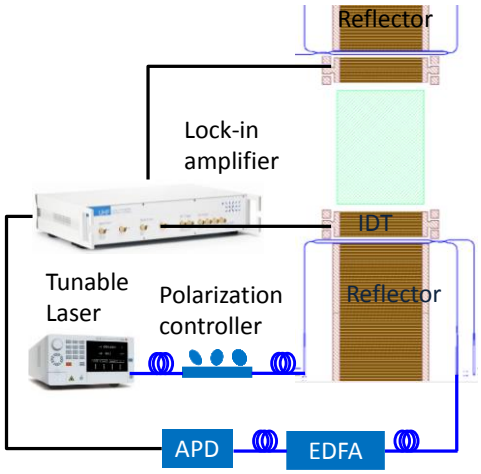

Figure 5.7 AOM measurement setup using lock-in amplifier.

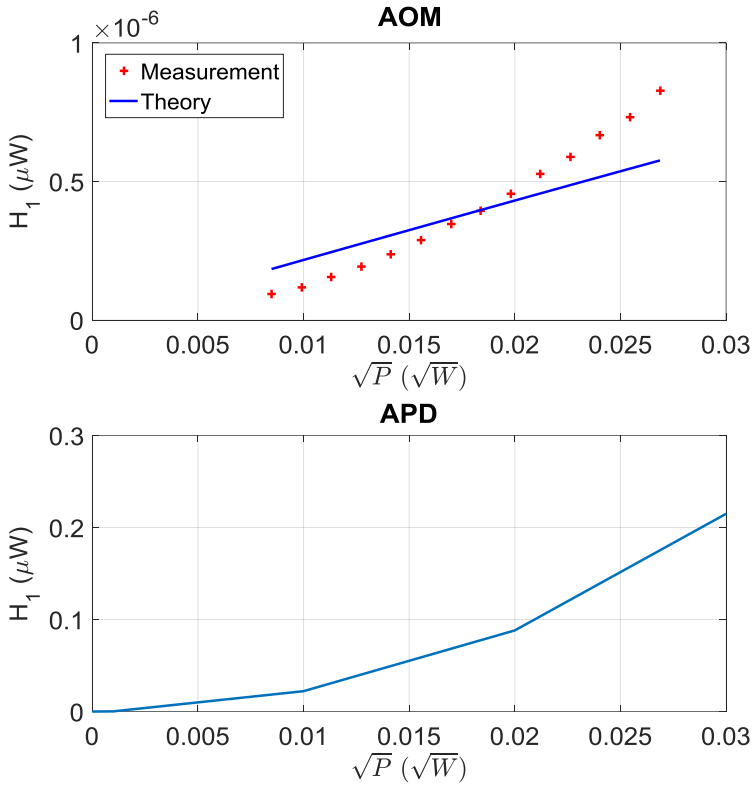

Figure 5.8 (Top) First modulation harmonic compared with theoretical expectations. (Bottom) Measured response for the APD alone.

5.2. EO tuned RT AOM

In this AOM, we use a high Q photonic racetrack (RT) resonator to enhance the AO interaction. However, efficient modulation can be obtained only when the coupling condition to the RT is near critical coupling [72]. The use of a directional coupler (DC) with narrow dimensions for achieving such critical coupling is a major fabrication challenge in LN as sub-100 nm gaps have to be defined. An alternative solution using a multi-mode interference (MMI) coupler is presented in this work. In addition, the coupling condition can be tuned by taking advantage of the unique EO properties of LN [68], hence ensuring attaining critical coupling condition at the desired wavelength of operation.

i. Theory and Design

A layout view for the proposed AOM is shown in Figure 5.9 **Error! Reference source not found.**, where a SAW IDT is placed near a photonic RT. The wave generated by the SAW IDT is used to modulate the light travelling through the photonic RT. The lower straight arm of the RT is split into two arms using two MMI couplers forming a Mach-Zehnder (MZI)-like structure. The EO coupling control electrodes are laid out parallel to the lower arm such that the electric field is directed along the material Z direction for maximum EO coefficient (r_{33} = 30 pm/V). Thus, the RT coupling coefficient will depend on the phase difference between the two arms induced by the applied voltage, V_c. Since applying voltage over the EO coupling control will also change the operating wavelength, additional electrodes for wavelength tuning are placed around the RT to ensure operation at the desired wavelength. The light is coupled in and out of the chip using grating couplers. Two S bends are introduced in the lower arm of the MZI to allow for the placement of the EO coupling electrodes.

In the following subsections we will describe: a) the principle of operation of the AO and the IDT design; b) the photonic RT design and the EO MZI-based coupling control method; c) the EO-based tuning of the system wavelength.

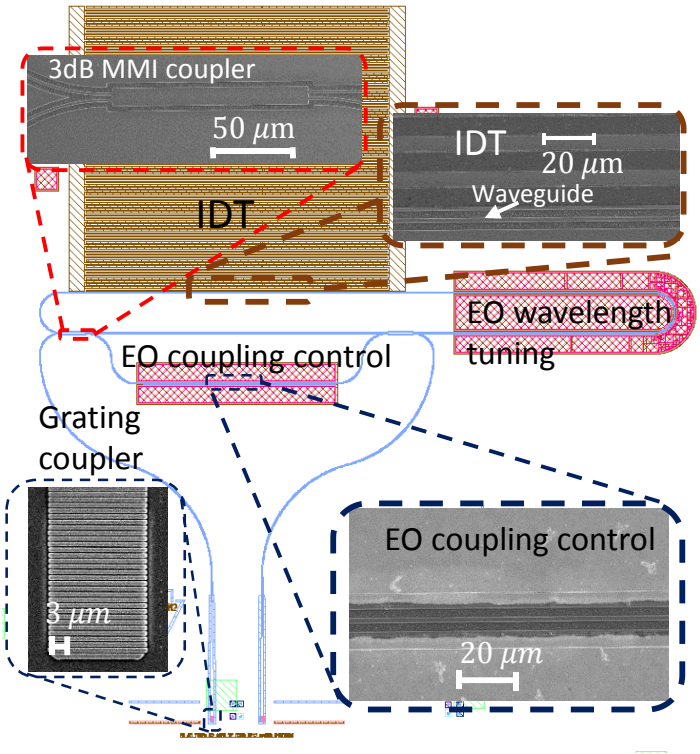

Figure 5.9 Layout view for the proposed AO RT modulator with zoomed-in SEMs of the various building blocks.

Consider a photonic waveguide having dimensions d for width, and e for its etch depth placed near an interdigitated transducer (IDT) with aperture L on top of an LNOI substrate (see Figure 5.10).

When a sinusoidal electrical signal of power p_e is applied to the IDT, a propagating SAW wave is generated, which induces a phase shift of the optical field in the waveguide according to the equation:

$$\varphi_{AO} = a_p \sqrt{p_e} \tag{5.16}$$

where $a_p = \Delta n 2\pi L / \lambda$ is the phase shift per square root of power, λ is the optical wavelength and Δn is the change in the refractive index, which is given by the equation:

$$\Delta n = -\frac{1}{2}\sqrt{M_2}\sqrt{\frac{2\eta}{HL}}\Gamma_{AO}\sqrt{p_e} \tag{5.17}$$

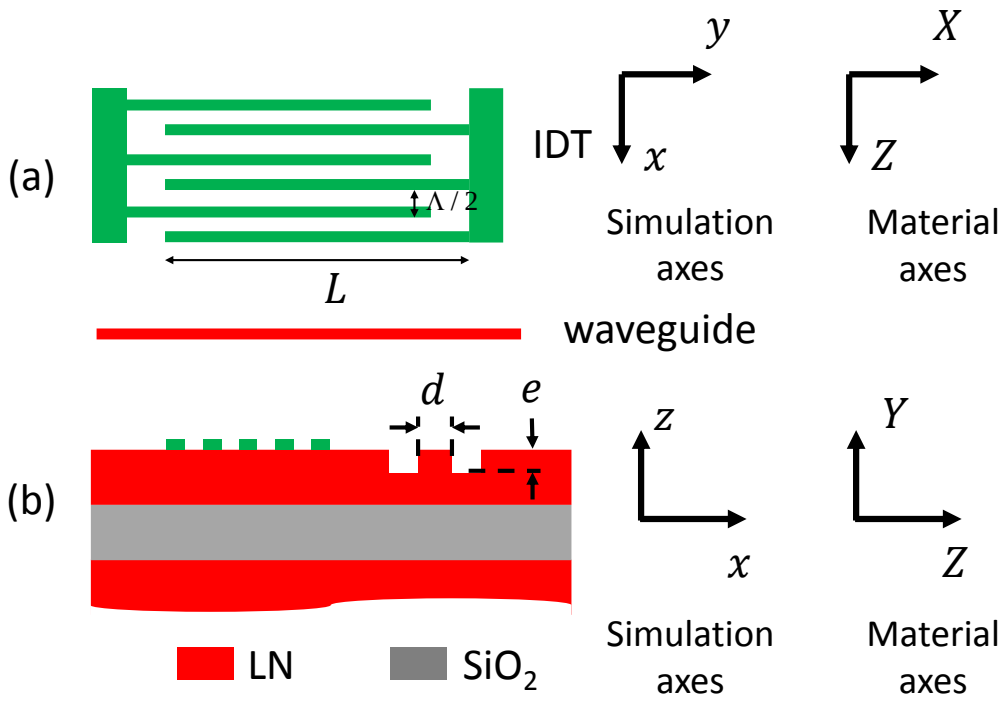

Figure 5.10 Waveguide placed near the IDT. The Capital letters (X, Y, and Z) denote the material axes while the small letters (x, y and z) denote the simulation axes. (a) Top view. (b) Side view.

where M_2 is the AO figure of merit (FOM) of LN expressed in terms of the refractive index, *n*, the effective photo-elastic coefficient , p^{eff} , in a specific SAW propagation direction, the material density, ρ , and the Rayleigh SAW wave velocity , v_R , as $M_2 = \left(n^6 \left(p^{eff} \right)^2 \right) / \left(\rho v_R^3 \right)$. M_2 can be estimated for our LNOI Y cut wafer to be equal to 0.5×10^{-14} sec^3 / kg in the case of a SAW wave propagating in the material Z direction. η is the electromechanical coupling efficiency and is limited to 50% for bidirectional IDTs designed with perfect matching to the source impedance, L is the aperture length and Γ_{AO} is the AO overlap factor already estimated in the previous section.

To obtain a compact IDT design with reasonable transduction efficiency, the aperture length and the number of IDT fingers were chosen as $L = 1500 \mu m$ and $N_{IDT} = 95$ such that the equivalent impedance is 200Ω. This means $\eta = 0.33$ when a 50Ω source impedance is used. The IDT periodicity is set to $\Lambda / 2 = 15 \mu m$, which will excite the SAW wave at the frequency, $f_m = 114 MHz$. Thus, Equations (5.16) and (6.20) can be used to estimate a_p to be equal to

$3 rad/\sqrt{W}$. Since this is the phase shift induced in the strained waveguide before inserting it in a RT, it is appropriate to compare it with phase shift induced by a push pull MZI previously reported in GaAs/AlGaAs substrate ($a_p = 2 rad/\sqrt{W}$) [62]. Despite the lower (15x) AO FOM in the case of LN [64], the a_p is higher and the improvement is mostly attributed to the higher transduction efficiency and the higher k_t^2 (~17x) of LN over GaAs/AlGaAs.

High Finesse ring or RT resonators can be used to more efficiently enable light modulation [73]. The efficiency of the modulation improves as the RT is operated near the critical coupling condition. Figure 5.11-a shows a ring resonator that is coupled to a bus waveguide using an EO-controlled DC to ensure critical coupling condition required for efficient modulation. As a control voltage, V_c, is applied to the electrodes placed around the coupling region, the EO properties of LN modulate the value of the coupling factor, r. For this configuration, the transfer function between the output and input fields can be expressed in terms of the DC coupling factor, r, the round trip phase shift, φ, and the field round trip loss, $a = e^{-\alpha L}$, as:

$$E_{out} = \frac{r(V_c) - ae^{-j\varphi}}{1 - ar(V_c)e^{-j\varphi}} E_{in} \tag{5.18}$$

where α is the propagation loss in dB/cm and r is written as $r(V_c)$ to point out that the coupling factor is function of V_c. However, etching narrow gaps in LN is challenging. Herein, we replace the narrow gap DC with the MZI based coupler, as shown in Figure 5.11-b. In this configuration, the coupling condition relies on the interference between the fields in the two arms of the MZI, which is modified by the voltage applied on the lower arm of the MZI. Thus, the optical field coupling coefficient can be expressed in terms of the EO phase shift, φ_{EO}, and the difference in the MZI arms' length, Δl, as:

$$r_{eq} = \frac{1}{2} e^{-jn\frac{2\pi}{\lambda}l_1} e^{-\alpha l_1} \left(1 - e^{-j\varphi_{EO}} e^{-jn\frac{2\pi}{\lambda}\Delta l}\right) \tag{5.19}$$

such that φ_{EO} can be expressed in terms of the refractive index, n, the MZI length, l_1, and the electrodes spacing, Δ, as:

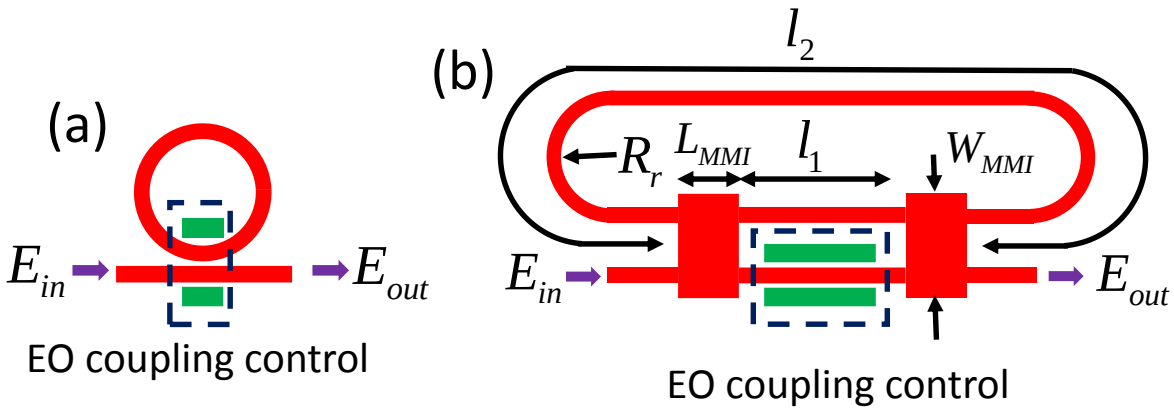

Figure 5.11 EO tuning of the coupling condition. (a) Ring resonator with gap based DC. (b) Proposed RT resonator with MZI based coupler consisting of two MMI couplers and two parallel waveguides.

$$\varphi_{EO} = \frac{r_{33} n^3 \pi l_1}{\lambda \Delta} \Gamma_{EO} V_c \tag{5.20}$$

Where Γ_{EO} is the electro-optical overlap between the optical field and the applied electric field as defined in section 4.1. Accordingly, the new transfer function can now be written similarly to eq (5.18) as:

$$E_{out} = \frac{r_{eq}(V_c) - a_{eq} e^{-j\varphi_2}}{1 - a_{eq} r_{eq}(V_c) e^{-j\varphi_2}} E_{in} \tag{5.21}$$

where r_{eq} is given by Eq (5.19), $a_{eq} = e^{-\alpha l_2}$ such that l_2 is the length of the RT that is not part of the MZI and φ_2 is given by:

$$\varphi_2 = n \frac{2\pi}{\lambda} l_2 \tag{5.22}$$

It is important to note that the effect of the AO modulation in this configuration can be readily modelled by including its contribution, φ_{AO}, in Eq. (6.20):

$$\varphi_2 = n \frac{2\pi}{\lambda} l_2 + \varphi_{AO} \tag{5.23}$$

The MMI couplers were designed as 3-dB splitters with the dimensions, $L_{MMI} = 276.4 \mu m$, and width, $W_{MMI} = 17.5 \mu m$. The RT radius was chosen to be large enough to ensure low losses ($R_r = 100 \mu m$). The light is coupled in and out of the chip using gratings couplers with their design discussed in section 3.1.

In section 4.1, we derived the EO tuning rate, *TR*, for a RT on LNOI to be given by:

$$TR \approx r_{33} n_{eff}^2 \frac{\lambda_{ro}}{2\Delta} \frac{l_t}{(l_1 + l_2)} \Gamma_{EO} \tag{5.24}$$

where l_t is the total length of the wavelength tuning electrodes.

Equations (5.16) to (6.20) are used to describe the operation of the overall system shown in Figure 5.9. The model is implemented in Matlab and used to estimate the coupling control as well as tuning rate and the AO modulation as a function of the various applied control or modulation voltages. A Fast Fourier Transform is used to calculate the modulation harmonics. The expected results are discussed in the next section, where they are directly compared with measurement results.

ii. Measurement Results

To verify the EO control over the coupling condition, the transmission response through the photonic RT was measured as a function of various values of the control voltage, Vc, applied across the electrodes placed around the bottom arm of the MZI. The experimental data together with their fitting are shown in Figure 5.12. The normalized |req| extracted from the fitting is plotted in Figure 5.13 and compared with theoretical expectations. There is a shift between the theoretical and the experimental curves, which is attributed to the asymmetry between the two MZI arms due to the fabrication process. However, the experimental results confirm the EO control capability over the coupling condition. The wavelength tuning capability through the EO effect is demonstrated in Figure 5.14 where the resonance wavelength, λ_r , is plotted as function of the voltage, V_T, applied across the electrodes place around the photonic RT. A TR of 0.38 pm/V can be extracted as the slope of the straight line fitting to the experimental response. The extracted value is slightly lower than what is expected theoretically (0.45 pm/V). Such difference might be attributed to the fact that the Al electrodes were slightly attacked during the last fabrication step (wet etch of the SiO_2) leading to larger electrodes. Nevertheless, this TR is consistent with what we have previously discussed in section 4.1 for an EO modulator with similar dimensions ratio.

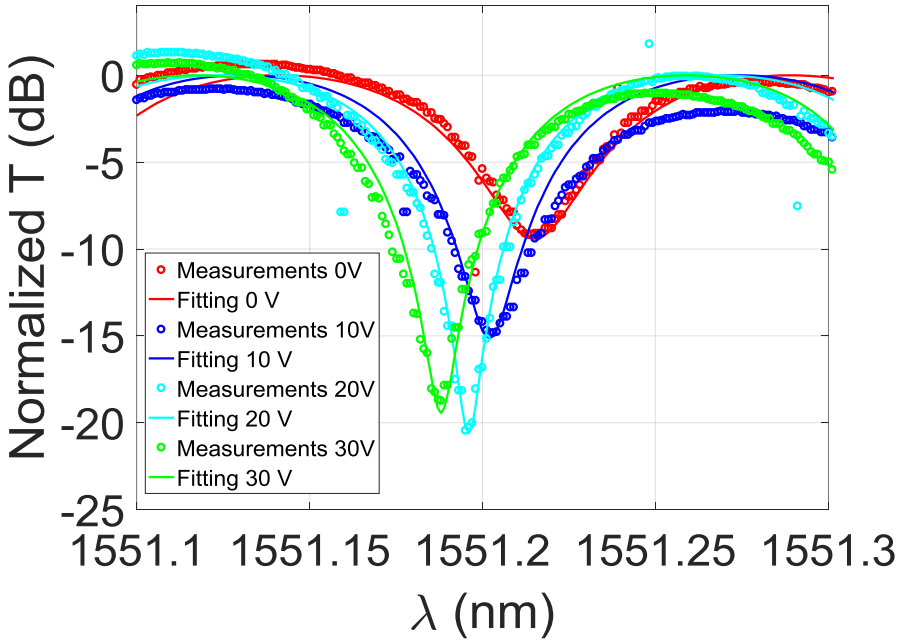

Figure 5.12 Transfer function of the RT as function of the wavelength for differennt values of the control voltage, V_c , applied across the EO-coupler tuning element.

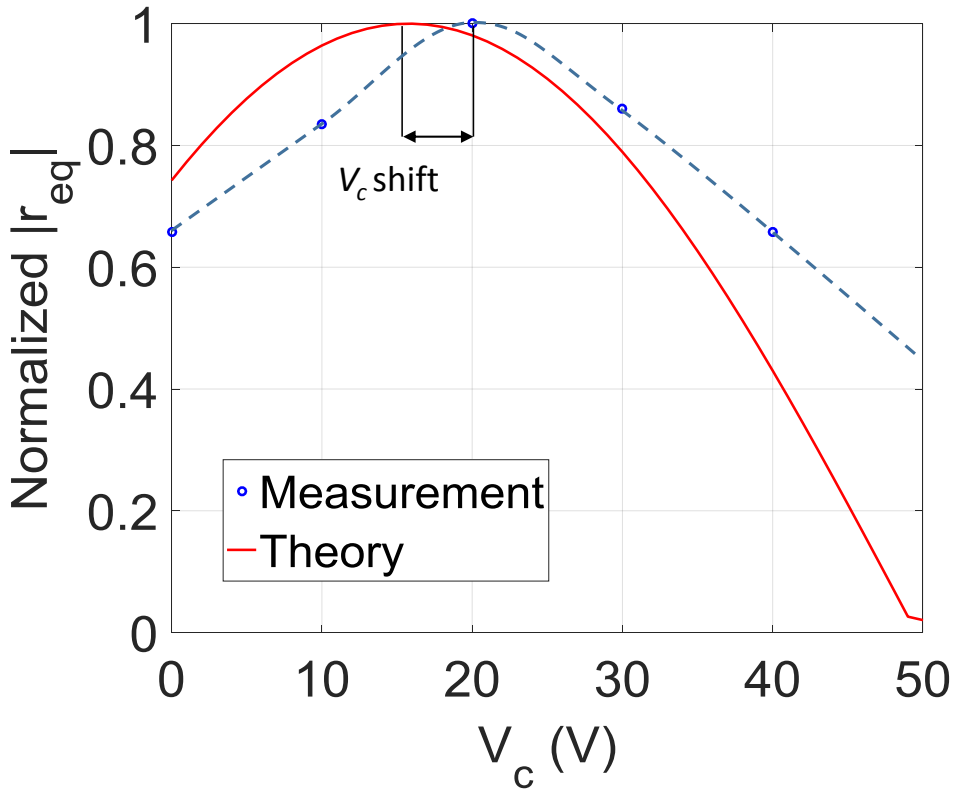

Figure 5.13 Extracted $|r_{eq}|$ from measurement as function of V_c compared with theory.

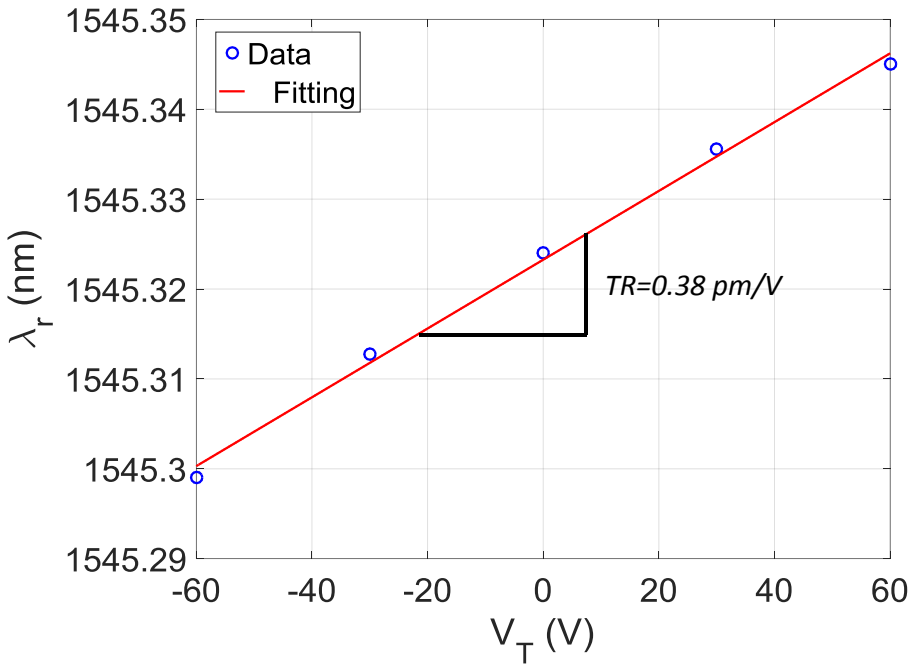

Figure 5.14 RT resonance wavelength as function of the applied voltage V_T.

The AO modulation measurement setup is shown in Figure 5.15. A SANTEC tunable laser is used as light source and coupled to a PM fiber in and out of the chip. The output signal from the fiber is connected to an Erbium Doped Fiber Amplifier (EDFA) and then demodulated by a 1544 New Focus avalanche photodetector (APD). The demodulated signal is collected through a

Spectrum Analyzer where the first and second harmonics of the modulated signal are monitored.

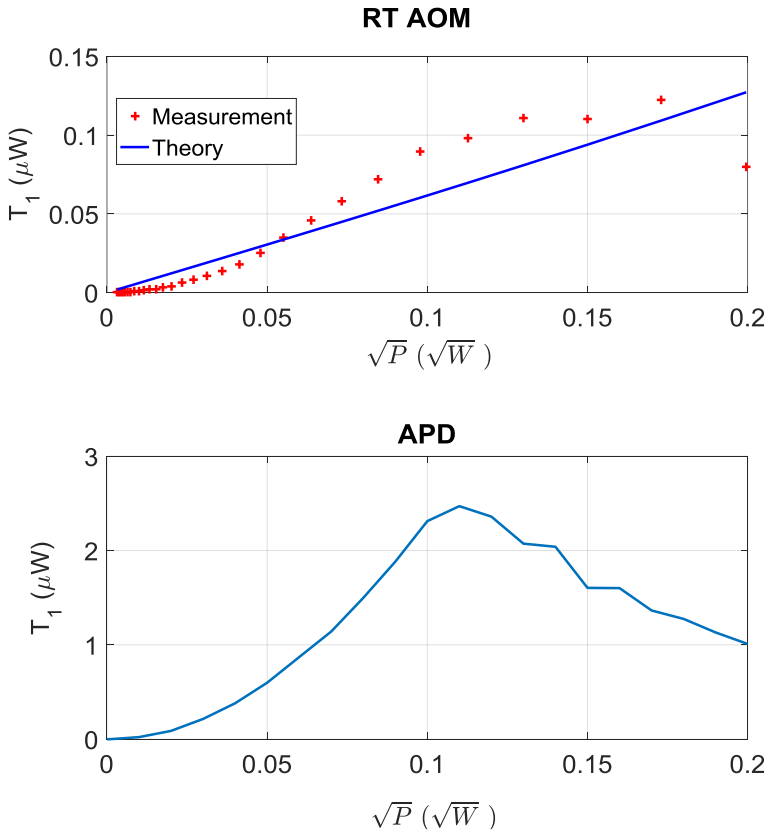

Figure 5.16 compares the measured modulation response with theory in the top sub-figure. The discrepancy between the theory and the measurements is attributed mostly to the non-linearity of the APD which is characterized separately in the bottom portion of the figure. Additionally, it might be attributed to the non-linearity in the transduction efficiency of the IDT at the low modulating power levels. Nonetheless, the results confirm that the value for the AO M_2 coefficient of the LN thin film is close to the expected theoretical value.

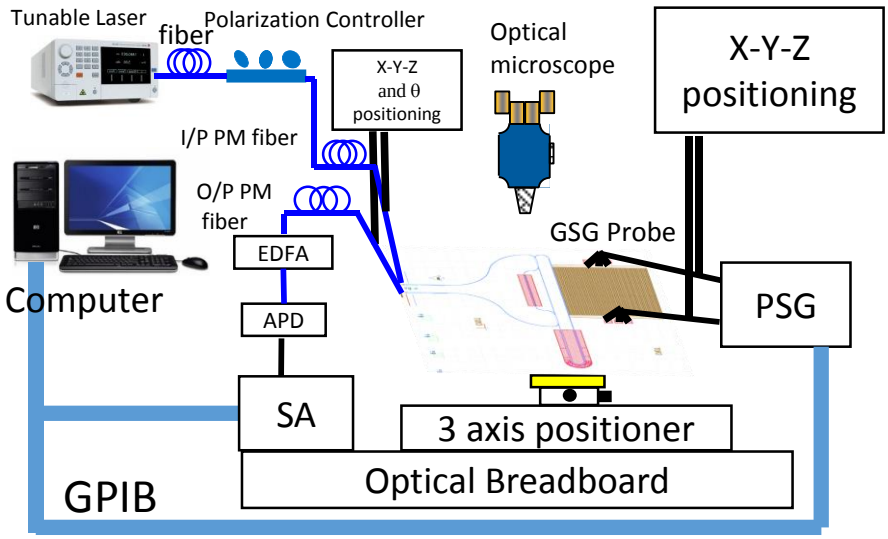

Figure 5.15 Measurements setup for AO modulation. SA=Spectrum Analyzer, PSG = Performance Signal Generator, APD = Avalanche photo-detector, EDFA=Erbium Doped Fiber Amplifier.

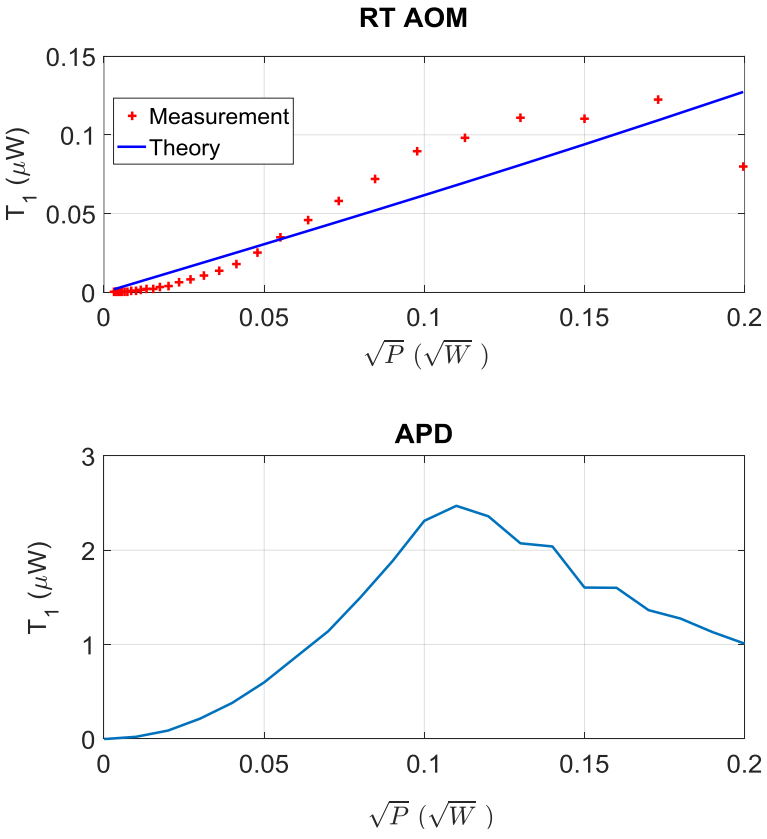

Figure 5.16 (Top) Measured response of the first harmonic of the AOM and comparison with theory. (Bottom) Measured response for the APD alone.

6. Acousto-optic Gyroscope

Existing gyroscopes for inertial navigation systems are based on either bulky mechanical implementations [74], [75] or large volume Optical Gyroscopes (OGs) [76]–[78]. MEMS vibratory gyroscopes (MVGs) [79]–[82] are an interesting alternative, but have exhibited limitations on various fronts. The need for a large released mass makes the MVG vulnerable to shock [83]. Since most MVGs operate at few kHz with quality factors > 1000, their output bandwidth is limited to mHz for frequency matched operation [84] unless complex bandwidth extension techniques are used [85]. Furthermore, the low operation frequency makes the gyroscope susceptible to environmental vibrations [86]. On the other hand, OGs such as Fiber Optic Gyroscope (FOG) and Ring Laser Gyroscope (RLG) can achieve both high performance and operation stability [76]. Unfortunately, miniaturization and power scaling of these implementations are challenging. In this work, we demonstrate the first prototype of an Acousto-Optic Gyroscope (AOG), which has the theoretical capability of addressing all the major issues encountered in MVGs or miniaturized OGs. The AOG is based on the concept of the Surface Acoustic Wave Gyroscope (SAWG) [87]–[89], in which the Coriolis force detection is performed optically instead of acousto-electrically. The use of SAW resonators enables the realization of a large unreleased mass. The optical sensing provides for extremely low noise levels and stable readout. In addition, the optical modulation method significantly simplifies the electronic readout. Different photonic phase sensing techniques can be used to detect rotation such as a Mach-Zehnder interferometer (MZI) [90] operated in the push pull operation, racetrack (RT) resonator, or an RT coupled to an MZI (MZI/RT) [91]. Here the Scale Factor, SF , for the AOG is analytically derived and compared for these various sensing techniques. The theoretical analysis is verified through experimental measurements of the SF for the MZI based AOG as well as the RT AOG. The angular random walk (ARW) is measured for the MZI-AOG and compared with the SAWG fabricated on the same platform to highlight the additional advantages of the photonic readout in regards to noise and stability.

6.1. Principle of Operation

Figure 6.1 depicts a schematic view of the AOG and offers an overview of its principle of operation. Two orthogonal SAW resonators are shown with metallic pillars placed at the center acting as the moving mass, M_p, of the gyroscope. A SAW standing wave pattern is established along the x (drive) direction. The pillars are placed inside the cavity at the anti-nodes of the SAW standing wave pattern (location of maximum x-directed velocity). The pillars are driven longitudinally with vibration velocity, v_p. When out-plane rotation, Ω_z, is applied, Coriolis force, F_c, is induced on the vibrating pillars in the direction orthogonal to both the input rotation direction and the drive vibration direction and can be expressed as:

$$F_c = -2M_p\Omega_z \times v_p \tag{6.1}$$

The pillars are arranged in a checkerboard configuration such that constructive interference for a secondary SAW wave is established in the y (sense) direction. The strain value, S, associated with this wave can be expressed in terms of the Coriolis force, the substrate mass density ($\rho = 4700 kg/m^3$) for LN, the Rayleigh SAW phase velocity ($v_R = 3488 m/\sec$), the SAW penetration depth, H (which is less than 10% of the acoustic wavelength Λ), and the acousto-optical (AO) interaction length, L, as:

$$S = \frac{F_c}{\rho v_R^2 LH} \tag{6.2}$$

In SAW gyroscopes, piezoelectric transducers are commonly used to sense the secondary waves. In this work, the secondary wave is detected through the elasto-optic effect in the photonic waveguides etched in the Lithium Niobate (LN) thin film, *i.e.* by monitoring the refractive index change, Δn, due to the strain induced by the secondary wave. The index change is expressed as:

$$\Delta n = \frac{1}{2} n^3 p_{eff} S \tag{6.3}$$

where p_{eff} is the effective acousto-optic coefficient in the specific propagation direction of the SAW. The photonic sensing technique shown in Figure 6.1 uses a push-pull MZI (PP-MZI), which converts the phase modulation to intensity modulation at the photodetector output by mixing the

optical beams from the two MZI arms. However, other phase sensing techniques like RT AOG or MZI/RT AOG can also be used, as we will discuss in the following sections.

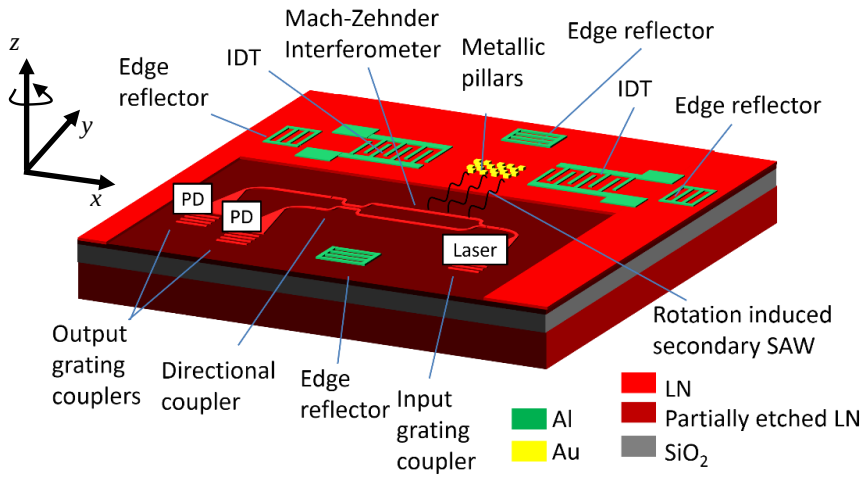

Figure 6.1 3D sketch for the AOG. PD=Photo-detector, IDT=Interdigitated transducer.

6.2. AOG Scale Factor and Comparison of Photonic Detection Techniques

The *SF* (or sensitivity) of the AOG is determined by the change in the optical signal intensity, *T*, due to the phase variation, $\varphi_{AOG,}$, $G = \partial T / \partial \varphi_{AOG}$, and the change in phase due to the external rotation, Ω_z, $\beta_{AOG} = \partial \varphi_{AOG} / \partial \Omega_z$ which directly relates to the SAW cavity design and the elasto-optic characteristics of the LN film. Overall, the SF can be expressed as:

$$SF = \frac{\partial T}{\partial \Omega_z} = \frac{\partial T}{\partial \varphi_{AOG}} \frac{\varphi_{AOG}}{\partial \Omega_z} = G\beta_{AOG} \tag{6.4}$$

The induced phase shift due to rotation, φ_{AOG} , can be expressed in terms of the refractive index change, Δn and the waveguide length, *L* as :

$$\varphi_{AOG} = \Delta n \frac{2\pi}{\lambda} L \tag{6.5}$$

where $\lambda = 1550\,nm$ is the optical wavelength. The *SF* is written in this way so that a direct comparison between various sensing techniques can be formulated by analyzing the gain factor, $G = \left| \frac{\partial T}{\partial \varphi_{AOG}} \right|_{\max}$.

i. Rotation induced phase changes

As discussed in section 5.1, placing the waveguides at the location of maximum strain for the standing wave pattern of the SAW cavity enhances the phase sensitivity by a factor that can be derived to be equal to $\sqrt{\frac{2\Lambda Q_S}{\pi L_c^{'}}}$ where Q_S is the resonator quality factor in the sense direction, Λ is the acoustic wavelength and $L_c^{'}$ is the total cavity length. This phenomenon can be accounted for by modifying Eq. (6.20) to be:

$$\varphi_{AOG} = \sqrt{\frac{2\Lambda Q_S}{\pi L_c^{'}}} \frac{2\pi}{\lambda} L\Delta n \tag{6.6}$$

The vibration velocity in Eq. (6.1) can be expressed in terms of the drive parameters: the electrical power, P_m, the drive resonator quality factor, Q_D, the resonator equivalent mass, M_r, and the SAW resonance frequency, f_m, as:

$$v_p = \sqrt{\frac{P_m Q_D}{\pi f_m M_r}} \tag{6.7}$$

Combining Eqs (6.1) to (6.20) the rotation induced phase can thus be derived to be equal to:

$$\beta_{AOG} = \frac{2\pi}{\lambda H} \sqrt{\frac{M_2}{\rho v_R}} M_p \sqrt{\frac{P_m Q_D}{\pi f_m M_r}} \sqrt{\frac{2\Lambda Q_S}{\pi L_c^{'}}} \tag{6.8}$$

where $M_2 = \left(n^6 \left(p_{eff} \right)^2 \right) / \left(\rho v_R^3 \right)$ is the AO figure of merit of the material

ii. Photonic sensing techniques

A. MZI

Figure 6.2 shows three phase sensing techniques considered for comparison in this study. Figure 6.2-a represents a PP-MZI which has a normalized transfer function given by

$T_{PP-MZI} = \sin 2\varphi_{AOG}$. The factor of two in the sin argument is due to the push-pull operation enabled by separating the MZI arms by a distance equal to $3\Lambda/2$. Thus, the AOG SF gain can be derived to be equal to $G_{PP-MZI} = 2$.

B. RT

The AOG RT phase sensing technique is shown in Figure 6.2-b where an RT is coupled to a bus waveguide. We assume that only the two straight arms of the RT contribute to the phase modulation. For this reason the separation between the two straight arms in the RT is set to even multiple of $\Lambda/2$, which enables doubling the phase sensitivity. Thus, the transfer function for the RT can be expressed in terms of the round trip intrinsic loss inside the RT, a^2, the coupling coefficient, r^2, and the round trip total phase shift, φ as:

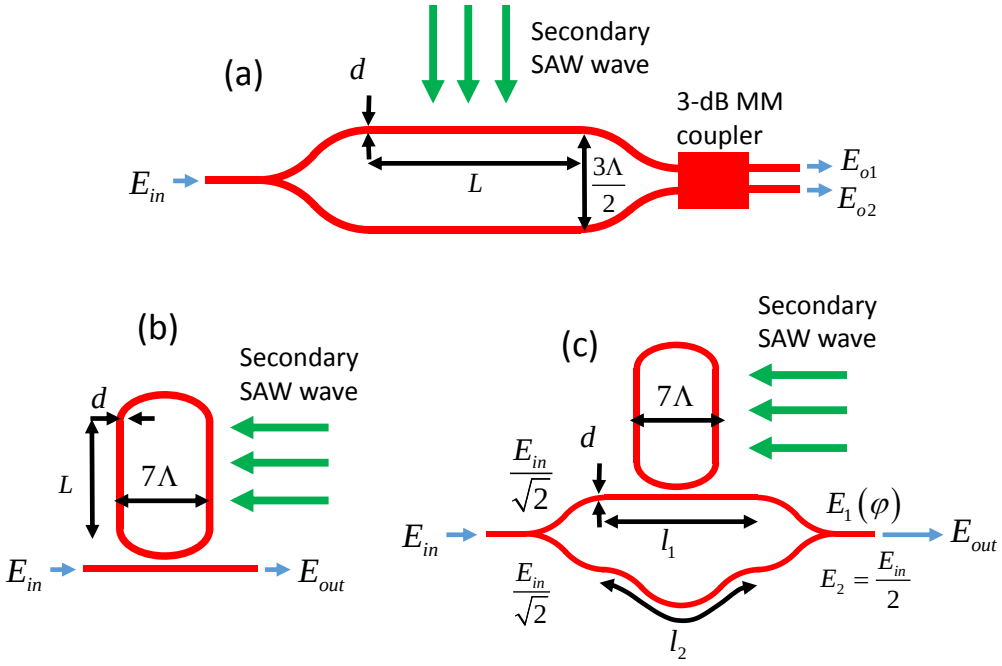

Figure 6.2 Phase sensing techniques for AOG. (a) PP-MZI. (b) RT. (c) MZI/RT

$$T_{RT} = \frac{a^2 + r^2 - 2ar\cos(\varphi)}{1 + a^2 r^2 - 2ar\cos(\varphi)} \tag{6.9}$$

The effective phase shift of the output field, E_{out}, with respect to the input one, E_{in}, is given by:

$$\varphi_{eff} = \tan^{-1}\frac{a\sin\varphi}{r - a\cos\varphi} - \tan^{-1}\frac{ar\sin\varphi}{1 - ar\cos\varphi} \tag{6.10}$$

Where $\varphi = \varphi_o + 2\varphi_{AOG}$, $\varphi_o = n\frac{2\pi}{\lambda}L_T$ is the round trip phase shift, and L_T is the total racetrack length. Thus:

$$\frac{\partial T_{RT}}{\partial \varphi} = \frac{2ar\sin\varphi\left(1+a^2r^2-r^2-a^2\right)}{\left(1+a^2r^2-2ar\cos\varphi\right)^2} \tag{6.11}$$

Figure 6.3 plots T_{RT} and its derivative as function of φ_{AOG} . The Finesse of the cavity is defined as the ratio between the free spectral range, 2π and the full width half maximum, $\Delta\varphi_{1/2}$ and its expression can be derived in terms of *a* and *r* as $F = \frac{\pi\sqrt{ar}}{1-ar}$. The plot in the figure assumes a specific value of the cavity Finesse, *13*. It is evident that the maximum value of the derivative of T_{RT} is a strong function of *a* and *r*. $\frac{\partial T_{RT}}{\partial \varphi}$ has a maximum at a specific phase offset that equals to one quarter of the full width half maximum, $\Delta\varphi_{max} = \Delta\varphi_{1/2} / 4$ where $\Delta\varphi_{1/2}$ is given in terms of *a* and *r* as $\Delta\varphi_{1/2} = \frac{1-ar}{\sqrt{ar}}$. Accordingly, the AOG gain can be derived as:

$$G_{RT} = \left|\frac{\partial T_{RT}}{\partial \varphi_{AOG}}\right|_{\varphi=\varphi_r+\Delta\varphi_{1/2}/4} \tag{6.12}$$

At this specific bias point, and assuming a low loss resonator, we can approximate $\sin\varphi \approx \Delta\varphi_{1/2}/4$ and $\cos\varphi \approx 1-\frac{1}{2}\left(\frac{\Delta\varphi_{1/2}}{4}\right)^2$ in Eq. **Error! Reference source not found.** to get:

$$G_{RT} \approx \frac{ar\Delta\varphi_{1/2}\left(1-a^2\right)\left(1-r^2\right)}{2\left(1+a^2r^2-2ar+ar\frac{\left(\Delta\varphi_{1/2}\right)^2}{16}\right)^2} \tag{6.13}$$

Also for low loss cavity near critical coupling, we can impose that $a \approx r$ and $F \approx \frac{\pi r}{1-r^2} = \frac{2\pi}{\Delta\varphi_{1/2}}$ so as to find a very simple expression of the RT gain factor:

$$G_{RT} = \frac{32F}{25\pi} \approx \frac{2F}{5} \tag{6.14}$$

To verify this analytical value, the derivative $\partial T_{RT} / \partial \varphi_{AOG}$ is computed numerically using Matlab and plotted in Figure 6.4 as a function of r for two values of $a = 0.85$ and $a = 0.99$. The

first value $a = 0.85$ represents the round trip loss extracted from the RT resonator of this work and is equivalent to a propagation loss of 2.45 dB/cm. The second value of a=0.99, corresponds to ultra-low losses (2.45 dB/m) that were recently reported for etched waveguide on the same LNOI substrate [93]. Note that the Finesse of the cavity is varying along that curve as r varies and the arrows point out the F value at the points of maximum slope.

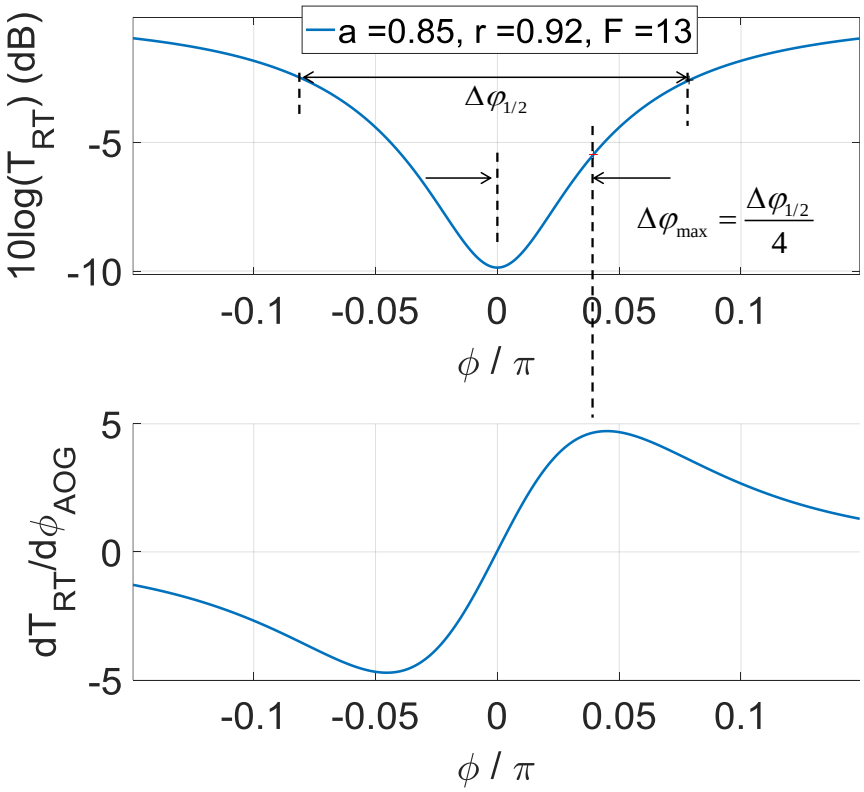

Figure 6.3 RT transfer function and its derivative as function of phase..

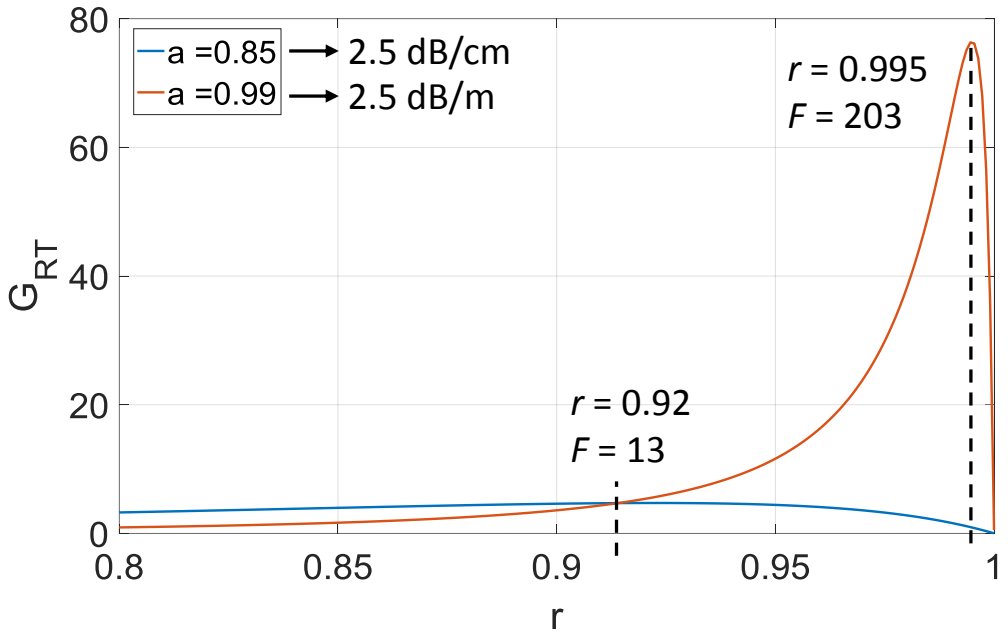

Figure 6.4 G_{RT} as function of r for two values of a

That numerical analysis confirms our analytical conclusion that the gain in the SF is bounded by $2F/5$. It also shows the RT has to be under-coupled for maximum phase sensitivity in agreement with [91].

C. MZI/RT

In this phase sensing technique, the RT is combined with the MZI. We can write the output optical field as sum of two fields (see Figure 6.2-c):

$$E_{out} = E_1(\varphi) + E_2 \tag{6.15}$$

Where $E_2 = E_{in}/2$ is the field from the reference arm while $E_1(\varphi)$ is the modulated AOG signal in the arm coupled to the RT. Thus, the output power can be written as:

$$P_o = |E_1(\varphi)|^2 + |E_2|^2 + 2|E_1(\varphi)||E_2|\cos(\varphi_1 + \varphi_{eff}(\varphi) - \varphi_2) \tag{6.16}$$

Where $\varphi_{eff}(\varphi)$ is the effective phase shift due to the RT and is given by Eq **Error! Reference source not found.**, $\varphi_1 = n\frac{2\pi}{\lambda}l_1$, $\varphi_2 = n\frac{2\pi}{\lambda}l_2$ are the phase shifts in the MZI upper and lower arms respectively. Accordingly, the transfer function for this phase sensing technique can be expressed as:

$$T_{MZI/RT} = \frac{T_{RT}}{4} + \frac{1}{4} + 2\frac{\sqrt{T_{RT}}}{2}\frac{1}{2}\cos\left(\varphi_{eff}\left(\varphi\right) - \varphi_{21}\right) \tag{6.17}$$

where $T_{RT} = \left|E_1\left(\varphi\right)\right|^2 / \left|E_{in}\right|^2$ is the RT transfer function given by Eq. **Error! Reference source not found.** and $\varphi_{21} = \varphi_2 - \varphi_1$. The derivative with respect to the phase of the transfer function is:

$$\frac{\partial T_{MZI/RT}}{\partial\varphi} = \frac{1}{4}\frac{\partial T_{RT}}{\partial\varphi} - \frac{\sqrt{T_{RT}}}{2}\frac{\partial\varphi_{eff}\left(\varphi\right)}{\partial\varphi}\sin\left(\varphi_{eff}\left(\varphi\right) - \varphi_{21}\right) + \frac{1}{2}\cos\left(\varphi_{eff}\left(\varphi\right) - \varphi_{21}\right)\frac{1}{2\sqrt{T_{RT}}}\frac{\partial T_{RT}}{\partial\varphi} \tag{6.18}$$

Maximum phase variation occurs at resonance, so the first and third terms are equal to zero because $\frac{\partial T_{RT}}{\partial\varphi} = 0$. Also, at resonance, $\varphi_{eff}\left(\varphi\right) = \varphi_{eff}\left(\varphi_r\right) = 2m\pi$. Thus, Eq. **Error! Reference source not found.** is reduced to:

$$\frac{\partial T_{MZI/RT}}{\partial\varphi} = -\frac{\sqrt{T_{RT}}}{2}\frac{\partial\varphi_{eff}\left(\varphi\right)}{\partial\varphi}\sin\left(-\varphi_{21}\right) \tag{6.19}$$

According to Eq **Error! Reference source not found.**, the gain factor is maximized when the phase difference, φ_{21}, is equal to $\pi/2$. This phase difference can be imposed by building an asymmetric MZI or using a directional coupler which provides a $\pi/2$ phase difference when operating as a beam combiner for a symmetric MZI. In this case, the gain factor associated with MZI/RT phase sensing technique can be expressed as:

$$G_{MZI/RT} = \sqrt{T_{RT}}\frac{\partial\varphi_{eff}\left(\varphi\right)}{\partial\varphi} = \frac{r-a}{1-ar}\frac{a\left(1-r^2\right)}{\left(r-a\right)\left(1-ar\right)} \approx \frac{r\left(1-r^2\right)}{1-r^2} \approx \frac{F}{\pi} \tag{6.20}$$

Eq. **Error! Reference source not found.** shows that, at critical coupling condition, the $\sqrt{T_{RT}}$ equals zero while the $\partial\varphi_{eff}\left(\varphi\right)/\partial\varphi$ is infinity but the product of the two is a finite value limited by the cavity finesse, F . Using a DC at the output of the symmetric MZI doubles the gain and yields $G_{MZI/RT/DC} \approx 2F/\pi$. The numerical analysis results are depicted in Figure 6.5-a and Figure 6.5-b and confirm the conclusions drawn from the analytical equations.

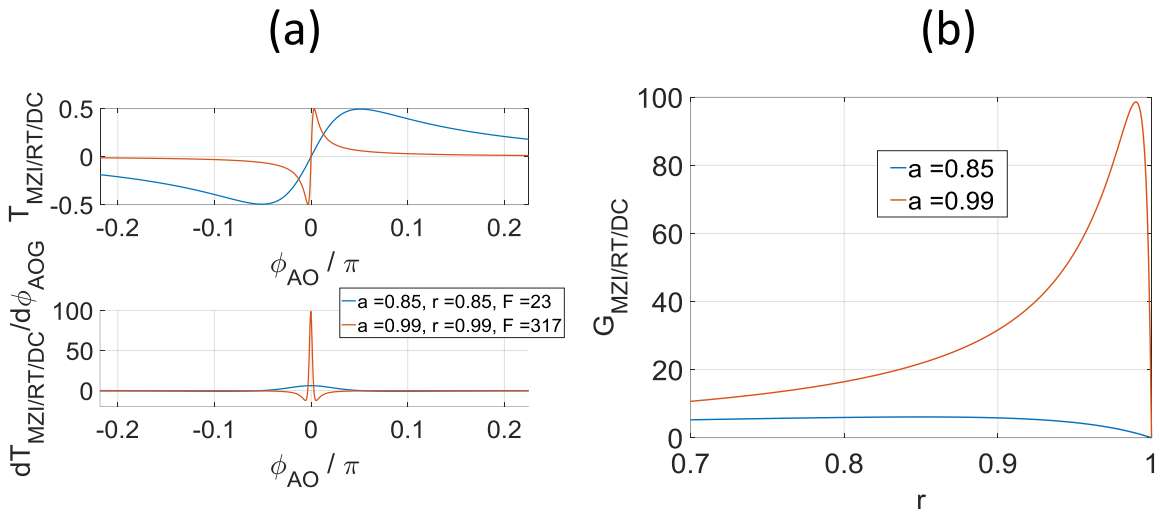

Figure 6.5 (a) MZI/RT/DC transfer function and its derivative as a function of phase. (b) $G_{MZI/RT/DC}$ as a function of r for different value of a.

Although the gain in the MZI/RT/DC is slightly better than the RT technique, asymmetry in the MZI arms due to fabrication tolerances may affect the overall sensitivity of this approach. To ensure symmetry, an electro-optic (EO) tuning on one of the arms [90] is needed to make sure $\varphi_{21} = \pi / 2$. To reduce the fabrication and measurement complexity, our first demonstration for the AOG is based on the techniques that do not require additional EO control which are the PP-MZI and the RT techniques as shown in the next section.

6.3. Acousto-optic Gyroscope Design

Figure 6.6 and Figure 6.7 show the layout views for the MZI-AOG and the RT-AOG respectively with zoomed-in SEMs of the various constitutive components. Four identical Interdigitated Transducers (IDT), SAW reflectors and photonic waveguides are placed symmetrically with respect to a central pillar-filled cavity so as to ensure frequency matching between orthogonal SAW resonators. The light is coupled in and out using grating couplers. The photonic readout shown in Figure 6.6 is based on a (PP-MZI) where a Y junction is used for splitting the optical input into the two arms of the MZI and a 2x2 multimode interference (MMI) 3-dB coupler is used as a beam combiner. The differential output is detected using a balanced photodetector. On the other hand, an RT is used in the photonic read-out in Figure 6.7 where a

butterfly MMI coupler [34] is used to couple the light to the RT. The following sub-sections will describe the design of each component forming the two AOGs.

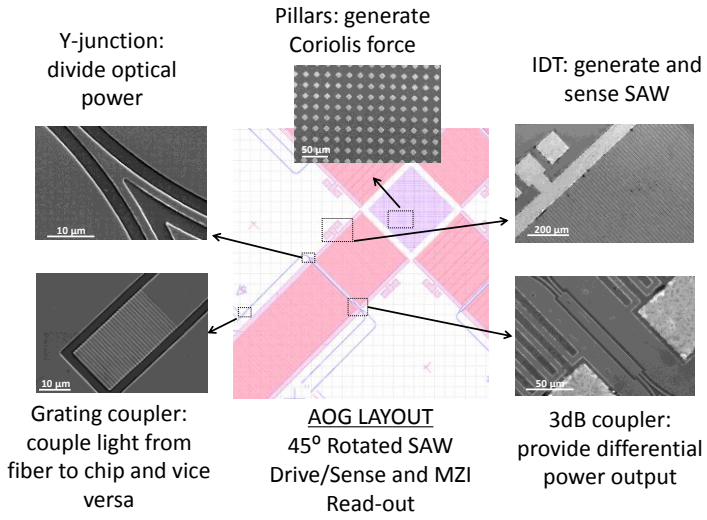

Figure 6.6 Layout view of the MZI AOG with zoomed-in SEMs of the various components forming it.

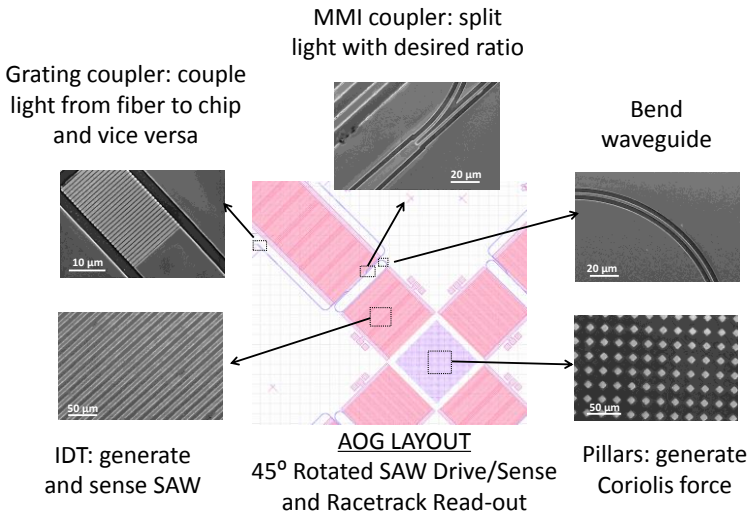

Figure 6.7 Layout view of the RT AOG with zoomed-in SEMs of the various components forming it.

i. SAW Resonator Design

The SAW resonator *Q* in the drive and sense directions can be fully harnessed in case the frequencies of the orthogonal resonators are matched. Previous SAW gyroscope designs [11], [87], [95] targeted SAW propagation direction and LN wafer cuts that provide the highest electromechanical coupling coefficient such as propagating the SAW in the Z direction for a Y cut

LN wafer. However, for such a cut, the material properties in the two orthogonal in-plane directions (X and Z) are not the same due the trigonal crystalline structure of LN. Such a configuration makes frequency matching difficult. In our AOG design, the two SAW resonators are rotated by $\pm 45^o$ with respect to the Z-direction to preserve symmetry, hence inherently matching the drive and sense frequencies. The aperture length is equal to the total cavity length and is chosen to be $L = 40\Lambda$. The acoustic wavelength is selected to be $\Lambda = 30\mu m$ so as to fit the gyroscope design in a 20x20 mm^2 die.

ii. Photonic components design

For both types of AOGs, the gratings couplers design is the same one discussed in section 3.1. The length of the waveguides of the MZI arms and the RT straight arm is chosen to be equal to the cavity length. The waveguides are placed at the positions of the maximum strain in the SAW cavity, $L = 40\Lambda$. The MZI arms' separation is set to $3\Lambda/2$ for push-pull operation while the RT straight arms' separation is set to 7Λ to double the phase sensitivity. The length and width of the 3-dB MMI coupler in the MZI-AOG are chosen to be $118.1\mu m$ and $11.6\mu m$, respectively, to ensure 3-dB splitting around 1550 nm (optical wavelength). The dimensions of the butterfly MMI coupler [34] in the RT-AOG were chosen to be equal to $7.6\mu m$ as the outer width, $14.5\mu m$ as inner width and $442.6\mu m$ as length.

6.4. Characterization

i. Characterization of SAW resonators

The frequency responses of the drive and sense acoustic resonators are measured using a vector network analyzer (PNA N5230A) and RF probing. The measurement result is shown in Figure 6.8. The ~40 kHz mismatch between sense and drive frequencies can be attributed to fabrication misalignments. This mismatch is still within the resonator bandwidth, which is approximately 100 kHz (loaded $Q_D = Q_S = 1000$).

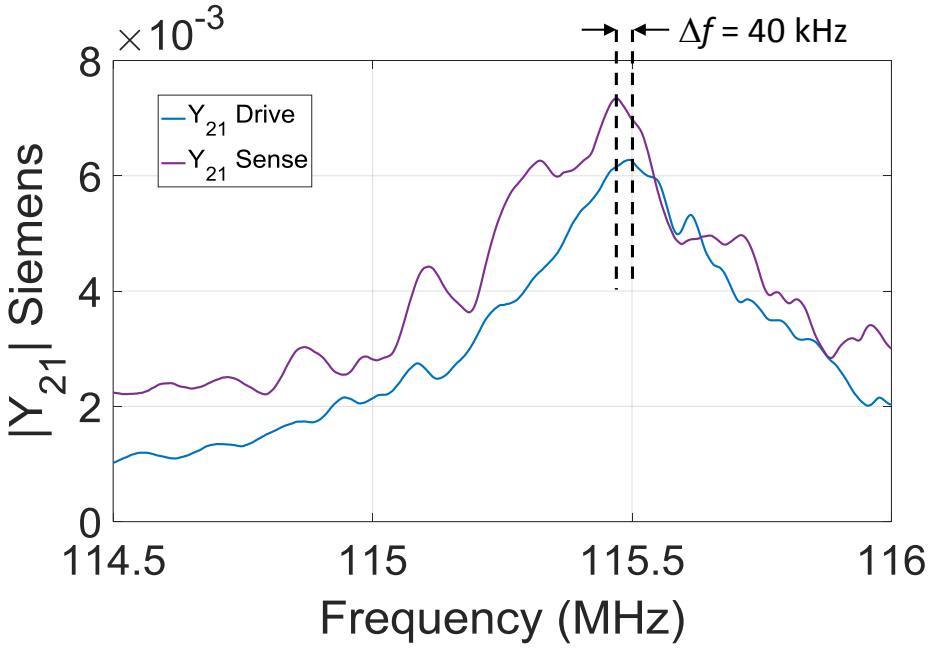

Figure 6.8 Frequency response for the drive and sense cavities showing a mismatch of 40 kHz.

ii. Characterization of the Photonic MZI and RT

Figure 6.9-a plots the MZI transfer function for the two outputs as a function of the wavelength. A balanced output is achieved at a few wavelengths near the design value of 1550 nm.

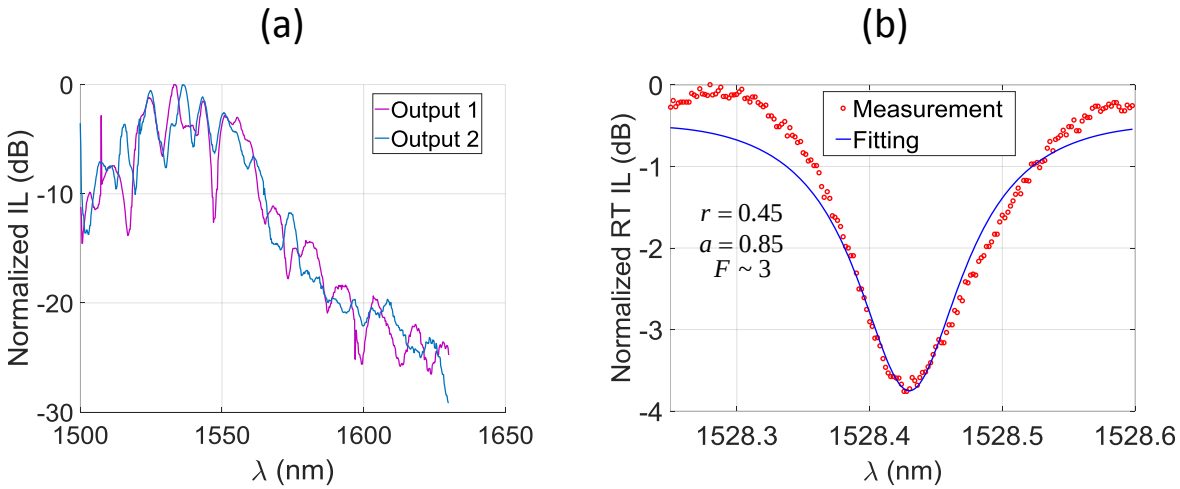

Figure 6.9 (a) Measured insertion loss for the two output ports of the MZI as function of the wavelength.(b) Measured insertion loss for the RT as function of wavelength together with fitting.

The slight shift in the wavelength might be attributed to differences in the actual dimensions of the etched waveguides with respect to the design values. The envelope reflects the transfer function of the grating couplers. On the other hand, the RT transfer function with respect to the wavelength is plotted in Figure 6.9-b together with the fitting to extract the round trip loss, *a*, and the coupling coefficient, *r*, as well as the Finesse, *F*. The fiber to chip coupling loss for the MZI was about -35 dB while that for the RT was about -36 dB. Such high coupling losses are substituted by the EDFA gain (~40 dB). Although the butterfly MMI coupler was designed to achieve slightly under-coupling condition, the extracted value for *r* is less leading to over-coupling ($r < a$) which does impact the measured *SF* negatively. Additionally, the extracted value for the intrinsic loss ($a = 0.85$) will have even more negative impact on the measured *SF* in the next sub-section. Figure 6.10 plots the numerically calculated RT transfer function its derivative for the actual coupling condition and the shows the bias point for maximum sensitivity.

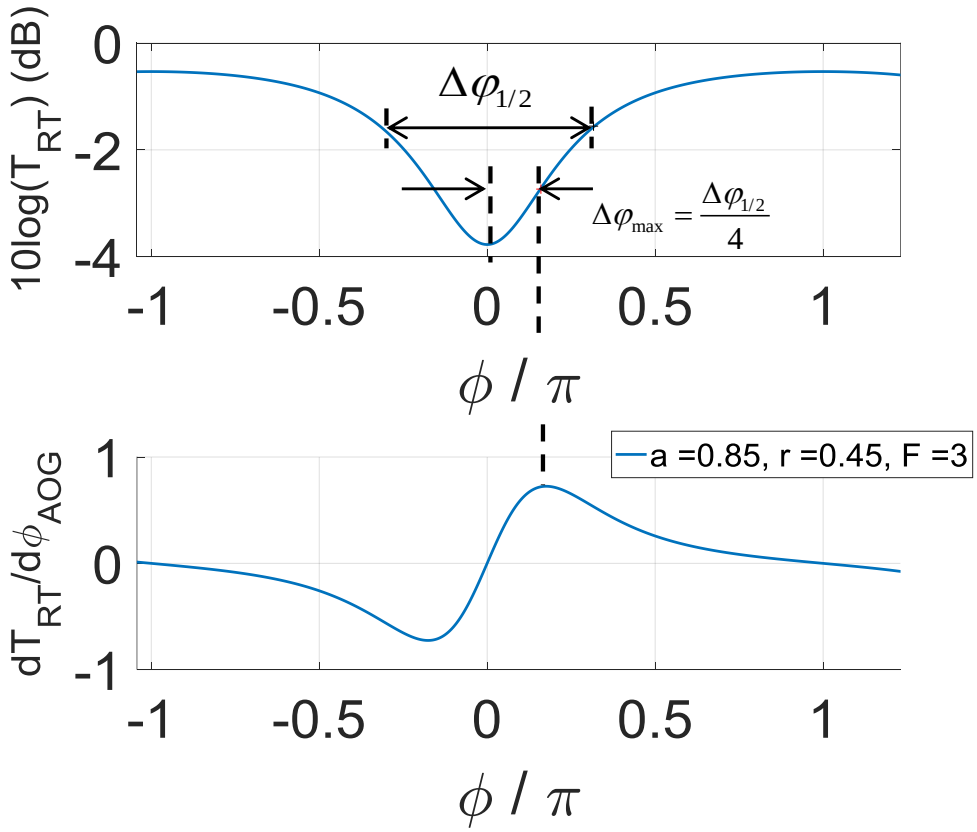

Figure 6.10 RT transfer function and its derivative as function of phase for the actual losses and coupling condition.

iii. AOG SF Measurement

The AOG measurement setup is shown in Figure 6.11 where each of the AOGs sample is mounted on the rate table together with the optical positioners and connected to the measurement instruments. The gyroscope die is packaged in a Pin Grid Array (PGA) ceramic package. An Ultra-High Frequency Lock-In (UHFLI) amplifier from Zurich Instruments is used to phase lock the SAW drive resonator using a built-in Phase Locked Loop (PLL). In addition, a built-in Proportional Integral Derivative (PID) controller is used to amplitude-control the drive signal for the SAW resonator and reject any variations due to vibration or temperature drift. An optical carrier generated by a benchtop tunable laser (SANTEC TSL-510) is coupled into the optical grating via a vertical groove array (VGA). Polarization controller is used after the Laser to make sure that we excited the TE polarization for which the gratings couplers were optimized. Erbium doped fiber amplifier (EDFA) is at the output to compensate for the coupling loss. The same VGA is also used to couple out the modulated gyroscope signal through another set of fibers in the array.

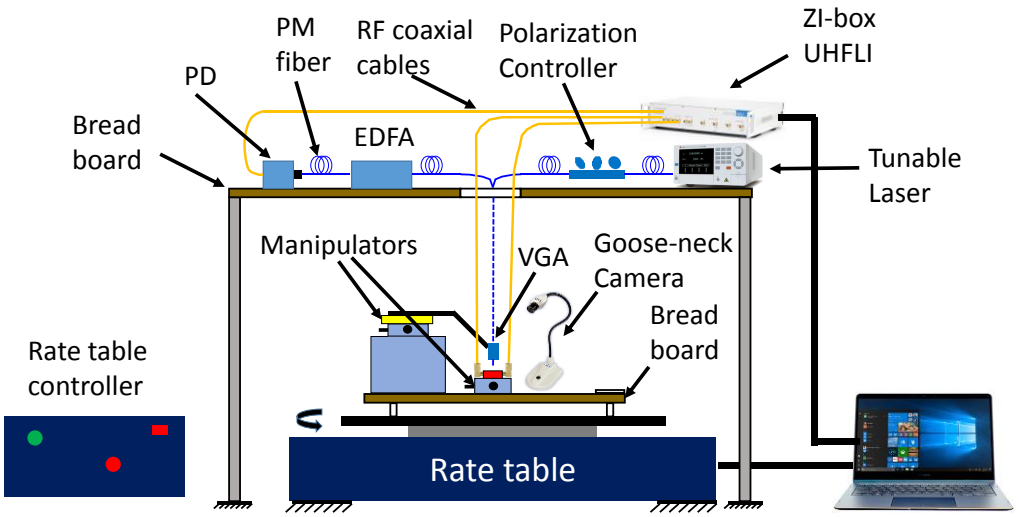

Figure 6.11 AOG measurement setup. The optical setup with the positioners and manipulators are mounted on top of the rate table.

The optical alignment is optimized by adjusting a six degree of freedom manipulator and sweeping the laser wavelength. The photonic output is fed to the lock-in amplifier where the Coriolis component is separated from the quadrature component. Due to the RF connecting cables and fibers, full 360^0 rotations for the rate table are not allowed. Instead, the input rotation is applied as a sinusoidal oscillation of fixed frequency (2 Hz) and variable amplitude.

The *SF* can be extracted for each AOG as the slope of the straight line in Figure 6.12-a. The measured $SF_{PP\text{-}MZI}=48\ nV/(^{o}/sec)$ in the case of the PP-MZI is higher than that of the RT $SF_{RT}=9\ nV/(^{o}/sec)$ with the ratio $SF_{PP-MZI}/SF_{RT}\approx 5.3$. The theoretically predicted ratio can be calculated as the ratio between the two gain factors (see Figure 6.12-b)

$$\frac{SF_{PP-MZI}}{SF_{RT}}=\frac{G_{PP-MZI}}{G_{RT}}=\frac{2}{0.7}=2.9 \tag{21}$$

The small discrepancy between the theoretical prediction and the measured value is attributed to the tolerance in the chip coupling loss between the two chips due to the optical fiber alignment (~3 dB). These experimental results showcase the first demonstration of an AOG and confirm the validity of our proposed analytical model of the device, especially in regards to the various photonic sensing techniques.

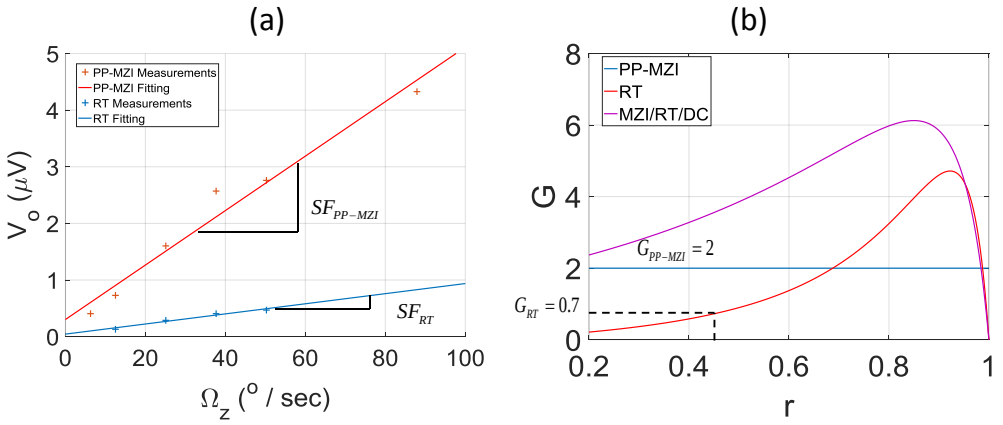

Figure 6.12(a) Measured output voltage as a function of rotation rate together with fitting to extract the scale factor for each AOG. (b) Theoretical comparison between various photonic sensing techniques.

As a conclusion, novel rotation sensing technique based on the acousto-optic effect is developed. Three different photonic phase sensing techniques are considered for comparison. Analytical and numerical analysis is considered studying each technique. The manufacturability of that novel device is ensured by developing a fabrication process that integrated acoustics and photonics on the same LNOI platform. The experimental results not only presents the first demonstration for the AOG but also verifies our theoretical study and shows that recently demonstrated low losses waveguides in that platform will open the door to highly sensitive, really stable strain based MEMS gyroscopes.

References

[1] Y. Zhang, J. Ai, Y. Xiang, Q. He, and T. Li, "A High Performance Optomechanical Mass Sensor," in *Conference on Lasers and Electro-Optics (2017), paper JW2A.14*, 2017, p. JW2A.14.

[2] Q. Liu, M. Li, and H. Li, "On-chip Eletromechanically Induced Brillouin Scattering on Suspended Aluminum Nitride Waveguides," in *Conference on Lasers and Electro-Optics (2017), paper JTh2A.115*, 2017, p. JTh2A.115.

[3] J. Horner, *Optical Signal Processing*. Elsevier, 2012.

[4] S. Ghosh and G. Piazza, "Piezoelectric actuation of aluminum nitride contour mode optomechanical resonators," *Opt. Express*, vol. 23, no. 12, pp. 15477–15490, Jun. 2015.

[5] G. Ryu, Y. Lee, and K. Lee, "Development of acoustic-optic (AO) SLM applicable to 3D holographic dispay," in *2017 19th International Conference on Solid-State Sensors, Actuators and Microsystems (TRANSDUCERS)*, 2017, pp. 1979–1982.

[6] R. Wang, S. K. Durgam, Z. Hao, and L. L. Vahala, "An SOI-based tuning-fork gyroscope with high quality factors," 2009, vol. 7292, pp. 729238-729238–9.

[7] C. Acar, A. R. Schofield, A. A. Trusov, L. E. Costlow, and A. M. Shkel, "Environmentally Robust MEMS Vibratory Gyroscopes for Automotive Applications," *IEEE Sens. J.*, vol. 9, no. 12, pp. 1895–1906, Dec. 2009.

[8] K. Liu, W. Zhang, W. Chen, K. Li, F. Dai, F. Cui, X. Wu, G. Ma, and Q. Xiao, "The development of micro-gyroscope technology," *J. Micromechanics Microengineering*, vol. 19, no. 11, p. 113001, 2009.

[9] M. Kurosawa, Y. Fukuda, M. Takasaki, and T. Higuchi, "A surface acoustic wave gyro sensor," in *, 1997 International Conference on Solid State Sensors and Actuators, 1997. TRANSDUCERS '97 Chicago*, 1997, vol. 2, pp. 863–866 vol.2.

[10] W. Wang, H. Oh, K. Lee, S. Yoon, and S. Yang, "Enhanced Sensitivity of Novel Surface Acoustic Wave Microelectromechanical System-Interdigital Transducer Gyroscope," *Jpn. J. Appl. Phys.*, vol. 48, no. 6, p. 06FK09, Jun. 2009.

[11] H. Oh, W. Wang, S. Yang, and K. Lee, "Development of SAW based gyroscope with high shock and thermal stability," *Sens. Actuators Phys.*, vol. 165, no. 1, pp. 8–15, Jan. 2011.

[12] H. Oh, C. Fu, S. S. Yang, W. Wang, and K. Lee, "A novel shock and heat tolerant gyrosensor utilizing a one-port surface acoustic wave reflective delay line," *J. Micromechanics Microengineering*, vol. 22, no. 4, p. 045007, 2012.

[13] K. R. Parameswaran, R. K. Route, J. R. Kurz, R. V. Roussev, M. M. Fejer, and M. Fujimura, "Highly efficient second-harmonic generation in buried waveguides formed by annealed and reverse proton exchange in periodically poled lithium niobate," *Opt. Lett.*, vol. 27, no. 3, pp. 179–181, Feb. 2002.

[14] W. K. Burns, R. P. Moeller, C. H. Bulmer, and H. Yajima, "Optical waveguide channel branches in Ti-diffused $LiNbO_3$," *Appl. Opt.*, vol. 19, no. 17, pp. 2890–2896, Sep. 1980.

[15] M. L. Bortz and M. M. Fejer, "Annealed proton-exchanged $LiNbO_3$ waveguides," *Opt. Lett.*, vol. 16, no. 23, pp. 1844–1846, Dec. 1991.

[16] L. Cai, Y. Kang, and H. Hu, "Electric-optical property of the proton exchanged phase modulator in single-crystal lithium niobate thin film," *Opt Express OE*, vol. 24, no. 5, pp. 4640–4647, Mar. 2016.
[17] G. Poberaj, H. Hu, W. Sohler, and P. Günter, "Lithium niobate on insulator (LNOI) for micro-photonic devices," *Laser Photon Rev*, vol. 6, no. 4, pp. 488–503, Jul. 2012.
[18] A. Guarino, G. Poberaj, D. Rezzonico, R. Degl'Innocenti, and P. Günter, "Electro–optically tunable microring resonators in lithium niobate," *Nat. Photonics*, vol. 1, no. 7, p. 407, Jul. 2007.
[19] H. Lu, B. Sadani, N. Courjal, G. Ulliac, N. Smith, V. Stenger, M. Collet, F. I. Baida, and M.-P. Bernal, "Enhanced electro-optical lithium niobate photonic crystal wire waveguide on a smart-cut thin film," *Opt. Express*, vol. 20, no. 3, pp. 2974–2981, Jan. 2012.
[20] A. J. Mercante, D. L. K. Eng, M. Konkol, P. Yao, S. Shi, and D. W. Prather, "Thin $LiNbO_3$ on insulator electro-optic modulator," *Opt. Lett.*, vol. 41, no. 5, pp. 867–869, Mar. 2016.
[21] H. Hu, R. Ricken, and W. Sohler, "Lithium niobate photonic wires," *Opt. Express*, vol. 17, no. 26, pp. 24261–24268, Dec. 2009.
[22] R. Geiss, S. Saravi, A. Sergeyev, S. Diziain, F. Setzpfandt, F. Schrempel, R. Grange, E.-B. Kley, A. Tünnermann, and T. Pertsch, "Fabrication of nanoscale lithium niobate waveguides for second-harmonic generation," *Opt. Lett.*, vol. 40, no. 12, pp. 2715–2718, Jun. 2015.
[23] A. Rao, A. Patil, J. Chiles, M. Malinowski, S. Novak, K. Richardson, P. Rabiei, and S. Fathpour, "Heterogeneous microring and Mach-Zehnder lithium niobate electro-optical modulators on silicon," in *2015 Conference on Lasers and Electro-Optics (CLEO)*, 2015, pp. 1–2.
[24] M. Mahmoud, S. Ghosh, and G. Piazza, "Lithium Niobate on Insulator (LNOI) Grating Couplers," in *CLEO: 2015 (2015), paper SW4I.7*, 2015, p. SW4I.7.
[25] M. Mahmoud, C. Bottenfield, L. Cai, and G. Piazza, "Fully integrated lithium niobate electro-optic modulator based on asymmetric Mach-Zehnder interferometer etched in LNOI platform," in *2017 IEEE Photonics Conference (IPC)*, 2017, pp. 223–224.
[26] L. Cai, S. Zhang, and H. Hu, "A compact photonic crystal micro-cavity on a single-mode lithium niobate photonic wire," *J. Opt.*, vol. 18, no. 3, p. 035801, 2016.
[27] P. O. Weigel, M. Savanier, C. T. DeRose, A. T. Pomerene, A. L. Starbuck, A. L. Lentine, V. Stenger, and S. Mookherjea, "Lightwave Circuits in Lithium Niobate through Hybrid Waveguides with Silicon Photonics," *Sci. Rep.*, vol. 6, p. 22301, Mar. 2016.
[28] L. Chen, M. G. Wood, and R. M. Reano, "12.5 pm/V hybrid silicon and lithium niobate optical microring resonator with integrated electrodes," *Opt. Express*, vol. 21, no. 22, pp. 27003–27010, Nov. 2013.
[29] *NANOLN JINAN Jingzheng 超平硅片 超平石英片*. .
[30] H. Bhugra and G. Piazza, *Piezoelectric MEMS Resonators*. Springer, 2017.
[31] "Lumerical Inc. | Innovative Photonic Design Tools." [Online]. Available: https://www.lumerical.com/. [Accessed: 12-Jan-2018].
[32] F. Xia, M. Rooks, L. Sekaric, and Y. Vlasov, "Ultra-compact high order ring resonator filters using submicron silicon photonic wires for on-chip optical interconnects," *Opt. Express*, vol. 15, no. 19, pp. 11934–11941, Sep. 2007.
[33] Q. Xu, B. Schmidt, S. Pradhan, and M. Lipson, "Micrometre-scale silicon electro-optic modulator," *Nature*, vol. 435, no. 7040, p. 325, May 2005.

[34] M. Mahmoud, L. Cai, C. Bottenfield, and G. Piazza, "Lithium Niobate Electro-optic Racetrack Modulator Etched in Y-Cut LNOI Platform," *IEEE Photonics J.*, to be published.
[35] Q. Xu and M. Lipson, "All-optical logic based on silicon micro-ring resonators," *Opt. Express*, vol. 15, no. 3, pp. 924–929, Feb. 2007.
[36] A. G. Griffith, R. K. Lau, J. Cardenas, Y. Okawachi, A. Mohanty, C. Poitras, A. L. Gaeta, and M. Lipson, "Silicon-Chip Mid-Infrared Frequency Comb Generation," in *CLEO: 2014 Postdeadline Paper Digest (2014), paper STh5C.6*, 2014, p. STh5C.6.
[37] M. Bachmann, P. A. Besse, and H. Melchior, "Overlapping-image multimode interference couplers with a reduced number of self-images for uniform and nonuniform power splitting," *Appl Opt AO*, vol. 34, no. 30, pp. 6898–6910, Oct. 1995.
[38] D. Ding, L. M. C. Pereira, J. F. Bauters, M. J. R. Heck, G. Welker, A. Vantomme, J. E. Bowers, M. J. A. de Dood, and D. Bouwmeester, "Multidimensional Purcell effect in an ytterbium-doped ring resonator," *Nat. Photonics*, vol. 10, no. 6, p. 385, Jun. 2016.
[39] S. Ghosh and G. Piazza, "Laterally vibrating resonator based elasto-optic modulation in aluminum nitride," *APL Photonics*, vol. 1, no. 3, p. 036101, 2016.
[40] A. Ksendzov and Y. Lin, "Integrated optics ring-resonator sensors for protein detection," *Opt. Lett.*, vol. 30, no. 24, pp. 3344–3346, Dec. 2005.
[41] G. T. Reed, G. Mashanovich, F. Y. Gardes, and D. J. Thomson, "Silicon optical modulators," *Nat. Photonics*, vol. 4, no. 8, p. 518, Aug. 2010.
[42] P. Dumon, W. Bogaerts, V. Wiaux, J. Wouters, S. Beckx, J. Van Campenhout, D. Taillaert, B. Luyssaert, P. Bienstman, D. Van Thourhout, and R. Baets, "Low-loss SOI photonic wires and ring resonators fabricated with deep UV lithography," *IEEE Photonics Technol. Lett.*, vol. 16, no. 5, pp. 1328–1330, May 2004.
[43] X. Xiao, M. Li, L. Wang, D. Chen, Q. Yang, and S. Yu, "High speed silicon photonic modulators," in *2017 Optical Fiber Communications Conference and Exhibition (OFC)*, 2017, pp. 1–3.
[44] M. Garcia-Granda, H. Hu, J. Rodriguez-Garcia, and W. Sohler, "Design and Fabrication of Novel Ridge Guide Modulators in Lithium Niobate," *J. Light. Technol.*, vol. 27, no. 24, pp. 5690–5697, Dec. 2009.
[45] H.-C. Huang, J. I. Dadap, G. Malladi, I. Kymissis, H. Bakhru, and R. M. Osgood, "Helium-ion-induced radiation damage in $LiNbO_3$ thin-film electro-optic modulators," *Opt. Express*, vol. 22, no. 16, pp. 19653–19661, Aug. 2014.
[46] C. Wang, M. Zhang, B. Stern, M. Lipson, and M. Loncar, "Nanophotonic Lithium Niobate Electro-optic Modulators," *ArXiv170106470 Cond-Mat Physicsphysics*, Jan. 2017.
[47] K. C. Balram, M. I. Davanço, B. R. Ilic, J.-H. Kyhm, J. D. Song, and K. Srinivasan, "Acousto-Optic Modulation and Optoacoustic Gating in Piezo-Optomechanical Circuits," *Phys. Rev. Appl.*, vol. 7, no. 2, p. 024008, Feb. 2017.
[48] S. A. Tadesse and M. Li, "Sub-optical wavelength acoustic wave modulation of integrated photonic resonators at microwave frequencies," vol. 5, p. 5402, Nov. 2014.
[49] S. A. Tadesse, H. Li, Q. Liu, and M. Li, "Acousto-optic modulation of a photonic crystal nanocavity with Lamb waves in microwave K band," *Appl. Phys. Lett.*, vol. 107, no. 20, p. 201113, Nov. 2015.
[50] X. Han, K. Y. Fong, and H. X. Tang, "A 10-GHz film-thickness-mode cavity optomechanical resonator," *Appl. Phys. Lett.*, vol. 106, no. 16, p. 161108, Apr. 2015.

[51] G. Fan, Y. Li, C. Hu, L. Lei, D. Zhao, H. Li, and Z. Zhen, "A novel concept of acousto-optic ring frequency shifters on silicon-on-insulator technology," *Opt. Laser Technol.*, vol. 63, no. Supplement C, pp. 62–65, Nov. 2014.
[52] L. Fan, C.-L. Zou, M. Poot, R. Cheng, X. Guo, X. Han, and H. X. Tang, "Integrated optomechanical single-photon frequency shifter," *Nat. Photonics*, vol. 10, no. 12, p. 766, Dec. 2016.
[53] J.-C. Kastelik, S. Dupont, K. B. Yushkov, V. Y. Molchanov, and J. Gazalet, "Double acousto-optic deflector system for increased scanning range of laser beams," *Ultrasonics*, vol. 80, no. Supplement C, pp. 62–65, Sep. 2017.
[54] W. Yang, Y. Liu, L. Xiao, and Z. Yang, "Wavelength-Tunable Erbium-Doped Fiber Ring Laser Employing an Acousto-Optic Filter," *J. Light. Technol.*, vol. 28, no. 1, pp. 118–122, Jan. 2010.
[55] Z. Shen, X. Han, C.-L. Zou, and H. X. Tang, "Phase sensitive imaging of 10 GHz vibrations in an AlN microdisk resonator," *Rev. Sci. Instrum.*, vol. 88, no. 12, p. 123709, Dec. 2017.
[56] J. Horner, *Optical Signal Processing*. Elsevier, 2012.
[57] Berg, *Acousto-Optic Signal Processing: Theory and Implementation, Second Edition*. CRC Press, 1995.
[58] G. Ryu, Y. Lee, and K. Lee, "Development of acoustic-optic (AO) SLM applicable to 3D holographic dispay," in *2017 19th International Conference on Solid-State Sensors, Actuators and Microsystems (TRANSDUCERS)*, 2017, pp. 1979–1982.
[59] J. Xu and R. Stroud, *Acousto-optic devices: principles, design, and applications*. Wiley, 1992.
[60] H. Li, S. A. Tadesse, Q. Liu, and M. Li, "Nanophotonic cavity optomechanics with propagating acoustic waves at frequencies up to 12 GHz," *Optica*, vol. 2, no. 9, pp. 826–831, Sep. 2015.
[61] M. M. de Lima, M. Beck, R. Hey, and P. V. Santos, "Compact Mach-Zehnder acousto-optic modulator," *Appl. Phys. Lett.*, vol. 89, no. 12, p. 121104, Sep. 2006.
[62] A. Crespo-Poveda, R. Hey, K. Biermann, A. Tahraoui, P. V. Santos, B. Gargallo, P. Muñoz, A. Cantarero, and M. M. de Lima, "Synchronized photonic modulators driven by surface acoustic waves," *Opt. Express*, vol. 21, no. 18, pp. 21669–21676, Sep. 2013.
[63] C. S. Tsai, *Guided-wave Acousto-optics: Interactions, Devices, and Applications*. Springer-Verlag, 1990.
[64] R. W. Dixon, "Photoelastic Properties of Selected Materials and Their Relevance for Applications to Acoustic Light Modulators and Scanners," *J. Appl. Phys.*, vol. 38, no. 13, pp. 5149–5153, Dec. 1967.
[65] J. J. Campbell and W. R. Jones, "A method for estimating optimal crystal cuts and propagation directions for excitation of piezoelectric surface waves," *IEEE Trans. Sonics Ultrason.*, vol. 15, no. 4, pp. 209–217, Oct. 1968.
[66] T.-T. Wu, Z.-C. Hsu, and Z.-G. Huang, "Band gaps and the electromechanical coupling coefficient of a surface acoustic wave in a two-dimensional piezoelectric phononic crystal," *Phys. Rev. B*, vol. 71, no. 6, p. 064303, Feb. 2005.
[67] S. Datta, *Surface acoustic wave devices*. Prentice-Hall, 1986.
[68] M. Mahmoud, C. Bottenfield, L. Cai, and G. Piazza, "Fully integrated lithium niobate electro-optic modulator based on asymmetric Mach-Zehnder interferometer etched in LNOI platform," in *2017 IEEE Photonics Conference (IPC)*, 2017, pp. 223–224.

[69] J. E. Zucker, T. L. Hendrickson, and C. A. Burrus, "Electro-optic phase modulation in GaAs/AlGaAs quantum well waveguides," *Appl. Phys. Lett.*, vol. 52, no. 12, pp. 945–947, Mar. 1988.
[70] L. A. Coldren, S. W. Corzine, and M. L. Mašanović, *Diode Lasers and Photonic Integrated Circuits: Coldren/Diode Lasers 2E*. Hoboken, NJ, USA: John Wiley & Sons, Inc., 2012.
[71] B. E. A. Saleh and M. C. Teich, *Fundamentals of Photonics*. Wiley, 2007.
[72] A. Yariv, "Critical coupling and its control in optical waveguide-ring resonator systems," *IEEE Photonics Technol. Lett.*, vol. 14, no. 4, pp. 483–485, Apr. 2002.
[73] Q. Xu, S. Manipatruni, B. Schmidt, J. Shakya, and M. Lipson, "12.5 Gbit/s carrier-injection-based silicon micro-ring silicon modulators," *Opt. Express*, vol. 15, no. 2, pp. 430–436, Jan. 2007.
[74] D. Rozelle, *The Hemispherical Resonator Gyro: From Wineglass to the Planets*, vol. 134. 2009.
[75] T. Zhang, Z. Lin, M. Song, B. Zhou, and R. Zhang, "Study on the thermoforming process of Hemispherical Resonator Gyros (HRGs)," in *2017 IEEE International Symposium on Inertial Sensors and Systems (INERTIAL)*, 2017, pp. 140–141.
[76] A. Shebl, A. M. Othman, A. Mahmoud, G. Albert, Y. M. Sabry, K. Sharaf, and D. Khalil, "Ring laser gyroscope based on standard single-mode fiber and semiconductor optical amplifier," in *2016 33rd National Radio Science Conference (NRSC)*, 2016, pp. 368–376.
[77] C. Ciminelli, F. Dell'Olio, and M. N. Armenise, "High-Q Spiral Resonator for Optical Gyroscope Applications: Numerical and Experimental Investigation," *IEEE Photonics J.*, vol. 4, no. 5, pp. 1844–1854, Oct. 2012.
[78] L. Zhao, W. Li, H. Zhang, Y. Yang, A. Huang, and Z. Xiao, "Improving the scale factor for rotation sensing in a frequency sensitive integrated optical gyroscope," presented at the International Conference on Optoelectronics and Microelectronics Technology and Application, 2017, vol. 10244, p. 102440E.
[79] I. P. Prikhodko, S. Nadig, J. A. Gregory, W. A. Clark, and M. W. Judy, "Half-a-month stable 0.2 degree-per-hour mode-matched MEMS gyroscope," 2017, pp. 1–4.
[80] E. E. Aktakka, J. K. Woo, and K. Najafi, "On-chip characterization of scale-factor of a MEMS gyroscope via a micro calibration platform," in *2017 IEEE International Symposium on Inertial Sensors and Systems (INERTIAL)*, 2017, pp. 1–4.
[81] E. Tatar, T. Mukherjee, and G. K. Fedder, "Stress Effects and Compensation of Bias Drift in a MEMS Vibratory-Rate Gyroscope," *J. Microelectromechanical Syst.*, vol. 26, no. 3, pp. 569–579, Jun. 2017.
[82] W. Ma, Y. Lin, S. Liu, X. Zheng, and Z. Jin, "A novel oscillation control for MEMS vibratory gyroscopes using a modified electromechanical amplitude modulation technique," *J. Micromechanics Microengineering*, vol. 27, no. 2, p. 025005, 2017.
[83] Z. Luo, X. Wang, M. Jin, and S. Liu, "MEMS gyroscope yield simulation based on Monte Carlo method," in *2012 IEEE 62nd Electronic Components and Technology Conference*, 2012, pp. 1636–1639.
[84] S. Askari, M. H. Asadian, K. Kakavand, and A. M. Shkel, "Vacuum sealed and getter activated MEMS Quad Mass Gyroscope demonstrating better than 1.2 million quality factor," in *2016 IEEE International Symposium on Inertial Sensors and Systems*, 2016, pp. 142–143.

[85] A. Mahmoud, W. Fikry, Y. M. Sabry, and M. A. E. Mahmoud, “Staggered mode MEMS gyroscope,” in *2016 Fourth International Japan-Egypt Conference on Electronics, Communications and Computers (JEC-ECC)*, 2016, pp. 103–106.
[86] M. S. Weinberg and A. Kourepenis, “Error sources in in-plane silicon tuning-fork MEMS gyroscopes,” *J. Microelectromechanical Syst.*, vol. 15, no. 3, pp. 479–491, Jun. 2006.
[87] M. Kurosawa, Y. Fukuda, M. Takasaki, and T. Higuchi, “A surface-acoustic-wave gyro sensor,” *Sens. Actuators Phys.*, vol. 66, no. 1, pp. 33–39, Apr. 1998.
[88] B. Davaji, V. Pinrod, S. Kulkarni, and A. Lal, “Towards a surface and bulk excited SAW gyroscope,” in *2017 IEEE International Ultrasonics Symposium (IUS)*, 2017, pp. 1–4.
[89] Y. Musha, M. Hara, H. Asano, and H. Kuwano, “Oscillator based surface acoustic wave gyroscopes,” in *2016 IEEE 11th Annual International Conference on Nano/Micro Engineered and Molecular Systems (NEMS)*, 2016, pp. 557–560.
[90] M.Mahmoud, L.Cai, C.Bottenfield, and G.Piazza, “Fully Integrated Lithium Niobate Electro-Optic Modulator based on Asymmetric Mach-Zehnder Interferometer Etched in LNOI Platform,” presented at the IEEE Photonics, 2017.
[91] M. Terrel, M. J. F. Digonnet, and S. Fan, “Ring-coupled Mach-Zehnder interferometer optimized for sensing,” *Appl Opt AO*, vol. 48, no. 26, pp. 4874–4879, Sep. 2009.
[92] J. Heebner, R. Grover, T. Ibrahim, and T. A. Ibrahim, *Optical Microresonators: Theory, Fabrication, and Applications*. Springer Science & Business Media, 2008.
[93] M. Zhang, C. Wang, R. Cheng, A. Shams-Ansari, and M. Lončar, “Monolithic ultra-high-Q lithium niobate microring resonator,” *Optica*, vol. 4, no. 12, pp. 1536–1537, Dec. 2017.
[94] M.Mahmoud, L.Cai, C.Bottenfield, and G.Piazza, “Fully Integrated Lithium Niobate Electro-Optic Modulator based on Asymmetric Mach-Zehnder Interferometer Etched in LNOI Platform,” presented at the IEEE photonics, 2017.
[95] W. Wen, H. Shitang, L. Shunzhou, L. Minghua, and P. Yong, “Enhanced sensitivity of SAW gas sensor coated molecularly imprinted polymer incorporating high frequency stability oscillator,” *Sens. Actuators B Chem.*, vol. 125, no. 2, pp. 422–427, Aug. 2007.